UNIVERSITY OF CALIFORNIA
RIVERSIDE

The Role of Isolated Metal Atoms and Support Effects in CO_2 Reduction Catalysis by Rh

A Dissertation submitted in partial satisfaction
of the requirements for the degree of

Doctor of Philosophy

in

Chemical and Environmental Engineering

by

John Matsubu

June 2016

Dissertation Committee:
Dr. Phillip Christopher, Chairperson
Dr. Francisco Zaera
Dr. David Kisailus

The Dissertation of John Matsubu is approved:

_____

_____

_____

Committee Chairperson

University of California, Riverside

ACKNOWLEDGEMENTS

First off, I would like to acknowledge my adviser Dr. Phillip Christopher for the great guidance he has given me and the patience he has had with me. I have grown significantly as a researcher and person during the last five years, and this has been in no small part because of the time he has invested and the influence he has had on me. I would additionally like to thank my committee members in Dr. Francisco Zaera and Dr. David Kisailus for their help in redirecting my studies where needed.

I am thankful for the whole Christopher lab for the help and friendship over the course of my studies. Specific credit goes to Matt Kale, Talin Avanesian, Leo DeRita, and Yibo Jiang for helping both in the lab and with discussion. A good portion of my research was due to people like Gabriel Gusmão, Vanessa Yang, Kyle Gunther, and Eric Lin getting their hands dirty and doing a lot of the actual experimentation that was needed. I additionally appreciate Alexander (Sasha) Dudchenko, for being extremely helpful with automation and general troubleshooting in the lab. Thanks to the Taco Tuesday crew for adding a regularly scheduled time to meet up with friends and catch-up/commiserate.

Sergei Hanukovich, Drew Story, and Christian Alcaraz were great help keeping me active, playing basketball and racquetball even through the dormant paper/dissertation writing days. I can't enumerate all of the friendships that I have developed over the years while at UCR and won't attempt to, but the people that have provided the necessary support

to stick with this program were: Matt Kale, Talin Avanesian, Noam Hart, Samarthya Bhagia, Claudia Chaves, Leo DeRita, and Sergei Hanukovich.

I am grateful for the National Science Foundation for funding (#CHE-1301019) a majority of my PhD work.

The text of this dissertation, in part or in full, is a reprint of the material as is appears in Journal of American Chemical Society, "Isolated Metal Active Site Concentration and Stability Control Catalytic CO_2 Reduction Selectivity" in 2015. Vanessa Yang contributed with the material synthesis and reactivity experiments.

The text of this dissertation, in part or in full, is a reprint of the material as is appears in Catalysis Science and Technology, "Critical role of interfacial effects on the reactivity of semiconductor-cocatalyst junctions for photocatalytic oxygen evolution from water" in 2016. Kyle Gunther synthesized materials and tested catalytic reactivity. Eric Lin synthesized materials, tested catalytic reactivity, characterized samples, and aided with writing. Dr. Krassimir Bozhilov performed STEM measurements on the photocatalysts. Yibo Jiang helped with brainstorming and paper editing. The co-author Phillip Christopher listed in both of these publications directed and supervised the research which forms the basis for this dissertation.

DEDICATIONS

This dissertation is dedicated to my family members: Mom, Dad, Bill, and Oceana, for continually inspiring me to push myself outside of my comfort zone.

ABSTRACT OF THE DISSERTATION

The Role of Isolated Metal Atoms and Support Effects in CO_2 Reduction Catalysis by Rh

by

John Matsubu

Doctor of Philosophy, Graduate Program in Chemical and Environmental Engineering
University of California, Riverside, June 2016
Dr. Phillip Christopher, Chairperson

In this work, we coupled a variety of characterization techniques with an array of reactivity experiments to gain the requisite fundamentals for designing optimal heterogeneous catalysts. The main emphasis was to investigate the effect of Rh catalyst site geometry and adsorbate stabilized metal-support interactions on CO_2 reduction selectivity.

Much effort has been performed in the catalysis field identifying active catalytic sites by developing structure-function relationships, however, the role of isolated catalyst sites has often been overlooked due to difficulty in characterizing these single atom catalysts. The hypothesis of our first study was that isolated Rh catalytic sites play a role in driving CO_2 reduction chemical pathways. Through development of a quantitative FTIR technique, fractions of Rh existing in both isolated catalytic (Rh_{iso}) site geometries and surface sites on Rh NPs (Rh_{NP}) were measured and related with kinetic data to identify the site-specific

reactivity of both site types. It was established that Rh_{iso} sites drive CO production and Rh_{NP} sites drive CH_4 production nearly exclusively.

Additionally, interesting dynamic changes in catalyst behavior were observed in CO_2 reduction conditions where CH_4 production decreased, yet CO production increased during time-on-stream. This transformation was investigated by coupling the following *in-situ* techniques: FTIR, ESTEM, EXAFS and XANES, with a battery of reactivity experiments for understanding both the underlying mechanism of this transformation and how to exploit this change in pathway reactivity to control selectivity. Reaction conditions and Rh weight loading were optimized to attain a 90% switch in selectivity between producing CO and CH_4 at the same conditions before and after treating the catalyst with a high CO_2:H_2 ratio. It was determined that the dramatic change in catalyst reactivity was from the TiO_2 support forming a permeable overlayer on the Rh_{NP} sites, which caused them to behave catalytically like a more noble metal and produce CO. Although similar strong metal-support interactions (SMSI) have been thoroughly studied for controlling CO_2 reduction selectivity, unlike in this work, the overlayers formed are usually hindered by either being impermeable to reactants, therefore killing off reactivity completely or unstable in CO_2 reduction reaction conditions.

Table of Contents

List of Figures

List of Tables

Chapter 1 Introduction

1.1 Significance of Heterogeneous Catalysis

Continued human population growth coupled with increasing standards of living around the world has led to an increase in consumption of both fuels and chemicals of mass proportions. Unfortunately, many of the feedstocks used to produce these fuels and chemicals are non-renewable and are therefore not a sustainable solution to satiating the ever growing global appetite for these products. Additionally, both the production and consumption of these products have led to outrageous levels of emitted pollutants, so, with increasing population, comes increasing demand for tapping our dwindling reserves and polluting the environment. One commonality in both the production of fuels and chemicals often using fossil fuels and mitigating the pollution emitted from their production and consumption, is the need to drive many different chemical reactions. A catalyst is a substance that increases the rate of a chemical reaction without being consumed in the process, and they have been utilized for expediting chemical processes for centuries in the form of enzymes for producing foods such as beer, wine, and bread.[1] However, inorganic catalysis is the only process for driving many of the industrially relevant chemistries in the economically feasible manner that we as a society have become accustomed to. Due to engineering simplicity, heterogeneous catalysis, where the catalyst is a different phase than the reactants, is implemented at the largest of scales. Over the last century or so, many great findings in catalysis have contributed to significantly improving our standard of living to the point that catalysis contributes in some manner to about 35% of the global GDP.[2]

Although patented in 1831 by Peregrin Philips, the first example of heterogeneous catalysts being implemented at an industrial scale was not until about 1875, where platinum catalysts were utilized to produce sulfuric acid.[3] Ever since heterogeneous catalysis has been beneficent of the symbiotic collaboration between chemists and engineers, the advancement of the field and society has grown rapidly. The major industries that heterogeneous catalysis drives are the chemicals, fuels, and pollution mitigation areas and each of these areas have had a game-changing invention with impact on the global scale.

1.1.1 Ammonia Synthesis: Haber-Bosch Process

Due to nitrogen-exhausted soil making it more difficult to attain desired crop yields, Europe was on the verge of a food crisis at the beginning of the 20th century. Organic fertilizers such as animal manure and saltpeter (potassium nitrate) were unable to keep up with the rate of nitrogen removal from agriculture.[4] However, fertilizers produced from ammonia were known to decompose in the soil and replenish the vital nitrogen levels. By the beginning of the 20th century, there were several inefficient methods for producing nitrogen-based fertilizers via nitrogen fixation directly from air, however it was two German chemists, Fritz Haber and Carl Bosch, who developed a much more efficient and scalable catalytic process for producing ammonia known as the Haber-Bosch process.

$$N_2 + 3H_2 \rightleftharpoons 2NH_3 \qquad \text{Eq. 1.1}$$

The process was catalyzed by a promoted iron catalyst at about 600 ˚C and 100 bar with a recycle step of the unconverted hydrogen and nitrogen as the single pass conversion was only about 15%.[5] BASF purchased the rights to the Haber-Bosch process, which became operating at the industrial scale by 1913. This process is still the main method for

producing ammonia to this day and makes up about (90%) of all ammonia produced[5], 88% of the domestically produced NH_3 is used in the fertilizer industry.[6] Not only did both Haber (1918) and Bosch (1931) receive the Nobel Prize in Chemistry for the invention of the process and scale-up of the process respectively, but the Fritz-Haber process is considered by some to be the most important invention of the 20th century.[7] About 1% of the global electricity is used in ammonia production which is responsible for feeding about half of the world's population.[7]

In addition to the Haber-Bosch process, there are four other catalytic advancements in the 20th century to note which have played a large role in shaping our everyday lives, two of which were amazingly invented by French engineer Eugene Houdry.

1.1.2 Synthetic Fuels: Fischer-Tropsch Synthesis

$$(2n + 1)\ H_2 + n\ CO \rightarrow C_nH_{(2n+2)} + n\ H_2O \qquad \text{Eq. 1.2}$$

The large increase in known natural gas reserves over the last couple of decades, many of which are stranded and unsuitable for delivery via pipeline, has stirred interest in converting the low-density gas into economically transportable liquid hydrocarbons. Fischer-Tropsch (FT) synthesis is a ~90 years technology that has served as the reference for measuring the feasibility of any other methane activation technologies.[8] The process was invented by Franz Fischer and Hans Tropsch in 1925 to produce synthetic fuels and lubrications from a mixture of CO and H_2 synthesis gas which can be derived from coal, natural gas, or biomass. The utility of the FT process stems from being able to produce the synthesis gas by gasifying various feedstocks and essentially removes the dependence on

crude oil, however the cost is higher than crude oil and therefore very cheap feedstocks or political sanctions have been instances when FT was utilized. The development of FT occurred in Germany during both world wars when resources were limited and South Africa has used the FT process for more than 60 years, due to their lack of oil reserves from economic sanctions past political sanctions in combination with cheap coal.[9]

The catalysts used for driving FT synthesis are typically either iron, cobalt, or ruthenium. A huge effort has gone into understanding the FT mechanism which undergoes sequential chain growth and always produces a mixture of hydrocarbons with varied chain lengths, which can be understood with polymerization models.[10]

1.1.3 Fluidized Catalytic Cracking (FCC):

The third invention was fluidized catalytic cracking (FCC) which is the upgrading of high molecular weight fractions of crude oil into products that were shorter in length, yet higher in value such as gasoline, olefins, and other chemicals. It became useful in supplying about 90% of the Allies demand for jet fuel in WWII allowing British aircraft to dramatically outperform German aircraft with much higher octane fuel.[11,12] FCC units benefit from the advancement of engineering, specifically fluidized catalyst beds which allowed for the catalyst to be continuously regenerated of coke build-up, and the advancement of chemistry, to synthesize and utilize synthetic alumina-silicate zeolite catalysts which have reactivity in their acidic sites.

1.1.4 Catalytic Converters: Detoxifying Automobile Exhaust

Eugene Houdry was also responsible for inventing the catalytic converter, which was such a success in detoxifying automobile exhaust and cleaning up the surrounding air that

within a decade of the US implementing these devices, Japan and Europe followed suit.[13] Catalyzing combustion exhaust is an interesting process, as it requires catalyzing three different types of reactions, the oxidation of CO, oxidation of hydrocarbons, and the reduction of NOx. Because there are three simultaneous reaction types to catalyze, this is called three-way catalysis or TWC and commonly has three different noble metals in Pt, Pd, and Rh for driving these reactions. Rh drives the reduction reactions, Pd drives the oxidation reactions, and Pt can drive both oxidation and reduction reactions. Although there has been extensive research in the field of emissions catalysis, as reviewed by McCabe,[13,14] there exist continuous challenges in the field resulting from continuously tightening emissions regulations related to actual concentrations of pollutants and increasing reactivity to decrease emissions at startup.

The examples mentioned above have had significant impact in allowing us to live our modern life as we do. Heterogeneous catalysis requires multi-scale problem solving of grand proportions, where fundamentals of the catalyst surface are on the atomic scale (<1nm), and the fundamental insights gained are then implemented in reactors (meter-scale) within chemical processing plants (km-scale). With chemical production estimated to increase by about 130% between 2015 and 2030, it is important to understand the fundamentals of catalysis down to the atomic scale, to achieve maximum efficiency of these catalytic processes on a reactant and catalyst basis.[15]

1.2 Fundamentals of Oxide Supported Metal Heterogeneous Catalysts

As the providers of these crucial innovations, scientists and engineers bear the responsibility of maximizing efficiency of these processes by minimizing waste of the

process feedstock or reactants, energy used to drive these reactions, and the catalyst materials. The three main descriptors used to describe the performance of a catalyst are activity, selectivity, and catalyst stability, and each of them play a role in the efficiency of a catalytic process. The activity of a catalyst is a measure of how fast the catalyst drives a chemical reaction, which typically changes with respect to temperature, and therefore designing a catalyst with higher activity would either decrease the amount of catalyst and therefore reactor size or the amount of thermal input which is often through the combustion of fossil fuels. Most chemical processes contain several possible reaction pathways resulting in products of varying value. Selectivity represents the percentage of total products that are the desired product, therefore by maximizing selectivity toward the desired product, waste of the feedstock is minimized. Lastly, many of the best performing catalysts are expensive precious metals, making it important cost-wise for the catalysts to have a high stability, and in turn, a long lifetime under reaction conditions.

While in the past, heterogeneous catalyst development has been considered black magic more than rational design, the main reason for studying heterogeneous catalysis is to optimize these three descriptors in a well-understood and rational manner. By gaining insight as to how these materials, which have a resemblance somewhere between flour and sand to the naked eye, interact with reactants, intermediates, and products, on the atomic-scale we can design optimal catalysts in a more efficient and direct manner.

Heterogeneous catalysts increase the rate of chemical reactions dramatically by decreasing the activation barrier of a reaction compared to the reaction occurring in the gas phase, Figure 1.1 In heterogeneous catalysis, reactants diffuse from the gas-phase to the

catalyst surface where the four elementary steps then occur: (1) adsorption to the catalyst surface, (2) adsorbed reactant (adsorbate) dissociation (3) association of these adsorbate intermediates with bond formation and (4) product desorption, Figure 1.1. For each reaction pathway and catalyst, the slow step in this sequence of elementary steps is called the rate limiting step (RLS). The rate of the overall reaction is only as fast as the RLS, therefore it is important to both identify which step is rate limiting and tune the catalyst to

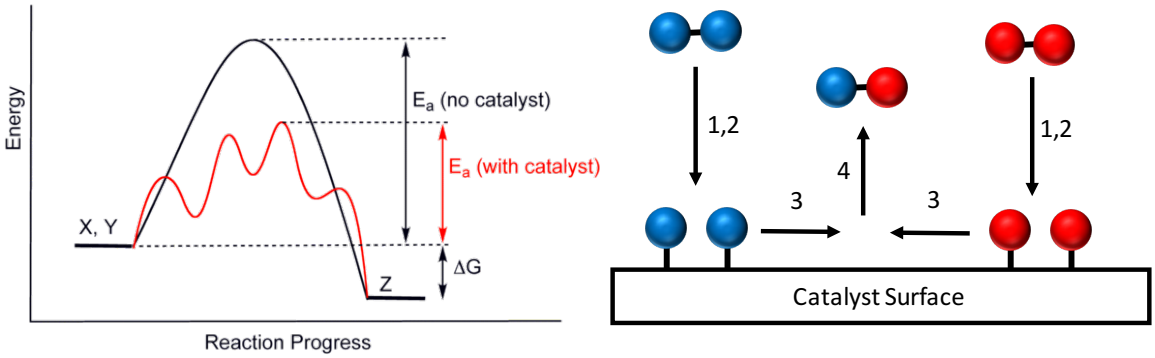

Figure 1.1 Heterogeneous Catalysis Fundamentals (left)Potential energy diagram of both catalyzed and uncatalyzed reaction pathways (right) Elementary heterogeneous catalysis steps. 1) Adsorption, 2) Dissociation 3) Association 4) Desorption

specifically lower the activation barrier of the RLS and accelerate the overall reaction rate for the desired pathway. Empirically speaking, it has been well established that certain metals are ideal for driving different reaction types, where more noble metals (Pd, Pt, Cu, Ag, Au) have been identified for driving oxidation reactions such as CO and hydrocarbon oxidation[16–18] in catalytic converters as well as the partial reduction of CO_2 into CO (reverse-water-gas-shift),[13,14,19–21] less noble transition metals like Fe, Ru, Rh, and CO drive reactions such as complete reduction of CO_2 to CH_4[22,23] or Fischer-Tropsch reaction,[8,24,25] and Ru and Re are most active for driving ammonia synthesis.[26–28] Paul Sabatier observed in 1920 that the ability of a metal to catalyze a reaction seemed to depend on both its ability to adsorb reactants strongly enough for them to remain on the metal catalyst surface to

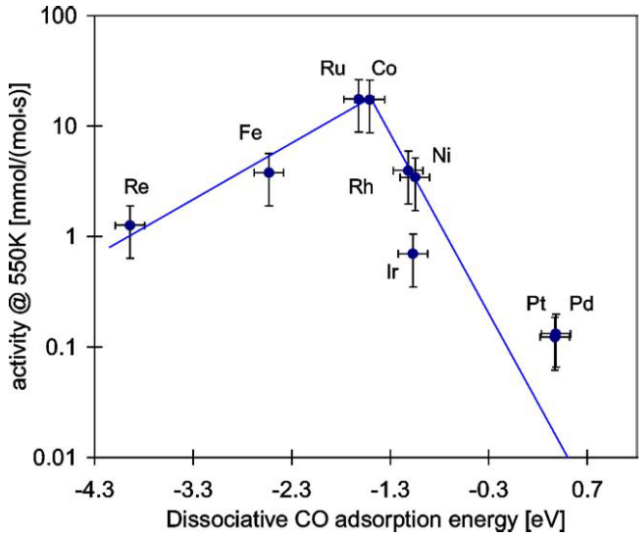

Figure 1.2 Volcano plot of CO methanation vs Dissociative CO adsorption energy. Reproduced with permission from ref. 31.

dissociate into reaction intermediates, yet weakly enough for products to desorb.[29] First introduced by Balandin,[30] volcano plots, such as the one shown in Figure 1.2, are very illustrative of Sabatier's principle in needing a balanced binding energy to maximize reaction rate such as the Ru and Co metals in driving CO methanation.[31] Where the metals with dissociative CO adsorption energies below ~1.4 eV would be limited by CO dissociation, as CO would be less likely to remain on the catalyst surface for dissociation to occur, and the metals with dissociative CO adsorption energies above ~1.4eV would bind CO strongly enough for facile dissociation, however would then be limited by desorption.

The Norskov group has coupled Density Function Theory (DFT) with experimental work to to identify what makes the best catalyst for a specific reaction, and have demonstrated this nicely for reactions which are limited by diatomic molecule activation.[32] Diatomic molecule activation in their study included N_2, CO, NO, and O_2 activation which are crucial for driving ammonia synthesis, Fischer-Tropsch, NO reduction, and CO/hydrocarbon oxidation reactions respectively. While the following example can be extended directly to other reactions limited by diatomic molecule activation, analogous comparisons have been performed for other reactions such as C-H bond breaking.[33] Ammonia synthesis is limited by the activation of N_2, as shown in figure 1.3, where the activation energy (Ea) controls the rate of N_2 dissociation and the ΔE represents the stability of intermediates bound to the transition metal surface. It was determined that Ea and ΔE are linearly related, like a Bronsted-Evans-Polanyi (BEP) relationship, and thus the Ea can be determined experimentally or computationally by calculating the adsorption energy of

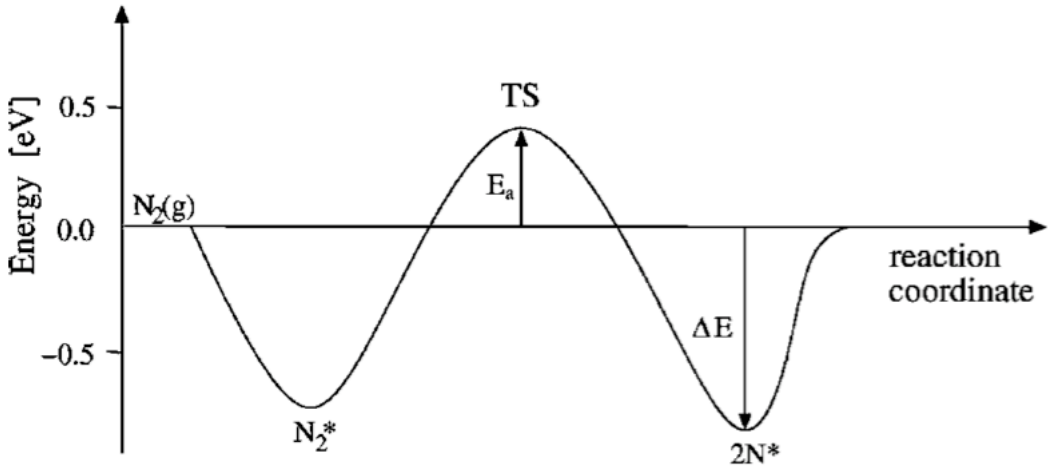

Figure 1.3 Potential energy diagram for N_2 activation on Ru. N_2* and 2N* represent the molecularly and atomically adsorbed (N*) states. TS represents the transition state of dissociation. Ea, controls the rate of dissociation and ΔE is the chemisorption energy which represents the stability of the dissociated product.[32] Reproduced with permission from ref. 32.

the intermediates on the catalyst surface.[34,35] By plotting a volcano curve, the turnover frequency (TOF) as a function of ΔE, the optimal ΔE for a catalyst can then be identified for a given reaction, therefore, this finding was certainly a stepping stone toward rational catalyst design. Essentially, by identifying the RLS, one can tune a catalyst to match the desired adsorption properties which are essentially the ideal compromise between ΔE and Ea for the specific RLS.

1.2.1 Tools for Controlling Catalyst Performance

The three most common tools one can use to affect reactivity of the catalyst surface are catalyst metal type, metal NP size and metal-support interactions.

1.2.2 Catalyst Metal Type

As illustrated by the volcano plot and BEP relations discussed earlier, different metals exhibit different reactivities as a result of the different ΔE and E_a. Nørskov et al. developed the d-band model which explains why the active metals for each reaction type group together on the periodic table.[36,37] Essentially, adsorbate binding energy can be directly related to the level of the d-band center relative to the fermi level, as the metals with lower d-band centers end up forming lower energy level antibonding orbitals with adsorbates, which are therefore more likely to be populated and therefore form weaker metal-adsorbate bonds or adsorption energies. This insight allows one to look at the transition metals on the periodic table as a map, where the adsorption energy decreases left to right and top to bottom and metal type is a tool for tuning the catalytic performance. However, we are not limited to using single metals, as we can go one step further in tuning catalysts by alloying multiple metals to achieve the optimal adsorption energy or to even

mix multiple cheaper metals with peripheral adsorption energies and make the catalyst material cheaper. One recent article which considered these insights by Porosoff et. al., showed that in addition to using d-band center with bimetallic alloys, the d-band center was also used specifically to control the selectivity of CO_2 reduction.

1.2.3 Metal Catalyst Particle Size

The second tool for controlling catalyst performance is to tune catalyst particle size. Unfortunately, many of the most effective catalytic metals that exhibit the most balanced adsorption energies, are also precious and therefore extremely expensive. Metal utilization or dispersion, which is the fraction of metal at the surface of the catalyst available for driving reactions, becomes very important. In order to achieve high dispersion of the metal to ensure high metal utilization, metal catalysts are typically supported on a high surface area (100-300 m^2/g), generally considered inert, metal oxide or alumina-silicate/zeolite support. The work presented in this dissertation strictly used metal oxide supports.

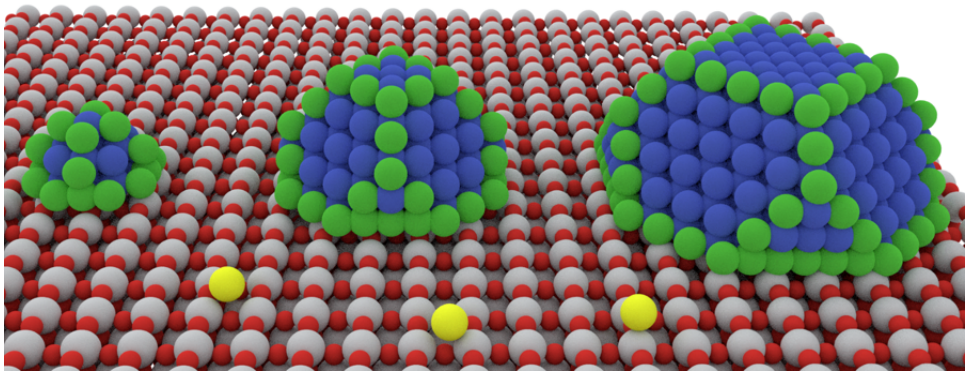

Figure 1.4 Effect of particle size on the effect of site fraction of highly coordinated and undercoordinated metal catalyst sites. Green sites are undercoordinated (steps and corner) sites, blue sites are the highly coordinated (terrace) sites, yellow sites are isolated sites.

There are several ways of depositing metals onto a metal oxide support, with varying levels of difficulty and particle size and shape control, such as wet impregnation or strong electrostatic adsorption, metal sputtering, photoreduction of metal, ion-exchange, colloidal-suspension synthesis specifically of metal NP with subsequent deposition to metal oxide support, however we will only be discussing catalysts that have undergone a dry impregnation technique. With this simple technique, metal particles typically form into the thermodynamically favored cuboctahedron shape, which has surface atoms or catalyst sites driving chemistry with varying coordinations to the neighboring metal atoms. The fraction of these sites changes with particle size as shown in Figure 1.4, therefore if the reactivity of a catalyst is affected by particle size, the reaction is said to be structure sensitive.[25,38,39] These site types can be categorized into terrace, step, and corner site types which are highly, moderately, or under coordinated. The reactivity of these various catalytic sites can be due to either electronic properties (ΔE) or geometric effects. Isolated sites or single atom catalysts, are discussed in section 1.5, and are the extreme example of

particle size control and behave very different from the other site types, as they have a very different electronic structure and geometry, and additionally represent the maximum metal utilization.[39] As shown in Figure 1.4, the fraction of these site types can vary by particle size, therefore, the catalytic reactivity can also be tuned by simply varying the metal particle size. A reaction is said to be structure sensitive if particle size changes the In the simplest impregnation techniques for synthesizing metal oxide supported metal NP catalysts, such as the one used throughout this dissertation, the two main ways of varying metal particle size are to vary metal weight loading or calcination/reduction temperatures and times.

1.2.4 Metal-Support Interactions

The last traditional tool for tuning catalytic reactivity is to vary the support type. There are many different types of metal-support interactions that can affect the catalyst structure both electronically or physically, both of which affect reactivity, as Boudart defined at least six types.[40] Table 1.1 below shows these different classes.

Table 1.1 Six metal-support effects and the observed phenomena

Metal-Support Effect	Phenomenon
Unreduced metal	Strong metal oxide catalyst-metal oxide support preventing complete reduction of metal NP
Support induced size and morphology	Interactions between metal and support cause NP formation to form in raft structure
Contamination or decoration of metal with support	Support contaminates metal in preparation or catalyst reduction
Bifunctional Catalysis	Both metal and supports drive reactions
Spillover	Spillover of adsorbates from the metal to the support or vice-versa
Electron Transfer	Some change in electronic structure of small NPs bound to support

The various metal-support effects in Table 1.1 have been found to affect the activity or selectivity of CO hydrogenation, H_2 and CO adsorption, ethane hydrogenolysis, reforming of naptha, ethylene hydrogenation, pentane dehydrogenation, CO oxidation, and CO_2 reduction to methanol.[41] Discussing the fundamentals involved with the different categorized Metal-Support interactions is out of the scope of this dissertation, as there are many phenomena involved with the interactions between a metal catalyst and oxide support. In section 1.5, we discuss the third type of metal-support interactions, known as Strong Metal-Support Interactions (SMSI), as this is a tool we utilize in a novel manner to control CO_2 reduction selectivity in Chapter 4.

1.3 Catalyzing CO_2 Reduction Reaction

The CO_2 reduction reaction has garnered a significant amount of attention in the catalysis field due to the negative environmental implications of the continued increase in atmospheric CO_2 concentrations from anthropogenic sources, as the world emitted nearly 46 billion tons of CO_2 greenhouse gas (GHG) equivalents in 2010, with 71% of those coming from energy production and use including fuels used by vehicles.[42] Conversion to fuels or chemicals via catalysis has the potential to decrease the CO_2 emissions more than an order of magnitude more than CO_2 sequestration.[43–45] CO_2 conversion could potentially be executed by utilizing CO_2 adsorption technology to capture CO_2 emitted from the largest perpetrating processes of these emissions such as fossil fuel combustion electricity plants and iron/steel production, and then catalytically reducing the CO_2 with sustainably produced H_2. The three main reaction pathways for CO_2 reduction are the production of CO, CH_4, and CH_3OH as shown in eq. 1.3-1.5.

$$CO_2 + H_2 \longrightarrow CO + H_2O \qquad \text{Eq. 1.3}$$

$$CO_2 + 4H_2 \longrightarrow CH_4 + 2H_2O \qquad \text{Eq. 1.4}$$

$$CO_2 + 3H_2 \longrightarrow CH_3OH + H_2O \qquad \text{Eq. 1.5}$$

Equation 1.3 represents the reverse water-gas shift (r-WGS) reaction, producing CO, which can then be used for CH_3OH synthesis or balancing the CO:H_2 ratio for FT synthesis. Equation 1.4 is CO_2 methanation, also known as the Sabatier reaction, which has little application aside from potential aerospace applications for converting CO_2 and waste H_2 into CH_4 (currently for disposal) and H_2O (for further splitting into H_2 –further CO_2 methanation and O_2 -breathing).[46] Methanol production is shown in equation 1.5, this simple alcohol can be utilized both as a fuel or as a chemical feedstock.

The mechanistic picture for CO_2 reduction can be fairly complex, as shown in Figure 1.5, however there are really 3 main paths as summarized and prepared by Porosoff et al.[22] The different possible reaction pathways make it important to understand how to control selectivity in CO_2 reduction. The CO_2 methanation and r-WGS reactions are the two reactions discussed in this dissertation, as the Rh/TiO_2 catalyst used throughout the studies is not an ideal catalyst for driving methanol production at atmospheric pressure.[19] Literature has shown that transition metals can drive these reactions at low reaction temperatures (~150-450 ˚C) where rWGS is driven by more noble metals, such as Cu, Pd, Ag, Pt, Au and methanation is driven by the less noble metals such as Re, Co, Ni, Ru, Rh, Os, and Ir.[21,23,47]

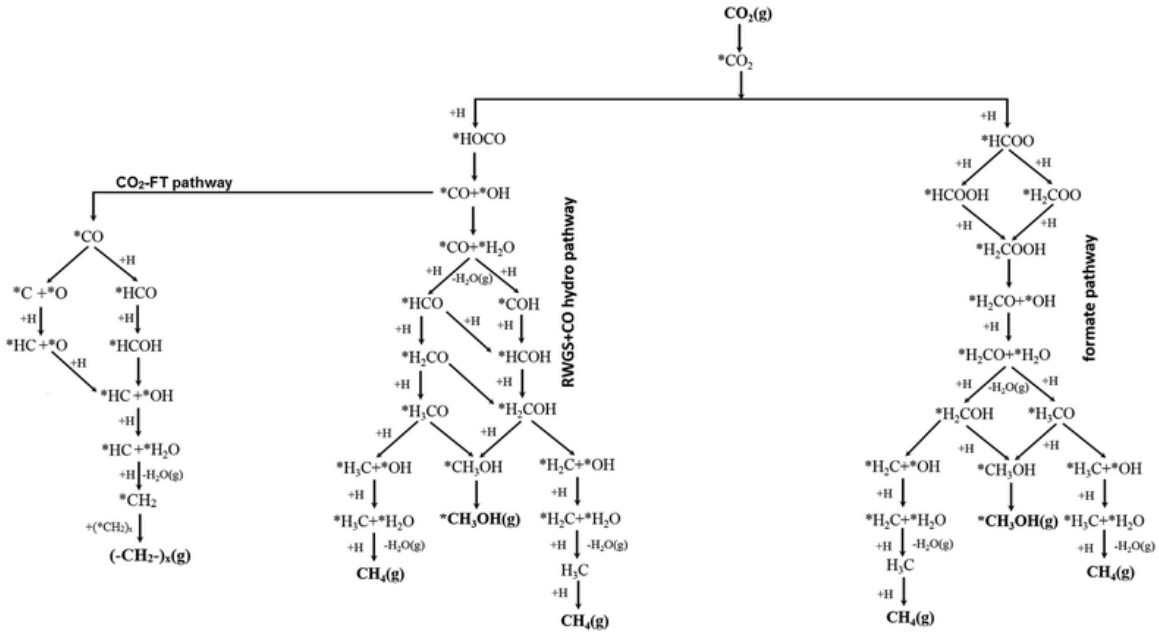

Figure 1.5 Proposed CO_2 reduction mechanisms. Reproduced from reference 22 with permission of The Royal Society of Chemistry.

Rh/TiO_2, the primary catalyst used for CO_2 reduction in this work, is one of the most active methanation catalysts, however there have been some sparse reports towards also producing CO with Rh/TiO_2 associated with low Rh weight loadings.[48] (add a couple more refs)

CO_2 methanation is exothermic and therefore has a higher thermodynamic equilibrium at lower temperatures than R-WGS which is preferred at higher reaction temperatures, as it is endothermic in nature.[49]

While there has been some work looking into the structure sensitivity via particle size of CO_2 methanation, the effect of isolated sites has been investigated for for CO_2 reduction to CO and CH_4 once with La promoted atomically dispersed Pd.[50] In addition, several reports have looked into impact of controlling CO_2 reduction with strong metal support interactions,[47,51–53] however we investigate the effect of an adsorbate stabilized

strong metal support interaction on CO_2 reduction in Chapter 4. The large volume of catalysis research on CO_2 reduction combined with the multiple reaction pathways makes it a great model reaction specifically for studying the impact of isolated sites and novel strong metal-support interactions (SMSI) on the reactivity and controlling selectivity.

1.4 Isolated Catalyst Sites

Yang and Garland used IR spectroscopy in 1957 to first identify single Rh atoms bound to a high surface area alumina support with the observation of the symmetric and asymmetric stretches of a gem-dicarbonyl species (Rh-$(CO)_2$ upon the chemisorption of CO on the Rh surface.[54] These species did not change in wavenumber/bond frequency as a function of CO surface coverage, indicating they were spatially isolated from one another, as carbonyl species that are spatially intimate, like those adsorbed to Rh NP's, blue-shift with increasing CO coverage due to dipole-dipole coupling interactions between the carbonyl groups.[55,56] Yates followed this up with extensive investigations in the late 1970's through the early 1980's regarding physical characteristics and stability of isolated sites,[55,57–60] where his work along with the work of Solymosi in the mid 1980's[61–63] indicated that these isolated sites were not very stable in environments similar to reaction environments. So, while the physical characteristics of these isolated sites garnered significant attention, little of this translated to an impact on catalysis for the following two decades.

Isolated sites have become relevant in the catalysis field over the last 15 or so years with the advancement of high resolution electron microscopy with the sub-nm resolution needed to identify single metal atoms bound to the surface of either zeolite or metal oxide supports. Recent reports have demonstrated the significant catalytic reactivity of supported isolated catalytic atoms or single atoms that were previously masked by the coexistence of metal clusters or nanoparticles due to the lack of characterizing the isolated sites. A majority of this work investigated noble metals (Pt, Pd, Au, and Rh) bound to either zeolites or reducible supports such as (CeO_2, TiO_2, FeOx, MgO, etc.) catalyzing the water–gas- shift (WGS) reaction and CO oxidation.[64–73] Other reactions catalyzed by single atoms or isolated atoms include: NO reduction with H_2,[74] ethylene dimerization,[68] cyclotrimerization of acetylene,[75] hydrogenation of nitroarenes,[76] and photocatalytic H_2 evolution.[77] In addition to their 100% metal utilization, isolated sites are also interesting because they often exhibit lower temperature reactivity,[78] meaning that both catalyst materials and thermal input can be conserved if these isolated site catalysts were to be implemented. These isolated catalyst sites have a difference in electronic structure as they are bound to a metal oxide support rather than other metal atoms, have discrete band energies, and additionally are geometrically similar to a homogeneous catalyst site, as they are both isolated from nearby catalyst sites and their reactivity can be tuned by local oxide support like ligands in homogeneous

catalysis. This homogeneous catalyst-like structure makes these isolated sites a hybrid material between heterogeneous and homogeneous catalysts beneficent of each without the limitations of each, where these isolated site materials benefit from the process engineering simplicity of heterogeneous catalysts and the site isolation and therefore selectivity control of homogeneous catalysts.

Isolated site catalyst reports typically rely on synthetic protocols to create catalysts with a predominance of single isolated sites and microscopy- or spectroscopy-based characterizations to identify the existence of the species. Through this approach, reactivity assignments of the isolated sites are demonstrated. However, in these approaches it can be difficult to quantitatively demonstrate these relationships due to the small sample size of microscopy-based characterization, or difficult fitting procedures, time-consuming, and expensive costs of X-ray absorption spectroscopy analysis of samples with heterogeneous distributions of metal cluster sizes.[79] Furthermore, the focus of these studies has been on the unique reactivity of isolated sites in single reaction pathway reactions (i.e., only one potential product) rather than the potential for isolated sites to exhibit unique selectivity as compared to nanoparticles consisting of the same metal.

Although these materials seem to be promising candidates for optimizing industrial catalytic processes, there still remain several challenges that are being studied, but still need to be overcome such as: a) developing quicker, cheaper, and

more quantitative methods for characterizing these isolated sites, b) understanding the effect that isolated sites play in multiple reaction pathway reactions, c) improved controllability of synthesizing these materials to maximize number of sites, d) increased stability of these sites to prevent agglomeration, e) better understanding of how these sites interact with their support, and f). In this dissertation we worked on challenges a and b, with the expectation that these would expedite the research crucial for meeting the other challenges and provide insight to the role in which isolated sites play in reactions with multiple pathways respectively.

The advancement of electron microscopy technology turned it into a tool that researchers could use to prove the existence of isolated sites, however the miniscule sample size inherent to electron microscopy is too small for statistically quantifying the fraction of isolated sites. CO probe molecule DRIFTS does not suffer from small sample sizes and is indeed a quantitative method for determining the fraction of isolated sites vs the fraction of site on the surface of NPs. In chapter 3, we discuss our efforts in developing the quantitative CO probe molecule DRIFTS method for measuring the number of exposed Rh atoms available for driving chemical reactions both in the isolated site geometry and on the surface of NPs.[80] We investigate the effect of isolated Rh atoms on catalyzing CO_2 reduction and the implication of their role in controlling selectivity of this multi pathway system.

1.5 Strong Metal-Support Interactions

In designing a catalyst, the identification of optimal active sites on supported metal catalysts often focuses on engineering the composition or geometry of the metal site for maximizing reaction rate or controlling reaction selectivity.[80–84] Much less is known about how metal-support interactions can be exploited to control the reactivity of heterogeneous metal oxide supported metal catalysts, although support characteristics can impact catalytic reactivity or selectivity as considerably as characteristics of the metal.[41,85] Demonstrated mechanisms of support effects on metal nanoparticle reactivity include small cluster stabilization,[86] charge transfer,[87–90] support participation in catalysis,[85,91,92] and oxide encapsulation of metal nanoparticles.[93–97] In chapter 4 of this dissertation, we will discuss the effect of oxide encapsulation of metal nanoparticles and how this can be exploited to control selectivity. Encapsulation of metal nanoparticles by reducible oxide support overlayers is the only mechanism by which supports can affect catalysis at a majority of active sites on metal particles with a diameter larger than 1-2 nm.[90]

The encapsulation of metal nanoparticles was designated by Tauster[93] as strong metal support interactions (SMSI) in 1978 after continually observing a dramatic decrease in H_2 and CO chemisorption on certain oxide supported transition metals after high temperature H_2 treatment.[93] With the use of electron microscopy and x-ray diffraction, it was found that agglomeration of the metal nanoparticles could not account for the large decrease in chemisorption values. It was later demonstrated with the advancement of electron microscopy, that the SMSI encapsulation state forms due to high temperature H_2 treatment of reducible oxide-supported Pt-group metals, causing a reduction of the oxide support to

sub-stoichiometric oxygen concentrations and inducing oxide migration on top of metal nanoparticles, as shown in Figure 1.6.[98] Where bonding between cationic support metal atoms and the metal catalyst surface makes migration of the support onto the metal thermodynamically favorable.[99]

Excitement surrounding the discovery of SMSI overlayers was stoked by the suggestion that the SMSI state could potentially be used to tune metal catalyst reactivity via partial decoration of metals by oxide overlayers.[94] However, the SMSI state rarely finds an intermediate configuration where partial metal coverage by the oxide allows interaction

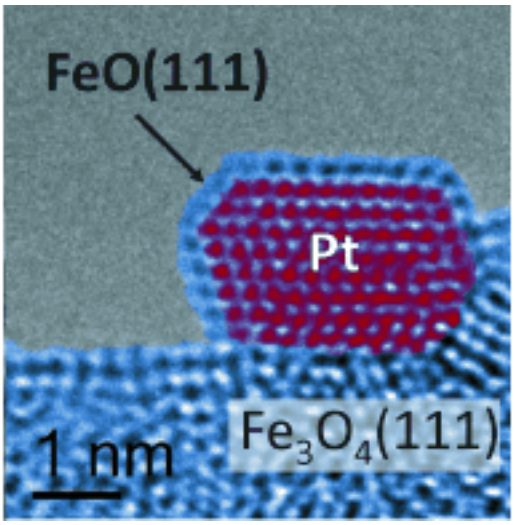

Figure 1.6 Colorized HRTEM micrograph of SMSI induced FeO(111) overlayer formed on the surface of a Pt nanoparticle. Reproduced with permission from ref. 98.

with a majority of exposed metal sites. Instead, the oxide overlayer either covers all metal sites, rendering the catalyst surface inactive, or retreats off the metal due to re-oxidation of the reduced support by H_2O or O_2,[51,100] creating a situation where only a small fraction of metal sites are influenced by the partially reduced support, specifically at the metal-support interface as shown in Figure 1.7 [53,101–103] The poisoning or receded SMSI overlayer

structures that exist under catalytic reaction conditions have curtailed the use of SMSI overlayers to increase reactivity or control selectivity on supported metal catalysts.

In Chapter 4, we demonstrate an SMSI encapsulation state that forms due to treatment of TiO_2 and Nb_2O_5 supported Rh nanoparticles in CO_2-H_2 (CO_2-rich) environments at temperatures of 150-300 °C. *In-situ* spectroscopy and microscopy show that a high coverage of adsorbates (HCO_x) on the support induces oxygen vacancy formation, driving migration of the adsorbate-functionalized support onto the metal. This adsorbate-mediated SMSI (A-SMSI) encapsulation state is stabilized against re-oxidation by H_2O and modifies the reactivity of all remaining exposed Rh sites, appearing to be

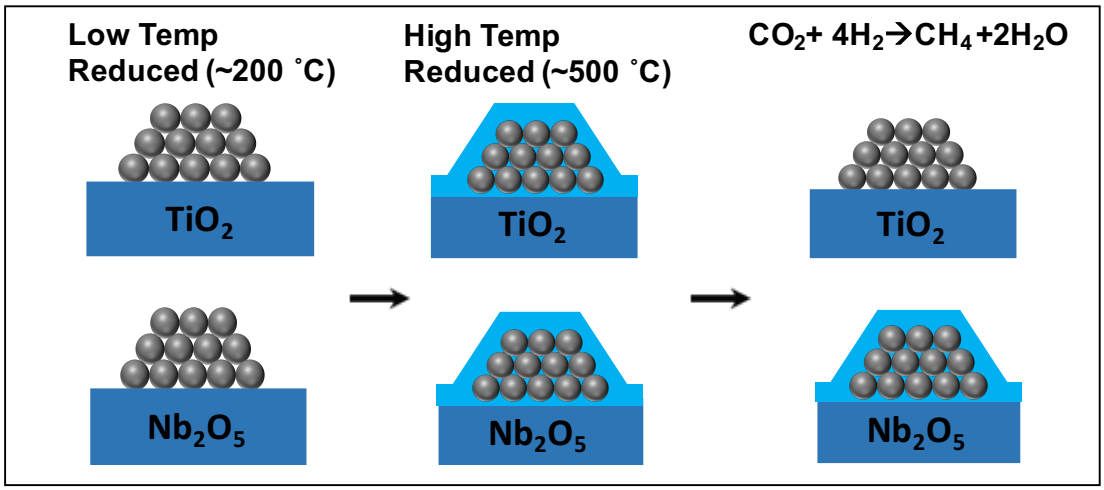

Figure 1.7 Stability of SMSI overlayer under CO_2 reduction conditions for TiO_2 and Nb_2O_5.

comprehensive in covering Rh but amorphous and permeable to reactants. Formation of the A-SMSI state induces a selectivity switch in the CO_2 reduction reaction from CH_4 production on bare Rh particles to CO production in the A-SMSI state, effectively rendering Rh less active for C-H bond formation. Our results show that the A-SMSI state

represents a powerful support effect, enabling rational manipulation of metal catalyst reactivity.

1.6 Fundamentals of Heterogeneous Semiconductor-Based Photocatalysis

Semiconductor photocatalysis differs from thermal catalysis in the activation mechanism by which the catalyst is activated, where thermal catalysts are thermally activated, semiconductor photocatalysts are activated through photon absorption. This photon absorption step requires that a photocatalyst is semiconducting in nature with a band gap energy (energy difference between conduction band minimum and valence band maximum) smaller than the impinging light to be absorbed. In photon absorption, an e- is excited from the valence band to the conduction band, forming a h+ in the conduction band. These charge carriers then either recombine, forming heat, or spatially transfer to the semiconductor surface and drive either a reduction reaction if the e- has a negative enough potential or an oxidation reaction if the h+ has enough of a positive potential. These steps are illustrated in Figure 1.8 below for photocatalytic water splitting, where h+s oxidize water and e- s reduce the protons diatomic H_2.

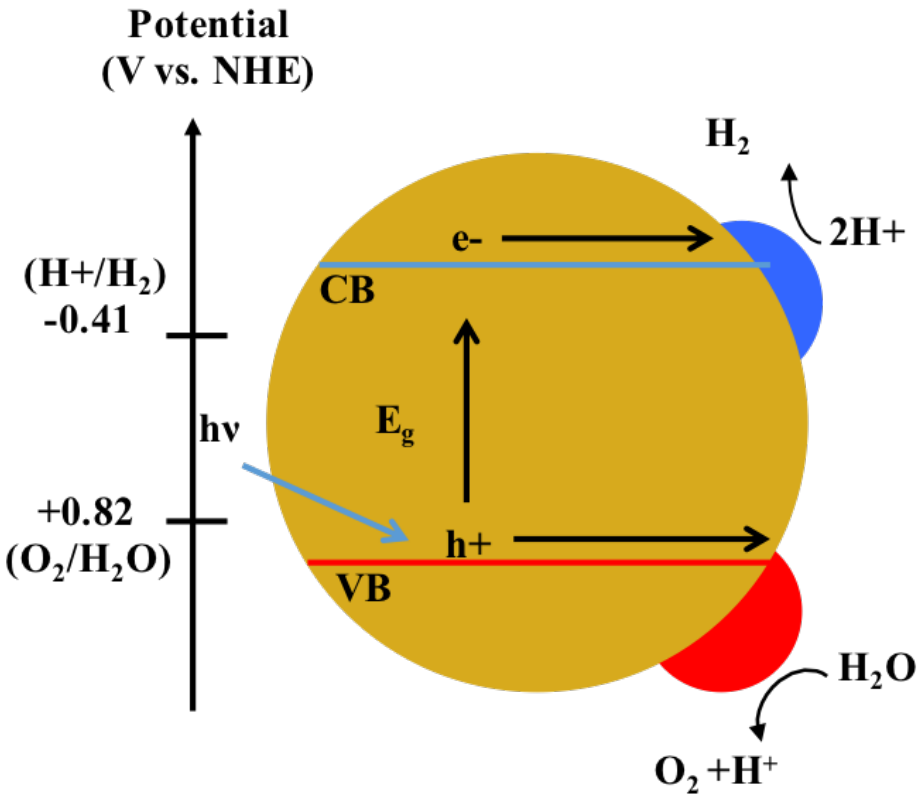

Figure 1.8 Particulate Photocatatalyst Diagram

1.7 Photocatalytic Water Splitting

The global reliance on CO_2 producing fossil fuels for much of our energy consumption and energy production, there is a great need to shift from these fuels toward a cleaner, more sustainable source of energy and chemical feedstocks. The utilization of solar energy to split water, producing H_2 and O_2, is one potentially transformative technology that could provide a nearly endless supply of sustainable fuels and chemicals. As opposed to photovoltaic technology which requires being coupled with energy storage (e.g. batteries, pumped hydroelectric storage, etc.), water splitting provides energy storage in the form of chemical bonds. H_2 is also a valuable feedstock for many chemical processes

which require hydrogenation such as ammonia synthesis, Fischer-Tropsch, CO_2 reduction, and upgrading in the petroleum industry. In addition to its high industrial relevance, because the top three H_2 sources come from steam reforming of natural gas, oil, and coal, a break-through in clean H_2 production would make a significant impact in the: chemicals, fuels, and pollution mitigation fields.[98]

In 1972, Fujishima and Honda started research in the field of semiconductor based photoelectrochemical (PEC) water splitting by demonstrating water splitting with a TiO_2

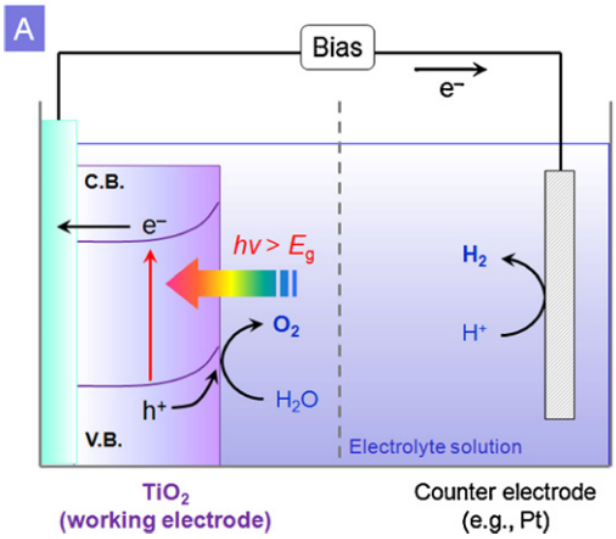

Figure 1.9 Photoelectrochemical (PEC) cell
Reproduced with permission from ref. 106

photoanode and Pt cathode with the aid of a bias.[104] The PEC system, as shown in figure 1.9, absorbs a photon through e- excitation into the conduction band, leaving behind a hole with oxidative potential. The h^+ can then transfer to the SC surface and oxidize a H_2O molecule to evolve O_2, while the e^- then transfers to a cathode (often Pt) where it reduces atomic H into H_2. By 1977, Schrauzer and Guth prepared a powder version of the PEC system by doping TiO_2 to perform water photolysis.[105] This powder system, shown in

Figure 1.8 is essentially a short circuit version of the PEC and is called a particulate photocatalyst (PPC) system. Since the Honda-Fujishima and Schrauzer-Guth publications, there has been a large amount of research performed in the field.[106–115] Various approaches for solar water splitting have been envisioned and realized[104,116–118], although efficiencies and costs are still prohibitive for large-scale application.[108,119] While current state-of-the-art PEC cells exhibit significantly more efficient performance than PPC processes, techno-economic analyses have suggested that PPC processes have the potential to produce H_2 at the lowest costs.[119] Regardless of whether PEC or PPC processes are used to split water, effective transfer of photo-generated charge carriers (electrons, e^-, and holes, h^+) from light absorbing semiconductors (SC) to reactive co-catalysts (CC) that facilitate water splitting half-reactions (oxygen evolution reaction (OER) and hydrogen evolution reaction (HER)) is requisite for high overall process efficiency.

Combinatorial efforts have been executed to identify SCs with broad-spectrum photon absorption,[120,121] targeted band positions,[122] excellent charge carrier transport,[123] and environmental stability.[124,125] Earth-abundant SCs with sufficient properties and n-type or p-type behavior have been developed to function as photoanodes (e.g. $BiVO_4$ or WO_3)[126,127] or photocathodes (e.g. p-Si)[128] and further SCs have been identified with characteristics to act simultaneously as a photoanode and photocathode in PPC processes for water splitting (e.g. GaN:ZnO).[129]

Considerable research has also been dedicated to designing electrochemical catalysts that can drive the HER and OER at low overpotentials.[130] The overpotential of a catalyst is the required potential to make the entire reaction pathway downhill in energy. Thus, this is

an inherent measurement of the electrocatalytic reactivity of a material. Insights into surface chemical properties of catalytic materials that optimize performance for HER and OER under electrochemical environments have been developed, allowing for the design of earth-abundant catalysts with relatively low required overpotentials for water splitting half reactions (e.g. MoS_2 for HER and Ni_xFe_yOOH for OER).[112,131] However, only a few studies exist that systematically examine charge transfer from SC to CC under relevant PPC or PEC reaction conditions to identify how characteristics of SC|CC junctions influence the performance of solar water splitting technologies.[110,132,133] This raises a simple question: Can the extensive studies that have been executed to identify optimal HER and OER catalysts in electrochemical environments be exploited to predict their reactivity in PEC/PPC systems that provide charge carriers via charge transfer across the SC|CC junction, rather than directly from a conductive support?

Here we report on the reactivity of SC|CC junctions for OER in a PPC geometry of CC nanoparticles (IrO_x, CoO_x, RuO_x, NiO_x and MnO_x) deposited on n-type SC particles (SnO_2, ZnO, and $BiVO_4$). The reactivity of these SC|CC junctions for OER exhibited significant variations compared to trends expected from electrochemical measurements of CC reactivity. Furthermore, trends in the CC reactivity varied significantly when comparing the relative reactivity of each CC on different SCs. The results strongly suggest that for SC|CC junctions formed between oxide components in PPC OER systems, the reactivity of the junction is significantly influenced by SC supplied overpotential, in combination with CC electrical conductivity, that together control charge transport efficiency across the SC|CC junction and ultimately OER rate. Essentially, interfacial

effects at the SC|CC junction significantly control the rate of OER, rather than the inherent CC reactivity measured under electrochemical environments.[134,135] These studies highlight the need for detailed interfacial analysis at oxide CC and oxide SC junctions on PPC, and perhaps PEC, to optimize OER performance.

1.8 Dissertation Summary

This dissertation was prepared from combining a variety of characterization techniques, both *in-situ* and *ex-situ,* with creative experimental testing to design optimal heterogeneous catalysts and photocatalysts. The main focus was to investigate the effect of catalyst geometry and the interactions between metal catalyst and support on CO_2 reduction selectivity. An additional focus was to look at the interaction between oxide cocatalyst and semiconductor support and how it affects the various aspects of photocatalytic water splitting, specifically the oxygen evolution reaction.

Chapter 2 reviews the major synthesis, materials characterization, and catalyst reactivity experimental methods developed and employed throughout this dissertation. Due to the nature of this dissertation focusing more on exploring fundamentals inherent with simple impregnated catalysts, a majority of the methods discussed here are related to the catalyst characterization and reactivity methods, which were interdependently performed to maximize relevance between the two.

In chapter 3, the role of isolated Rh atoms in the CO_2 reduction reaction pathways are discussed. First, a quantitative DRIFTS method is developed to quantify the fraction of exposed Rh atoms available for driving reactions in the isolated site geometry compared to the Rh atoms on the surface of Rh NP's. These site fractions are then compared to reactivity

data to determine site-specific reactivity, where isolated Rh atoms are determined to drive CO production and Rh NP sites are found to drive CO_2 methanation. These assignments are further tested and supported via selectively removing Rh NP sites and observing the corresponding loss in CH_4 production. Instability is observed at CO_2:H_2 reactant ratios > 1, where CH_4 production is observed to decrease with time-on-stream, however a near proportionate increase in CO production is observed, suggesting the CH_4-producing Rh NP's are converting into CO-producing isolated Rh sites.

Chapter 4: Optimization of supported metal catalysts predominantly focuses on engineering the metal site, where physical insights based on extensive theoretical and experimental contributions have enabled rational design of active sites. While it is well known that supports can influence the catalytic properties of metals, physically transparent insights into how metal-support interactions can be exploited to optimize metal active site properties are lacking. In this chapter, we utilize *in-situ* spectroscopy and microscopy to identify and characterize a support-effect in oxide-supported heterogeneous Rh catalysts, where strongly bound adsorbates (HCO_x) on reducible oxide supports (TiO_2 and Nb_2O_5) induce oxygen-vacancy formation in the support, causing HCO_x functionalized support encapsulation of Rh nanoparticles. The encapsulation layer is permeable to reactants, stable under reaction conditions, and strongly influences the catalytic properties of Rh, enabling rational and dynamic tuning of CO_2 reduction selectivity.

Chapter 5: Photocatalytic water splitting has the potential to provide a sustainable approach for storing the energy of solar photons in the form of chemical bonds. Much work has been executed towards developing semiconducting light absorbers (SC) and co-

catalysts (CC) for photoelectrochemical (PEC) and particulate photocatalytic (PPC) water splitting systems. However, minimal insights exist into how the formation of junctions between highly dispersed CC clusters and nanoparticle SCs influences the reactivity of the system, as compared to the reactivity of the CCs in electrochemical environments. In this work, 15 materials consisting of five different CC nanoclusters deposited on three different nanoparticle SCs were synthesized, characterized, and tested for oxygen evolution reaction (OER) activity. The SCs were chosen based on their similar n-type behavior and low OER activity, and the CCs were chosen based on their benchmarked OER reactivity in electrochemical measurements. We found that the photocatalytic activity of these samples for the OER did not directly correlate with the reactivity of the CCs measured under electrochemical conditions. Instead, the performance was controlled by interfacial effects specific to each SC|CC junction. CC electrical conductivity and SC supplied OER overpotential were the major factors identified to strongly affect OER rate. This work suggests that when designing an optimal photocatalyst, one can not simply deposit the most active CC (as measured in electrochemical conditions) on the SC which absorbs the highest fraction of the solar flux, as the CC-SC pairing requires critical interfacial considerations.

In chapter 6, we discuss the main conclusions of the dissertation and their utility in the field. Additionally, we cover potentially continuations or follow-up studies to the work described in this dissertation.

1.9 References

1 J. Anderson and M. Boudart, *Catal. Sci. Technol.*, 1981, **1**, 1–41.

2 N. Am. Cat. Soc., http://nacatsoc.org/educational/about-catalysis/, (accessed April 2016).

3 R. L. BURWELL, 1983, pp. 3–12.

4 J. K. Laylin, *Nobel Laureates in chemistry, 1901-1992*, Chemical Heritage Foundation, 1993.

5 M. Appl, *Ullmann's Encycl. Ind. Chem.*, 2006, 153.

6 L. E. Apodaca, *Mineral commodity summaries*, Reston, Virginia, 2016.

7 V. Smil, *Nature*, 1999, **400**, 415.

8 H. Schulz, *Appl. Catal. A Gen.*, 1999, **186**, 3–12.

9 P. L. Spath and D. C. Dayton, *Preliminary Screening -- Technical and Economic Assessment of Synthesis Gas to Fuels and Chemicals with Emphasis on the Potential for Biomass-Derived Syngas*, 2003.

10 R. Snel, *Catal. Letters*, 1988, 327–330.

11 R. P. Fletcher, *ACS Symp. Ser.*, 2009, **1000**, 189–249.

12 American Chemical Society National Historic Chemical Landmarks. The Houdry Process for Catalytic Cracking. at <http://www.acs.org/content/acs/en/education/whatischemistry/landmarks/houdry.html>

13 M. Shelef and R. W. McCabe, *Catal. today*, 2000, **62**, 35–50.

14 H. S. Gandhi, G. W. Graham and R. W. McCabe, *J. Catal.*, 2003, **216**, 433–442.

15 M. van der Hoeven, Y. Kobayashi and R. Diercks, *Technology Roadmap Energy and GHG Reductions in the Chemical Industry via Catalytic Processes*, 2013.

16 E. McCarthy, J. Zahradnik, G. C. Kuczynski and J. J. Carberry, *J. Catal.*, 1975, **39**, 29–35.

17 N. Lopez, T. V. W. Janssens, B. S. Clausen, Y. Xu, M. Mavrikakis and T. Bligaard, *J. Catal.*, 2004, 232–235.

18 M. Haruta, S. Tsubota, T. Kobayashi and H. Kageyama, *J*., 1993.

19 T. Inoue, T. Iizuka and K. Tanabe, *Appl. Catal*., 1989, **46**, 1–9.

20 A. Trovarelli, C. Mustazza, G. Dolcetti, J. Kasˇpar and M. Graziani, *Appl. Catal*., 1990, **65**, 129–142.

21 M. R. Gogate and R. J. Davis, *Comparative study of CO and CO2 hydrogenation over supported Rh–Fe catalysts*, 2010, vol. 11.

22 M. D. Porosoff, B. Yan and J. G. Chen, *Energy Environ. Sci*., 2016, DOI: 10.1039/C5EE02657A.

23 P. Panagiotopoulou, D. I. Kondarides and X. E. Verykios, *Appl. Catal. A Gen*., 2008, **344**, 45–54.

24 R. A. Dictor and A. T. Bell, 1986, **136**, 121–136.

25 N. Fischer, E. van Steen and M. Claeys, *J. Catal*., 2013, **299**, 67–80.

26 Ammonia, the substance that changed the world, http://www.ini-europe.org/node/16, (accessed April 2016)

27 K. Honkala, a Hellman, I. N. Remediakis, a Logadottir, a Carlsson, S. Dahl, C. H. Christensen and J. K. Nørskov, *Science*, 2005, **307**, 555–8.

28 A. Logadottir, T.H. Rod, J.K. Nørskov, B. Hammer, S. Dahl and C. J.H. Jacobsen, *J. Catal*., 2001, **197**, 229–231.

29 F. Sabatier, *La catalyse en chimie organique*, Berauge, Paris, 1920.

30 A. A. Balandin, *Adv. Catal*., 1969, **19**, 1–210.

31 T. Bligaard, J. K. Nørskov, S. Dahl, J. Matthiesen, C. H. Christensen and J. Sehested, *J. Catal*., 2004, **224**, 206–217.

32 J. K. Nørskov, T. Bligaard, A. Logadottir, S. Bahn, L. B. Hansen, M. Bollinger, H. Bengaard, B. Hammer, Z. Sljivancanin, M. Mavrikakis, Y. Xu, S. Dahl and C. J. H. Jacobsen, 2002, **278**, 275–278.

33 V. Pallassana and M. Neurock, *J. Catal*., 2000, **191**, 301–317.

34 J. N. Bronsted, *Chem. Rev*., 1928, **5**, 231–338.

35 M. G. Evans and M. Polanyi, *Trans. Faraday Soc*., 1938, **34**, 11.

36 B. Hammer and J. K. Nørskov, in *Advances in Catalysis*, 2000, vol. 45, pp. 71–129.

37 T. Bligaard and J. K. Nørskov, in *Chemical Bonding at Surfaces and Interfaces*, Elsevier, 2008, pp. 255–321.

38 M. P. Andersson, I. N. Remediakis, T. Bligaard, G. Jones, O. Lytken, S. Horch, J. H. Nielsen, J. Sehested and I. Chorkendorff, *J. Catal.*, 2008, **255**, 6–19.

39 J. K. Nørskov, T. Bligaard, B. Hvolbaek, F. Abild-Pedersen, I. Chorkendorff and C. H. Christensen, *Chem. Soc. Rev.*, 2008, **37**, 2163–71.

40 M. Boudart and G. Djega-Mariadassou, *Kinetics of Heterogeneous Catalytic Reactions*, Princeton University Press, Princeton, 1984.

41 M. Behrens, F. Studt, I. Kasatkin, S. Kühl, M. Hävecker, F. Abild-Pedersen, S. Zander, F. Girgsdies, P. Kurr, B.-L. Kniep, M. Tovar, R. W. Fischer, J. K. Nørskov and R. Schlögl, *Science*, 2012, **336**, 893–897.

42 U. States, *IPCC*, 2000, 1990–1998.

43 W. Wang, S. Wang, X. Ma and J. Gong, *Chem. Soc. Rev.*, 2011, **40**, 3703–27.

44 M. Gangeri, S. Perathoner, S. Caudo, G. Centi, J. Amadou, D. Bégin, C. Pham-Huu, M. J. Ledoux, J.-P. Tessonnier, D. S. Su and R. Schlögl, *Catal. Today*, 2009, **143**, 57–63.

45 S. Perathoner and G. Centi, *ChemSusChem*, 2014, **7**, 1274–1282.

46 R. M. Zubrin, A. C. Muscatello and M. Berggren, *J. Aerosp. Eng.*, 2013, **26**, 43–56.

47 A. Trovarelli, C. Mustazza, G. Dolcetti, J. Kasˇpar and M. Graziani, *Appl. Catal.*, 1990, **65**, 129–142.

48 J. H. Kwak, L. Kovarik and J. Szanyi, *ACS Catal.*, 2013, **3**, 2449–2455.

49 T. Riedel, G. Schaub, K.-W. Jun and K.-W. Lee, 2001, **40**, 1355–1363.

50 J. H. Kwak, L. Kovarik and J. Szanyi, *ACS Catal.*, 2013, **3**, 2094–2100.

51 C. Deleitenburg and A. Trovarelli, *J. Catal.*, 1995, **156**, 171–174.

52 M. Levin, M. Salmeron, A. T. Bell and G. A. Somorjai, *Surf. Sci.*, 1986, **169**, 123–137.

53 A. Boffa, C. Lin, A. T. Bell and G. A. Somorjai, *J. Catal.*, 1994, **149**, 149–158.

54 A. C. Yang and C. W. Garland, *J. Phys. Chem.*, 1957, **61**, 1504–1512.

55 J. T. Yates Jr., T. M. Duncan, S. D. Worley and R. W. Vaughan, *J. Chem. Phys.*, 1979, **70**, 1219.

56 M. J. Lundwall, S. M. McClure and D. W. Goodman, *J. Phys. Chem. C*, 2010, **114**, 7904–7912.

57 T. M. Duncan, J. T. Yates Jr. and R. W. Vaughan, *J. Chem. Phys.*, 1980, **73**, 975.

58 J. T. Cavanagh, R. R., Yates Jr., *J. Chem. Phys.*, 1981, **74**, 4150.

59 J. T. Yates, T. M. Duncan and R. W. Vaughan, *J. Chem. Phys.*, 1979, **71**, 3908–3915.

60 Basu, P., Panayotov, D., Yates, J.T. Jr., *J. Am. Chem. Soc.*, 1988, **110**, 2074–2081.

61 G. Me and F. Solymosi, 1996, **2**, 17732–17734.

62 F. Solymosi and M. Pásztor, *J. Phys. Chem.*, 1986, **90**, 5312–5317.

63 F. Solymosi and M. Pdsztor, *J. Phys. Chem.*, 1985, **89**, 4789–4793.

64 G. Kyriakou, M. B. Boucher, A. D. Jewell, E. A Lewis, T. J. Lawton, A. E. Baber, H. L. Tierney, M. Flytzani-Stephanopoulos and E. C. H. Sykes, *Science*, 2012, **335**, 1209–12.

65 Q. Fu, H. Saltsburg and M. Flytzani-Stephanopoulos, *Science*, 2003, **301**, 935–8.

66 M. Flytzani-Stephanopoulos, *Acc. Chem. Res.*, 2014, **47**, 783–92.

67 P. Serna and B. C. Gates, *J. Am. Chem. Soc.*, 2011, **133**, 4714–7.

68 P. Serna and B. C. Gates, *Angew. Chemie*, 2011, **123**, 5642–5645.

69 F. Boccuzzi, A. Chiorino, M. Manzoli, D. Andreeva and T. Tabakova, *J. Catal.*, 1999, **185**, 176–185.

70 Q. Fu, W. Deng, H. Saltsburg and M. Flytzani-Stephanopoulos, *Appl. Catal. B Environ.*, 2005, **56**, 57–68.

71 Q. Fu, S. Kudriavtseva, H. Saltsburg and M. Flytzani-Stephanopoulos, *Chem. Eng. J.*, 2003, **93**, 41–53.

72 Z.-P. Liu, S. Jenkins and D. King, *Phys. Rev. Lett.*, 2005, **94**, 196102.

73 M. Yang, L. F. Allard and M. Flytzani-Stephanopoulos, *J. Am. Chem. Soc.*, 2013, **135**, 3768–3771.

74 J. Lin, B. Qiao, N. Li, L. Li, X. Sun, J. Liu, X. Wang and T. Zhang, *Chem. Commun.*, 2015, **51**, 7911–7914.

75 S. Abbet, A. Sanchez, U. Heiz, W.-D. Schneider, A. M. Ferrari, G. Pacchioni and N. Rösch, *J. Am. Chem. Soc.*, 2000, **122**, 3453–3457.

76 H. Wei, X. Liu, A. Wang, L. Zhang, B. Qiao, X. Yang, Y. Huang, S. Miao, J. Liu and T. Zhang, *Nat. Commun.*, 2014, **5**, 5634.

77 J. Xing, J. F. Chen, Y. H. Li, W. T. Yuan, Y. Zhou, L. R. Zheng, H. F. Wang, P. Hu, Y. Wang, H. J. Zhao, Y. Wang and H. G. Yang, *Chem. - A Eur. J.*, 2014, **20**, 2138–2144.

78 E. J. Peterson, A. T. DeLaRiva, S. Lin, R. S. Johnson, H. Guo, J. T. Miller, J. Hun Kwak, C. H. F. Peden, B. Kiefer, L. F. Allard, F. H. Ribeiro and A. K. Datye, *Nat. Commun.*, 2014, **5**, 4885.

79 J. C. Fierro-Gonzalez, S. Kuba, Y. Hao and B. C. Gates, *J. Phys. Chem. B*, 2006, **110**, 13326–13351.

80 J. C. Matsubu, V. N. Yang and P. Christopher, *J. Am. Chem. Soc.*, 2015, **137**, 3076–3084.

81 P. Christopher and S. Linic, *J. Am. Chem. Soc.*, 2008, **130**, 11264–11265.

82 F. Studt, I. Sharafutdinov, F. Abild-Pedersen, C. F. Elkjær, J. S. Hummelshøj, S. Dahl, I. Chorkendorff and J. K. Nørskov, *Nat. Chem.*, 2014, **6**, 320–324.

83 F. Calle-Vallejo, T. Jakub, V. Colic, P. Sautet, J. Tymoczko, V. Colic, Q. H. Vu, M. D. Pohl, K. Morgenstern, D. Loffreda, P. Sautet, W. Schuhmann and A. S. Bandarenka, *Science*, 2015, **350**, 185–189.

84 A. Holewinski, J.-C. Idrobo and S. Linic, *Nat. Chem.*, 2014, **6**, 828–834.

85 J. Graciani, K. Mudiyanselage, F. Xu, A. E. Baber, J. Evans, S. D. Senanayake, D. J. Stacchiola, P. Liu, J. Hrbek, J. F. Sanz and J. A. Rodriguez, *Science*, 2014, **345**, 546–550.

86 J. A. Farmer and C. T. Campbell, *Science*, 2010, **329**, 933–936.

87 T. Ioannides and X. E. Verykios, *J. Catal.*, 1996, **161**, 560–569.

88 A. Bruix, J. a Rodriguez, P. J. Ramírez, S. D. Senanayake, J. Evans, J. B. Park, D. Stacchiola, P. Liu, J. Hrbek and F. Illas, *J. Am. Chem. Soc.*, 2012, **134**, 8968–8974.

89 C. T. Campbell, *Nat. Chem.*, 2012, **4**, 597–598.

90 Y. Lykhach, S. M. Kozlov, T. Skála, A. Tovt, V. Stetsovych, N. Tsud, F. Dvořák, V. Johánek, A. Neitzel, J. Mysliveček, S. Fabris, V. Matolín, K. M. Neyman and J. Libuda, *Nat. Mater.*, 2015, **15**, 284–288.

91 J. Saavedra, H. A. Doan, C. J. Pursell, L. C. Grabow and B. D. Chandler, *Science*, 2014, **345**, 1599–1602.

92 I. X. Green, W. Tang, M. Neurock and J. T. Yates Jr., *Science*, 2011, **333**, 736–739.

93 S. J. Tauster, S. C. Fung and R. L. Garten, *J. Am. Chem. Soc.*, 1978, **100**, 170–175.

94 S. J. Tauster, *Acc. Chem. Res.*, 1987, **20**, 389–394.

95 O. Dulub, W. Hebenstreit and U. Diebold, *Phys. Rev. Lett.*, 2000, **84**, 3646–3649.

96 A. K. Datye, D. S. Kalakkad, M. H. Yao and D. J. Smith, *J. Catal.*, 1995, **155**, 148–153.

97 G. L. Haller and D. E. Resasco, *Adv. Catal.*, 1989, **36**, 173–235.

98 M. G. Willinger, W. Zhang, O. Bondarchuk, S. Shaikhutdinov, H. J. Freund and R. Schlögl, *Angew. Chemie - Int. Ed.*, 2014, **53**, 5998–6001.

99 S. Sakellson, M. McMillan and G. L. Haller, *J. Phys. Chem.*, 1986, **90**, 1733–1736.

100 T. Uchijima, *Catal. Today*, 1996, **28**, 105–117.

101 M. A. Vannice and B. Sen, *J. Catal.*, 1989, **115**, 65–78.

102 X. Y. Shi, W. Zhang, C. Zhang, W. T. Zheng, H. Chen and J. G. Qi, *J. Microsc.*, 2015, **00**, 1–13.

103 S. Bernal, J. J. Calvino, M. A. Cauqui, J. M. Gatica, C. López Cartes, J. A. Pérez Omil and J. M. Pintado, *Catal. Today*, 2003, **77**, 385–406.

104 A. Fujishima and K. Honda, *Nature*, 1972, **238**, 37–38.

105 G. N. Schrauzer and T. D. Guth, *J. Am. Chem. Soc.*, 1977, **99**, 7189–7193.

106 K. Maeda, *J. Photochem. Photobiol. C Photochem. Rev.*, 2011, **12**, 237–268.

107 K. Maeda, K. Teramura, D. Lu, T. Takata, N. Saito, Y. Inoue and K. Domen, *Nature*, 2006, **440**, 295.

108 D. M. Fabian, S. Hu, N. Singh, F. A. Houle, T. Hisatomi, K. Domen, F. E. Osterloh and S. Ardo, *Energy Environ. Sci.*, 2015, **8**, 2825–2850.

109 F. A. Frame, T. K. Townsend, R. L. Chamousis, E. M. Sabio, T. Dittrich, N. D. Browning and F. E. Osterloh, *J. Am. Chem. Soc.*, 2011, **133**, 7264–7.

110 M. T. Uddin, Y. Nicolas, C. Olivier, T. Toupance, M. M. Müller, H.-J. Kleebe, K. Rachut, J. Ziegler, A. Klein and W. Jaegermann, *J. Phys. Chem. C*, 2013, **117**, 22098–22110.

111 M. T. Uddin, Y. Nicolas, C. Olivier, T. Toupance, L. Servant, M. M. Müller, H.-J. Kleebe, J. Ziegler and W. Jaegermann, *Inorg. Chem.*, 2012, **51**, 7764–7773.

112 L. Trotochaud, S. L. Young, J. K. Ranney and S. W. Boettcher, *JACS,* 2014, **136**, 6744–6753.

113 M. S. Burke, L. J. Enman, A. S. Batchellor, S. Zou and S. W. Boettcher, *Chem. Mater.*, 2015, **27**, 7549–7558.

114 D. G. Nocera, *Acc. Chem. Res.*, 2012, **45**, 767–76.

115 M. G. Walter, E. L. Warren, J. R. McKone, S. W. Boettcher, Q. Mi, E. A. Santori and N. S. Lewis, *Chem. Rev.*, 2010, **110**, 6446–6473.

116 K. Domen, S. Naito, M. Soma, T. Onishi and K. Tamaru, *J. Chem. Soc. Chem. Comm.*, 1980, 543–544.

117 S. Sato and J. M. White, *Ind. Eng. Chem. Prod. Res. Dev.*, 1980, **19**, 542–544.

118 P. J. Boddy, *J. Electrochem. Soc.*, 1968, **115**, 199–203.

119 B. A. Pinaud, J. D. Benck, L. C. Seitz, A. J. Forman, Z. Chen, T. G. Deutsch, B. D. James, K. N. Baum, G. N. Baum, S. Ardo, H. Wang, E. Miller and T. F. Jaramillo, *Energy Environ. Sci.*, 2013, **6**, 1983–2002.

120 K. Lee, B. M. Tienes, M. B. Wilker, K. J. Schnitzenbaumer and G. Dukovic, *Nano Lett.*, 2012, **12**, 3268–3272.

121 J. Choi, H. Park and M. R. Hoffmann, *J. Mater. Res.*, 2010, **25**, 149–158.

122 X. Yong and M. A. A. Schoonen, *Am. Mineral.*, 2000, **85**, 543–556.

123 H. Park, H. Kim, G. Moon and W. Choi, *Energy Environ. Sci.*, 2016, **9**, 411–433.

124 M. R. Singh, K. Papadantonakis, C. Xiang and N. S. Lewis, *Energy Environ. Sci.*, 2015, **8**, 2760–2767.

125 D. G. Nocera, *Acc. Chem. Res.*, 2012, **45**, 767–776.

126 T. W. Kim and K.-S. Choi, *Science*, 2014, **343**, 990–994.

127 G. Hodes, D. Cahen and J. Manassen, *Nature*, 1976, **260**, 312–313.

128 A. B. Bocarsly, D. C. Bookbinder, R. N. Dominey, N. S. Lewis and M. S. Wrighton, *J. Am. Chem. Soc.*, 1980, **102**, 3683–3688.

129 K. Maeda, T. Takata, M. Hara, N. Saito, Y. Inoue, H. Kobayashi and K. Domen, *J. Am. Chem. Soc.*, 2005, **127**, 8286–8287.

130 I. C. Man, H.-Y. Su, F. Calle-Vallejo, H. A. Hansen, J. I. Martínez, N. G. Inoglu, J. Kitchin, T. F. Jaramillo, J. K. Nørskov and J. Rossmeisl, *ChemCatChem*, 2011, **3**, 1159–1165.

131 T. F. Jaramillo, K. P. Jørgensen, J. Bonde, J. H. Nielsen, S. Horch and I. Chorkendorff, *Science*, 2007, **317**, 100–102.

132 F. Lin, B. F. Bachman and S. W. Boettcher, *J. Phys. Chem. Lett.*, 2015, **6**, 2427–2433.

133 Y. Ping, W. A. I. Goddard and G. A. Galli, *J. Am. Chem. Soc.*, 2015, **137**, 5264–5267.

134 K. A. Stoerzinger, L. Qiao, M. D. Biegalski and Y. Shao-Horn, *J. Phys. Chem. Lett.*, 2014, **5**, 1636–1641.

135 Z. Chen, C. X. Kronawitter and B. E. Koel, *Phys. Chem. Chem. Phys.*, 2015, **17**, 29387–29393.

Chapter 2 Experimental Methods

2.1 Summary

This chapter reviews the major synthesis, materials characterization, and catalyst reactivity experimental methods developed and employed throughout this dissertation. Due to the nature of this dissertation focusing more on exploring fundamentals inherent with simple impregnated catalysts, a majority of the methods discussed here are related to the catalyst characterization and reactivity methods, which were interdependently performed to maximize relevance between the two.

2.2 Introduction

To gain insights of the atomic level interactions necessary for understanding catalytic phenomena well enough to improve catalytic processes on a global scale, it is very important to diligently develop and perform experimental methods in a manner best suited for the experiment at-hand, as there are: reaction, materials, and equipment-specific intricacies and exceptions to every method. This dissertation explores the catalytic role of: isolated Rh sites, novel reaction environment-dependent strong metal support interactions, and interfacial effects at heterojunctions, for which all three of these studies involved very simple synthesis techniques but intensive characterization and reactivity experimentation. An assortment of characterization techniques was used to investigate the physical and electronic structures of both the support and metal/metal oxide catalysts in both *ex-situ* and *in-situ* modes. Two setups were used for testing catalytic reactivity for continuous packed bed reactor experimentation of thermal CO_2 reduction catalysis and liquid phase photocatalytic water splitting in a batch reactor. The utility, specific apparatuses, and specific protocols are described below.

2.2.1 Catalyst Synthesis

2.2.1.1 Incipient Wetness Impregnation Technique

The incipient wetness or dry impregnation synthesis technique that was primarily employed in this dissertation is probably the simplest technique for depositing a metal catalyst onto a metal oxide support. While this technique lacks catalyst particle shape control and a narrow particle size distribution, it was selected for its simplicity and prevalence in the catalysis field. In addition, we tried to use only metal nitrate precursors to avoid any residual precursor (e.g. Cl or Na) from affecting catalyst reactivity. The following synthesis protocol was followed for all three studies.

In a typical synthesis, the proper mass of catalyst precursor to attain the desired weight loading was dissolved and stirred in an evaporation dish with a pre-determined volume of distilled water to produce a very thick slurry consistency for these non-porous supports. An appropriate amount of support was added to the aqueous metal catalyst solution and mixed with a stir rod until homogeneous in appearance. The resulting mixture was dried at 90 °C under vacuum for at least 4 hours, and was then ground with a mortar and pestle. The samples were further calcined and reduced as specified in the following sections.

2.2.1.2 Rh metal catalyst synthesis

All Rh catalysts were calcined at 450 ˚C in air for 4 hours and were then reduced *in-situ* for 1 hour at 250 ˚C - 450 ˚C in H_2 before catalytic testing or *in-situ* characterizations.

2.2.1.3 Materials for these syntheses:

The only Rh precursor used for the Rh metal catalyst was Rh Nitrate Hydrate ($Rh(NO_3)_3 \cdot xH_2O$, Sigma-Aldrich-#83750. Supports used in the thermal catalysis experiments were all non-porous metal oxides: TiO_2 (Evonik-P25, 52 m^2/g)), γ-Al_2O_3 (Inframat Advanced Materials-#26R-0804UPG, 83 m^2/g), CeO_2 (Sigma-Aldrich-#544841, 63 m^2/g), and Nb_2O_5 (CBMM-HY 340, 122 m^2/g).

2.2.2 Metal Oxide co-catalyst synthesis

The metal oxide samples were calcined in air at 400-550 ˚C to attain the desired crystal structure as shown in Table 2.1.

Table 2.1 Calcination conditions for desired co-catalyst crystal structure

Metal Oxide	Desired Structure	Temperature (˚C)	Time (hours)
IrO_x	Rutile	550	5
NiO_x	Rock Salt	400	3
MnO_x	Rutile	400	2
RuO_x	Rutile	400	6
CoO_x	Spinel	500	2

Materials:

Metal oxide catalyst precursors: cobalt(II) nitrate hexahydrate (cat. 203106), nickel(II) nitrate hexahydrate (cat. 203874), ruthenium(III) nitrosyl nitrate (cat. 373567), manganese(II) nitrate hydrate (cat. 203742), and iridium(III) chloride hydrate (203491) were purchased from Sigma-Aldrich. Precursors for the $BiVO_4$ nanoparticle support consisted of bismuth nitrate pentahydrate (cat. 467839), ethylenediaminetetraacetic acid

(EDTA) (cat. E9884), and ammonium metavanadate (cat. 10028) from Sigma-Aldrich and used in an EDTA-modified hydrothermal process to synthesize $BiVO_4$.[1] ZnO (cat. 5810HT) and SnO_2 (cat. NS6130-03-349) nanoparticle SC supports were obtained from NanoAmor and Nanoshel respectively.

2.3 Catalyst Characterization Techniques

2.3.1 Static Volumetric Physical Adsorption

In heterogeneous catalysis, it is important to know support surface area, pore volume, and pore distribution to determine the optimal weight loading, aid with synthesis, and predict reactant transport within catalyst pores. Vapor phase physical adsorption is performed under vacuum at the N_2 boiling point (77K) by measuring the relative pressure of a sample tube and plotting vs the volume of dosed N_2 gas. The BET model is then applied to the plot known as an adsorption isotherm to determine the volume of N_2 that physically adsorbed to the sample. For this work, a Micromeritics ASAP 2020 was used to determine the surface areas. The samples were degassed *in-situ* at 350 °C under vacuum for 3 hours and cooled to 35 °C under vacuum prior to analysis.

2.3.2 Static Volumetric Chemical Adsorption

It is important to measure the total exposed metal catalyst surface area or total number of exposed metal catalyst atoms to compare catalyst reactivity on a per catalyst site basis, indicating the inherent activity per catalyst site. This per catalyst site basis is typically referred to as turnover frequency (TOF) and is of the units: product molecules per catalyst site per time. Volumetric chemical adsorption is performed in a similar manner to physical adsorption, with the main differences being that adsorption occurs at ambient

room temperature, the adsorbing gases chemically bind to metal surfaces (e.g, CO, H_2 , etc.) and there are two adsorption isotherms. After reducing the sample, it is cooled under vacuum and then undergoes two cycles of dosing to produce two adsorption isotherms. The first represents both the reversibly physical adsorption to all non-metal surfaces, and the irreversible chemically adsorption to the metal catalyst nanoparticles. Upon evacuation after the first isotherm, all of the physically adsorbed adsorbates are removed, and the second isotherm only represents physical adsorption. The difference in adsorption between the two isotherms represents the chemical adsorption which can then be used to determine the total number of exposed metal atoms, metal dispersion, and even an average metal particle size.

Volumetric CO chemisorption analyses were performed with a Micromeritics ASAP 2020. Catalysts were packed in a quartz tube sample holder and heated in H_2 at a heating rate of 10 °C/min to 350 °C with a reduction time at 350 °C of 1 hour. The sample was evacuated at 350 °C for 10 minutes and cooled to 35 °C under vacuum prior to CO chemisorption analysis. The two CO adsorption isotherms were performed (at 35 °C and from 100-450 mmHg) with an evacuation step between the two to remove physisorbed CO. An assumed ratio of 1 CO molecule per surface Rh atom was used to convert the number of chemisorbed CO molecules into the number of surface Rh atoms. This value was corrected using DRIFTS to account for CO adsorption geometries with non 1:1 CO:Rh ratios.

2.3.3 X-ray Diffraction (XRD)

XRD is used to determine the crystal structure and crystallite size of materials and distinguishes between crystalline and amorphous materials on both bulk and powder samples. Incident x-rays diffract off crystalline planes at particular angles which can be converted to d spacings, for which each crystal structure has its own set of d spacings. In our work, a generator voltage of 45 kV and emission current of 40 mA were employed. The scanning range was 10–70° (2θ) with a step size of 0.10° and a step time of .0275 s. The phases were determined by identifying the top matching score between each XRD spectrum and known library peak positions with PANalytical Highscore software.

2.3.4 Diffuse reflectance infrared Fourier transform spectroscopy (DRIFTS)

IR spectroscopy has proven to be a primary characterization method in the heterogeneous catalysis field, by providing surface chemistry information regarding both the catalyst geometry and chemically bound species at the catalyst surface. The low energy nature of IR radiation allows a catalyst to be investigated *in-situ* or operando without destroying the sample or interfering with catalyst performance. Frequencies exhibited by the mid-range IR (MIR) region utilized in these spectrometers match the vibrational bond frequencies of most molecules, therefore via bond-specific IR absorption, a plethora of molecules can be identified by their IR fingerprint comprised of several different IR peaks representing bonds. As various states such as charge, binding to different moieties or metals, and repulsion in local environments can change molecular vibrational frequencies, IR spectroscopy provides insight to these variables. In addition, the intensity of the absorbed IR can be related linearly back to the concentration of surface species on a catalyst

through absorbance, Kubelka-Munk, or the Matyschak-Krylov functions depending on the relative reflectance of the sample and the baseline drift.[2]

Rather than utilizing a grating monochromator or spectrograph to analyze the sample in incremental wavelength regions commonly implemented in dispersive spectroscopy techniques, an FTIR spectrometer analyzes all wavelengths simultaneously. The use of a Michelson interferometer allows for: the simultaneous collection of all wavelengths which provides a higher signal to noise ratio at a specific scan time, higher IR throughput with the the removal of monochromator slits which prevent some of the beam throughput, and better wavelength resolution.[3] As shown in Figure 2.1, the interferometer splits incoming coherent light, by reflecting half and transmitting half, into two beams which reflect off of

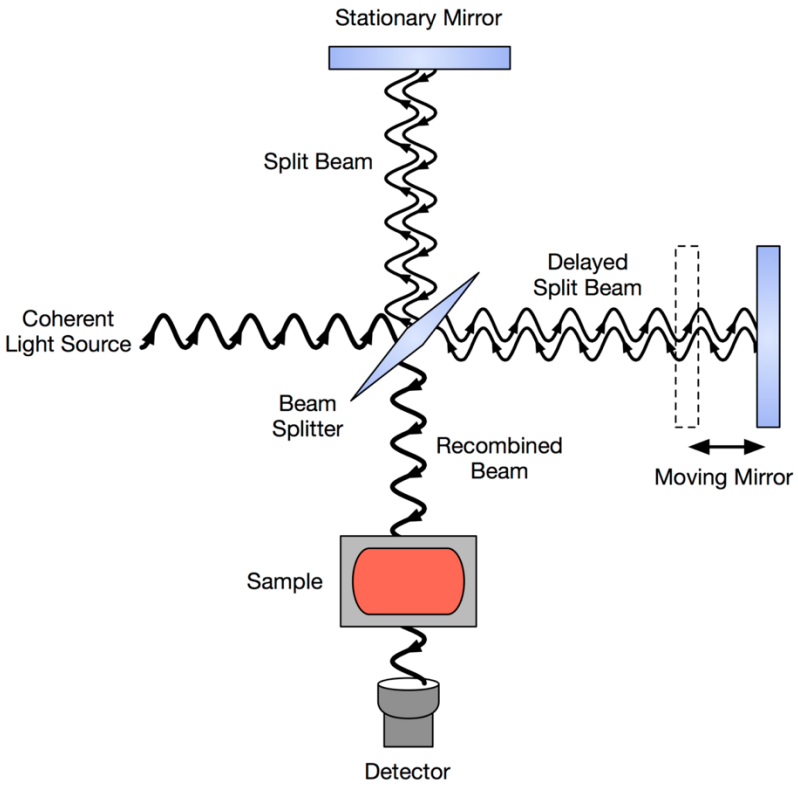

Figure 2.1 Diagram of FTIR Spectrometer with interferometer

mirrors, one being stationary and one moving back and forth to change the distance

between the beam splitter and the moving mirror. The reflected beams then recombine at the beam splitter and are transmitted or reflected to the sample and finally the detector. Due to the changing distance of the beam which reflects from the moving mirror, the recombined beam is the two beams continually interfering with one another at various frequencies. The spectrum collected at the detector is an interferogram which provides data regarding every frequency of the IR source, and upon processing with Fourier transformation the data is converted to a frequency spectrum.

Although there are several IR techniques utilized in heterogeneous catalysis, four of which are shown in Figure 2.2, the two most popular IR modes are transmission-absorption IR (TIR) and diffuse reflectance (DRIFTS)[3]. Each of these techniques can be used to probe the catalyst surface for both ex-situ, *in-situ*, and operando configurations, however there are different advantages and disadvantages between TIR and DRIFTS discussed below.

TIR measures the intensity of IR radiation transmitted through a carefully prepared IR-transparent sample (Figure 2.2), where the Lambert-Beer law applies in relating absorbance to analyte concentration or coverage. TIR can be used to study catalysts *in-situ* and provides quantitative data, however the technique suffers from a more difficult sample preparation and is limited to samples with IR transparency. DRIFTS is another FTIR based technique, which collects the diffusely reflected light from the sample with spherical mirrors. This mode benefits from: a much simpler sample prep in placing catalyst powder into a small cup, a sample that can be opaque to IR light and can have irregular surfaces, and the sample can be run in a packed bed reactor configuration at elevated temperatures and pressures.[3,4] Additionally, DRIFTS can have a higher sensitivity to surface species compare to gas-phase molecules, potentially as a result of the light undergoing multiple

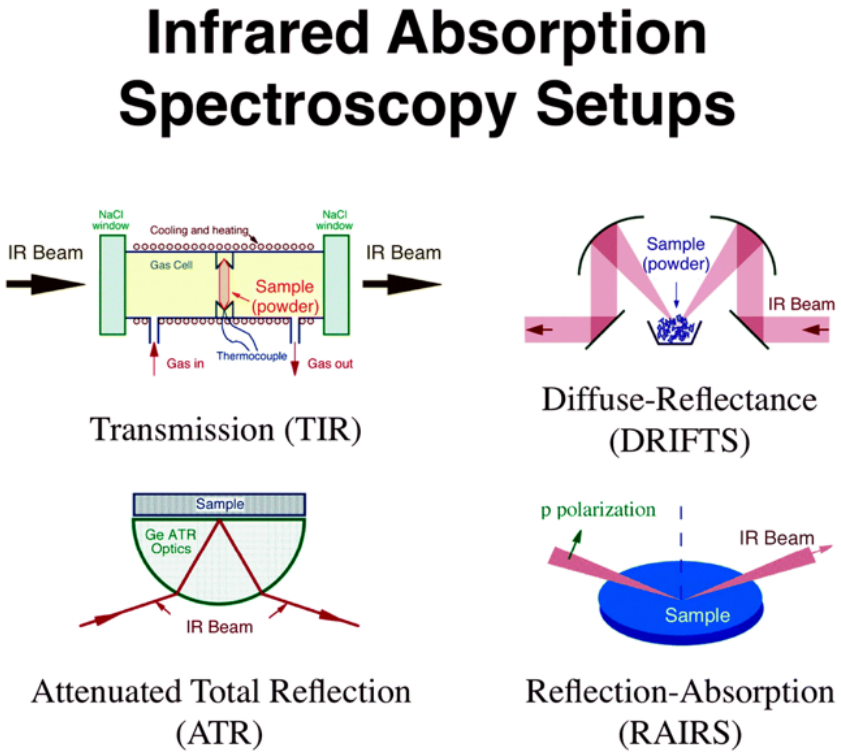

Figure 2.2 Different modes of FTIR analysis used for heterogeneous catalysis. Reproduced with permission from ref. 3.

reflections in the sample prior to being collected.[3] DRIFTS measurements are not without their flaws, as DRIFTS is more difficult to attain consistent quantitative data from one sample to the next and data collection at elevated temperatures can be challenging due to the large temperature gradient inherent to the method.[5] In this dissertation, DRIFTS was the main characterization technique for probing the surface geometry of Rh and to identify adsorbates present on the catalyst surface in reaction conditions and we took careful measures to minimize the inherent flaws associated with DRIFTS.

2.3.5 DRIFTS CO chemisorption for Isolated Site Fraction Quantification

One benefit of characterizing Rh isolated site catalysts via FTIR is the compilation of IR work that has been previously performed on the geometry of Rh.,[6–13] which has shown that CO exhibits vibrational frequencies specific to the Rh geometry. Therefore, CO was used as a probe molecule adsorbed to the catalyst surface at saturation coverages to quantify the fractions of isolated and NP Rh sites.

Catalyst samples were packed into a Harrick Praying Mantis™ high temperature reaction chamber (ZnSe windows) mounted inside of a Thermo Scientific Praying Mantis™ diffuse reflectance adapter, set inside of a Thermo Scientific Nicolet™ iS™10 FT-IR spectrometer. Gases were flowed to the reaction chamber using Teledyne mass flow controllers. This setup was used to quantitatively determine the fraction of isolated Rh (Rh_{iso}) and Rh sites on the surface of Rh NPs (Rh_{NP}) sites on each catalyst. In all measurements, spectra were obtained by averaging 40 sequentially collected scans at a resolution of 4 cm^{-1}. The spectra were obtained in Kubelka-Munk (KM) units, which have been shown to scale linearly with adsorbate concentration.[2] This analysis was used in 3

different applications: quantifying the Rh_{iso} and Rh_{NP} site fractions of freshly prepared reduced catalysts, quantifying the impact of reaction conditions on the relative quantity of site type fractions, and verifying that the CO chemisorption analyses did not significantly alter the site fractions or structure of the samples via disintegration[12,14–16] during the process of characterization.

2.3.6 Site fraction quantification

Approximately 30 mg of pure TiO_2 (Evonik P25) was packed in the reaction chamber (to minimize use of the Rh/TiO_2 samples) and approximately 10 mg of each Rh/TiO_2 sample was then packed on top. For the 4% and 6% Rh weight loading samples, a 1:1 dilution of the top 10 mg of Rh loaded samples with plain TiO_2 was used to improve the signal by reducing absorption. The samples were purged with pure H_2 (99.999%) at 100 sccm for 15 minutes at room temperature and then reduced in pure H_2 at 20 sccm and 350 °C for 1 hour. The reactor was then cooled to room temperature and purged with Ar (99.999%) at 100 sccm for 10 minutes and then a baseline spectrum was taken of the sample. 50 sccm of a 10%CO/90%Ar stream was then introduced to the sample for 10 minutes to allow for complete CO adsorption. The sample was then purged with 100 sccm Ar for 10 minutes and a DRIFT spectrum was acquired to quantitatively determine the fraction of both Rh_{iso} and Rh_{NP} sites. To verify that 10 minutes of CO adsorption was enough time to reach monolayer saturation and examine the stability of the catalysts during the site fraction quantification, the site fractions were also monitored on a per minute basis during the CO exposure and Ar purge steps. The peak intensities, I_i, were determined from de-convolution

using Omnic software and were converted into site fractions using previously determined extinction coefficients[10] for each vibrational mode and the following equation:

$$X_{iso} = \frac{I_{iso}/\left(\epsilon_{iso} \times \left(\frac{CO}{Rh}\right)_{iso}\right)}{\sum_{i=1}^{3}\left[I_i/\left(\epsilon_i \times \left(\frac{CO}{Rh}\right)_i\right)\right]} \quad 1)$$

The three types of CO configurations considered were gem-dicarbonyl (Rh_{iso}), linear (Rh_{NP}), and bridge bound (Rh_{NP}), where the Rh_{iso} sites were quantified based on the intensity of the symmetric gem-dicarbonyl CO stretch. Rh_{NP} site fraction (X_{NP}) was calculated as X_{NP} = 1- X_{iso}. Extinction coefficients, ε_i, used for the symmetric gem-dicarbonyl, linear, and bridge configurations were 74, 26, and 85 (cm/mole)(10^8) respectively.[10] The extinction coefficients were used from an earlier study on Rh/Al_2O_3, where the nature of the support may slightly affect the extinction coefficient, particularly the gem-dicarbonyl species, however the similarity of vibrational frequencies of the gem-dicarbonyl species on the two supports suggests that this difference wouldn't significantly impact our results. The CO:Rh ratios for the symmetric gem-dicarbonyl, linear, and bridge configurations were 2, 1, and 0.5 respectively.

2.3.7 In-Situ Characterization

DRIFTS measurements were executed to identify how the various treatments explored in this study impact the species adsorbed on the catalyst surface in reaction conditions. The same setup utilized for the Rh site fraction quantification was used for all of the *in-situ* DRIFTS analyses. Measurements were taken with 128 scans, 4 cm^{-1} resolution, and a 30-40 standard liters per minute N_2 purge of the spectrometer and Praying

Mantis adapter box to minimize the effect of variations in atmospheric water and CO_2 from falsely appearing in the spectra. Typically, 10 mg of the catalyst sample was packed on top of 100 mg of α-alumina. The reactor effluent was routed to the GC to monitor reactivity of the catalyst and ensure consistent behavior with experiments performed in the packed bed reactors.

After loading the catalysts in the reactor, the following steps were taken for the DRIFTS cycling experiments to identify how the species on the catalyst surface changed under reaction conditions (1%CO_2:1%H_2:98%He, 180 °C) following reduction or other treatments explained in chapter 4.

1. **Reduction:** Pure H_2 flow (20 sccm) over sample at 350 °C* for 1 hour
2. **FTIR Background:** Changed temperature to 180 °C* and collected background spectrum in H_2.
3. **Reactivity Assay:** Changed flows to 1 sccm CO_2, 1 sccm H_2, 98 sccm He and allowed the system 20 minutes to reach steady state prior to collecting a spectrum of the reduced material in reaction conditions.
4. **A-SMSI Formation:** Changed temperature to 210 °C* and flowrates to 20 sccm CO_2, 2 sccm H_2, and 78 sccm He for 16 hours* to induce A-SMSI formation.
5. **Reactivity Assay:** Changed temperature to 180 °C* and flowrates to 1 sccm CO_2, 1 sccm H_2, 98 sccm He and allowed the system 20 minutes to reach steady state prior to collecting a spectrum of the catalyst in reaction conditions and the A-SMSI state.
6. **Re-Reduction:** Pure H_2 flow (20 sccm) over sample at 350 °C* for 4 hour.
7. **Reactivity Assay:** Changed temperature to 180 °C* and flowrates to 1sccm CO_2, 1sccm H_2, 98 sccm He and allowed the system 20 minutes to reach steady state prior to collecting a spectrum of the re-reduced catalyst.

2.3.8 DRIFTS Analysis of CO_2 Removal and TPD Experiments

The goals of this experiment were to observe (a) which surface species were acting as reaction intermediates, (b) the coverage dependence of the CO stretch frequency and (c) in the case of the A-SMSI state, the impact of the HCO_x species on the frequency of the

stretch associated with CO bound to Rh. We only examined the 2% Rh/TiO_2 catalyst in this set of experiments. In the case of the reduced catalyst, CO_2 was removed from the reactant stream and time-resolved DRIFT spectra were collected to identify reactive species and the coverage dependent frequency of the CO stretch, see Figure 4.19. In the case of the catalyst in the A-SMSI state, an identical experiment was performed, followed by a temperature programmed desorption in He. Detailed accounting of the protocol is included in Chapter 4.

2.3.9 UV-Vis Diffuse Reflectance Spectroscopy (UV-Vis DRS)

The UV (200-400 nm) and Visible (400-800nm) wavelength ranges often measure the electronic transitions of a material, in our case, photon absorption in semiconductors (chapter 5). The spectra were collected using diffuse reflectance (section 2.3.4) mode as opposed to transmission, UV-Vis spectroscopy, due to the samples being solid in nature. Therefore, the diffusely reflected light was collected as opposed to the absorbance normally collected in transmission UV-Vis spectroscopy. Diffuse reflectance spectra of the SCs were recorded with a Thermo Scientific Evolution 300 UV-vis spectrophotometer and a Harrick Praying Mantis™ diffuse reflectance accessory. SC band gap energies were determined using the Kubelka– Munk technique.

2.3.10 Transmission Electron Microscopy (TEM)

Transmission electron microscopy is used to image materials down to an atomic level resolution. TEM utilizes an electron beam to pass through a thin sample, which interacts via scattering with the sample nuclei, where the transmitted electrons are then collected by a CCD camera. Scanning transmission electron microscopy (STEM) is a type of TEM with

the beam rastered across the sample, which allows for less beam damage to the sample and the detection of inelestically and back scattered electrons, Auger, and X-ray signals.[17] Many other analyses can be performed within a TEM/STEM system, however in this work Energy-dispersive X-ray spectroscopy (EDS) and electron energy loss spectroscopy (EELS) were the only other analyses performed in conjunction with the TEM/STEM analysis. Both EDS and EELS analyses provide elemental insight through x-ray and inelastically scattered electrons respectively. The micrographs taken for each chapter were obtained using 3 different electron microscopes, two which were STEM and 1 was TEM.

The Rh particle size distributions determined in chapter 3 were taken by a FEI CM300 TEM at Central Facility for Advanced Microscopy and Microanalysis (CFAMM) at UC Riverside, with reduced samples at 300 kV accelerating voltage. After reduction, sample powders were suspended in distilled water using ultrasonication and added dropwise onto a holey carbon-coated copper grid sample holder. Rh particle size distributions were determined by measuring the diameter of at least 100 particles for each sample using ImageJ software.

The oxide cocatalysts supported on oxide semiconductors in chapter 5 were prepared with the same method, however were then characterized using scanning transmission electron microscopy (STEM) imaging, which was performed by Dr. Krassmir Bozhilov at CFAMM in UCR on a FEI Titan Themis 300 instrument equipped with XFEG electron gun, 4k × 4k CETA digital camera, a SuperX EDX system with 4 × 30 mm^2 SDD detectors and 4k × 4k Fischione Instruments Inc. annular dark field detector model 3000. The imaging was coupled with EDS elemental mapping to examine the dispersion of the IrOx

and CoOx CCs on all three SCs to verify that CC dispersion did not play a significant role in observed reactivity trends.

Typically, TEM analysis is performed at ambient temperatures and under ultra-high vacuum conditions, which adds a pressure, temperature, and environmental gap between characterization and reaction conditions. The development of environmental STEM (ESTEM) has bridged much of these gaps by implementing the inclusion of environmental cells with gases and a resistively heated sample holder.[18] In chapter 4, we specifically investigate the effect of reaction conditions, both reactant concentrations and temperature, on an *in-situ* transformation that we had previously observed with time-on-stream.[19] ESTEM analysis was executed on a JEOL 3100R5 with double Cs corrector operated at 300kV and at the same reduction and reaction conditions as performed in the catalytic reactivity experiments. 2%Rh/TiO_2 samples were suspended in methanol via sonication and drop casted onto lacy carbon-on-copper grids for *ex-situ* analysis and a special SiN heater chip for *in-situ* observation, which utilized a Protochips Atmosphere system. To improve the ESTEM and EELS resolution, the sample was first sintered at 800 ˚ for 3 hours to increase the Rh particle size from 1-3nm to 10-50nm and was then analyzed.

Electron Energy Loss Spectroscopy was performed to identify the existence of Ti in the amorphous A-SMSI overlayer and characterize the Ti valance state. EELS data was collected in-situ when the sample was sandwiched between two SiN membranes, with a total thickness of 80nm, using the Gatan #965 Quantum Imaging Filter (GIF). The spot size was 1.0-1.5Å in diameter and typical acquisition time was 10 seconds. The Ti valence

was quantified by using Multiple Linear Least Square (MLLS) Fitting with Digital Micrograph.

2.3.11 X-ray absorption spectroscopy

XAS provides insight to the chemical nature of materials by exploiting the photoelectric effect in usually using high intensity x-rays from a synchotron radiation source to eject core electrons upon photon absorption.[20] XAS is comprised of the complementary techniques in extended x-ray absorption fine structure (EXAFS) and x-ray absorption near edge structure (XANES). EXAFS provides distances, coordination number, and the type of neighboring atom to the absorbing atom. In Chapter 4, XAS experiments were performed and analyzed at Beamline 2-2 at the Stanford Synchrotron Radiation Light source (SSRL) by Nebojsa Marinkovic and were analyzed by George Graham and Xiaoqing Pan. A double-crystal Si (220) monochromator was used to scan X-ray energy from -100 to 200 eV and -200 eV to 1300 eV relative to the Rh K-edge (23,220 eV) for XANES and EXAFS spectra, respectively. About 20 mg of 2% Rh/TiO_2 catalyst was placed in 2.4 mm OD quartz tubes and into a resistance heating-capable Claussen cell[21] with gas flowing through the powder. Data were recorded for an untreated sample at room temperature, at 400 °C in H_2 flow for reduced catalyst and at 250 °C with $20\%CO_2/2\%H_2/78\%$He flow all at 20 mL/min.

2.4 Catalyst Reactivity Experiments

2.4.1 Thermal Reaction Experiments

Simple Thermal Catalysis Reactions

Catalysts were reduced *in-situ* between 250-450 ˚C for 1 h in pure H_2 prior to catalytic testing. All CO_2 reduction reaction rates were measured using 15–30 mg of catalyst at 200 °C in a 1/4" OD borosilicate packed bed reactor operating at atmospheric pressure and running under differential reactor conditions (conversion of limiting reagent <10%) with the effluent quantified by online gas chromatography (SRI MG #3), Figure 2.3. CO_2 was separated from other gases using a Hayesep D column, while H_2, N_2, CH_4, and CO were separated using a molecular sieve (MS13X) packed column. The separated

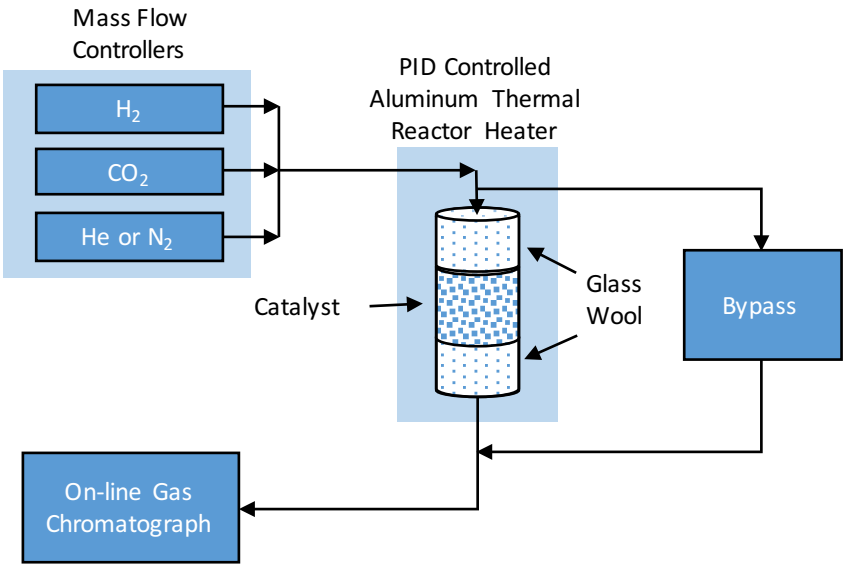

Figure 2.3 Custom-built thermal packed bed reactor experimental setup.

gases were then quantified using a helium ionization detector (HID) or a flame ionization detector (TCD). The total reactant flow rate in all studies was 100 standard cm^3 per minute (sccm). Gases were delivered via Teledyne mass flow controllers. The CO_2:H_2 ratio was varied from stoichiometric methanation conditions, 1:4, to H_2-lean conditions, 10:1, by varying individual flow rates. Inert N_2 or He carrier gases were used at all conditions with a flow rate of greater than 89 sccm. It is important to note that for each reaction condition a fresh sample was loaded into the reactor to ensure each experiment was measuring the reactivity of freshly prepared samples. Reaction rates and selectivity were calculated on the basis of the average of five measurements taken during the first hour on stream.

2.4.1.1 Experimental Setup Automation for Cycling Experiments

Automation aspects were implemented with the thermal reactor setup to improve data throughput and consistency, especially with experiments testing multiple parameters such as temperature, reactant concentrations, and cycling of the catalyst. Temperature of the thermal reactors was controlled via an omega CN7823 PID controller connected to a laptop computer with CN7-A-Process Monitoring and Logger software by Omega Engineering allowing for easy control and monitoring of the pre-treatment and reaction temperature. Gas flow rates were controlled via communication between a Teledyne Powerpod control box and laptop, where the flows were initially input and then sent to the MFC controller power pod box by scripts written in Python programming language. A directional flow solenoid valve was used to switch between sending the reactants directly to the reactor system or bypassing the reactor and sending the reactants to a GC. This bypass option was used before the reactions were run to collect a baseline peak area of the

reactants for determining H_2 or CO_2 conversion and minimizing the experimental error in conversion calculations. Lastly, the GC was used in a continuous manner to take an injection every 10-25 minutes for the entirety of the experiment. The automation was extremely useful in performing the 3-7 day experiments in chapter 4, allowing for very consistent data sampling both day and night.

2.4.2 Photocatalytic Oxygen evolution reaction (OER) experiments

The OER measurements were carried out in 65 ml custom built glass batch reactors. In a typical experiment, 15 mg of catalyst was suspended in distilled water through sonication followed by $AgNO_3$ addition to produce a 50mM $AgNO_3$ solution. Prior to irradiation, the reactor system underwent a series of He (99.999%) purging and high-vacuum pump evacuations to remove O_2 and N_2 from the reaction environment. After 3 sequential purge-evacuation cycles the photo-reactor was pressurized to 10 psig with He to maintain a positive pressure environment and therefore prevent O_2 and N_2 contamination from air. The reactors were left in pure He environment for 30 minutes to allow trace O_2 and N_2 concentrations to equilibrate prior to illumination. The start of the oxygen evolution reaction was signaled by illumination of the reactor with a 100 watt Dolan Jenner MH-100 metal halide lamp with a measured intensity of approximately 640 mW/cm^2. During irradiation, 1 mL gas aliquots of the reactor headspace were drawn every 7-8 minutes with a valved-syringe and quantified using an SRI (MG#3) gas chromatograph equipped with a helium ionization detector (HID) and a thermal conductivity detector (TCD). Special care was taken to maintain strict time consistency between each sample taken and to minimize any effects from atmospheric O_2. N_2 and O_2 concentrations were tracked to account for any

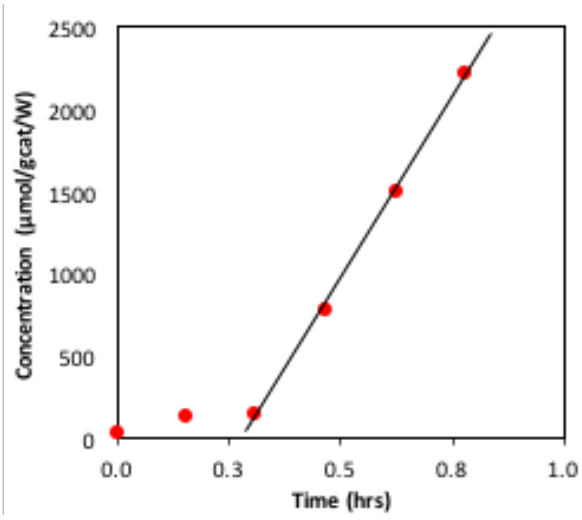

Figure 2.4 O_2 accumulation plot, where slope of accumulation at onset of reactor illumination was used to determine OER rate.

atmospheric O_2 that could be mistaken for evolved O_2, where a simple experimentally determined $3N_2$:O_2 molar ratio was utilized to subtract away atmospheric/non-evolved O_2. Accumulation of evolved O_2 in the reactor headspace was plotted as a function of time and a photocatalytic OER rate, normalized by mass of catalyst and photo flux, was determined by calculating slope of increase in O_2 accumulation during the first 30 minutes following irradiation, as shown in Figure 2.4. Irradiation time was limited to 30 minutes to minimize the effect of Ag deposition from the sacrificial reagent on both light absorption (shading) and any potential catalytic effect from the Ag such as localized surface plasmon resonance.[22,23] Although irradiation time was limited to 30 minutes, linearity of the O_2 accumulation plots was verified to 4h experiment duration. The OER rate measurements were performed in duplicate to obtain error bars and ensure consistency of the catalytic performance.

Figure 2.5, is a simple diagram of the photocatalytic batch reactor used for the OER experiments. The reactors were 100 mL media bottles capped with PTFE gaskets with ¼-28 threaded ports in a GL 45 lid from Western Analytical Products, allowing for gas-tight reaction conditions. In an effort to improve the detection limit of O_2 and N_2, the gas headspace was decreased by the campus glass blower Stan Heldon who reducing the volume of the jar down to 42 mL. To minimize light loss and maintain a consistent light source position, a plastic cover was 3D printed and then lined on the inside with reflective tape not shown in Figure 2.5. Valves at He and vacuum lines were only opened during purging and were closed during experimentation.

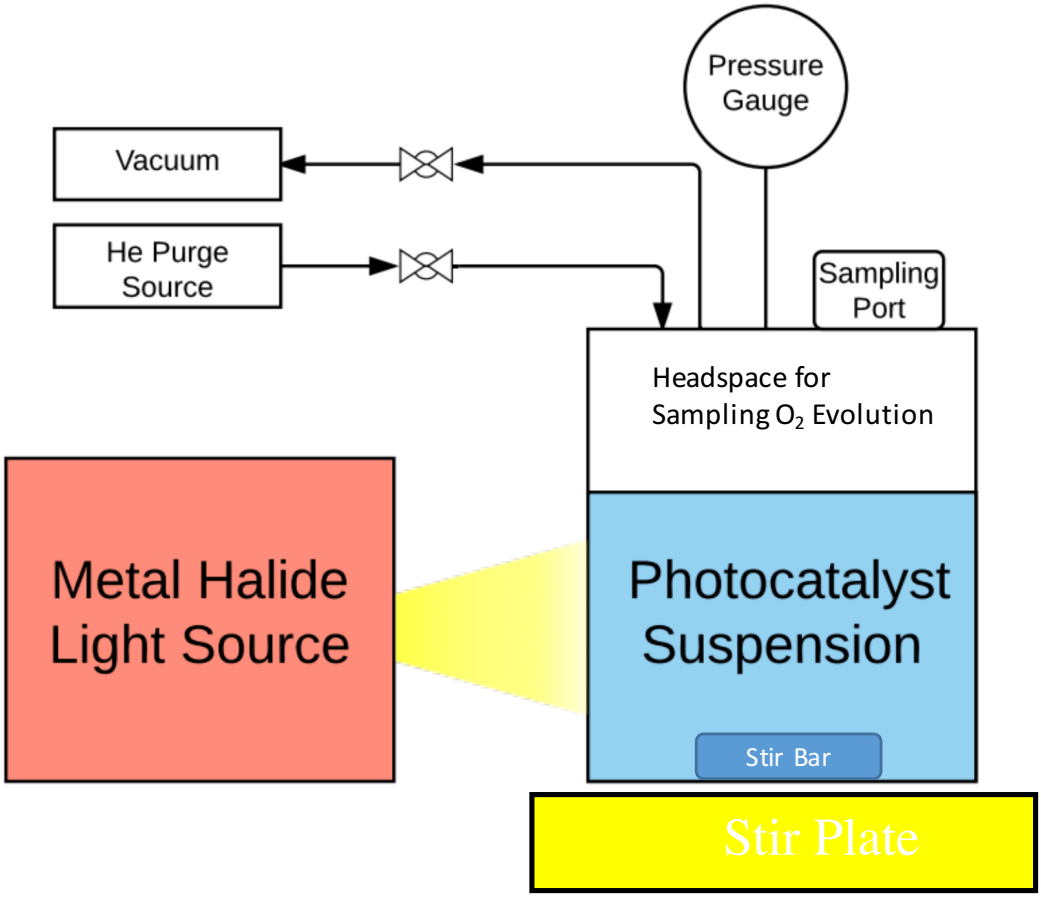

Figure 2.5 Photocatalysis Liquid Batch Phase Reactor Diagram.

2.5 References

1 W. Sun, M. Xie, L. Jing, Y. Luan and H. Fu, *J. Solid State Chem.*, 2011, **184**, 3050–3054.

2 J. Sirita, S. Phanichphant and F. C. Meunier, *Anal. Chem.*, 2007, **79**, 3912–8.

3 F. Zaera, *Chem. Soc. Rev.*, 2014, **43**, 7624–7663.

4 T. Armaroli, T. Bécue and S. Gautier, *Oil Gas Sci. Technol.*, 2004, **59**, 215–237.

5 I. M. Hamadeh, D. King and P. R. Griffiths, *J. Catal.*, 1984, **88**, 264–272.

6 A. C. Yang and C. W. Garland, *J. Phys. Chem.*, 1957, **61**, 1504–1512.

7 D. J. C. Yates, L. L. Murrell and E. B. Prestridge, *J. Catal.*, 1979, **57**, 41–63.

8 J. T. Yates, T. M. Duncan and R. W. Vaughan, *J. Chem. Phys.*, 1979, **71**, 3908–3915.

9 J. T. Yates Jr., T. M. Duncan, S. D. Worley and R. W. Vaughan, *J. Chem. Phys.*, 1979, **70**, 1219.

10 T. M. Duncan, J. T. Yates Jr. and R. W. Vaughan, *J. Chem. Phys.*, 1980, **73**, 975.

11 J. T. Cavanagh, R. R., Yates Jr., *J. Chem. Phys.*, 1981, **74**, 4150.

12 F. Solymosi and M. Pdsztor, *J. Phys. Chem.*, 1985, 4789–4793.

13 J. H. A. Martens, R. Prins, H. Zandbergen and D. C. Koningsberger, *J. Phys. Chem.*, 1988, **92**, 1903–1916.

14 R. Ouyang, J.-X. Liu and W.-X. Li, *J. Am. Chem. Soc.*, 2013, **135**, 1760–71.

15 B. R. Goldsmith, E. D. Sanderson, R. Ouyang and W.-X. Li, *J. Phys. Chem. C*, 2014, **118**, 9588–9597.

16 F. Tao, S. Dag, L.-W. Wang, Z. Liu, D. R. Butcher, H. Bluhm, M. Salmeron and G. A. Somorjai, *Science*, 2010, **327**, 850–853.

17 J. M. Thomas, O. Terasaki, P. L. Gai, W. Zhou and J. Gonzalez-Calbet, *Acc. Chem. Res.*, 2001, **34**, 583–594.

18 D. S. Su, B. Zhang and R. Schlögl, *Chem. Rev.*, 2015, **115**, 2818–2882.

19 J. C. Matsubu, V. N. Yang and P. Christopher, *J. Am. Chem. Soc.*, 2015, **137**, 3076–3084.

20 M. Newville, *Fundamentals of XAFS*, 2004.

21 P. J. Chupas, K. W. Chapman, C. Kurtz, J. C. Hanson, P. L. Lee and C. P. Grey, *J. Appl. Crystallogr.*, 2008, **41**, 822–824.

22 S. Linic, P. Christopher and D. B. Ingram, *Nat. Mater.*, 2011, **10**, 911–921.

23 P. Christopher, D. B. Ingram and S. Linic, *J. Phys. Chem. C*, 2010, **114**, 9173–9177.

Chapter 3 Isolated Metal Active Site Concentration and Stability Controls Catalytic CO_2 Reduction Selectivity

3.1 Summary

In this chapter, the role of isolated Rh atoms in the CO_2 reduction reaction pathways are discussed. First, a quantitative DRIFTS method is developed to quantify the fraction of exposed Rh atoms available for driving reactions in the isolated site geometry compared to the Rh atoms on the surface of Rh NP's. These site fractions are then compared to reactivity data to determine site-specific reactivity, where isolated Rh atoms are determined to drive CO production and Rh NP sites are found to drive CO_2 methanation. These assignments are further tested and supported via selectively removing Rh NP sites and observing the corresponding loss in CH_4 production. Instability is observed at CO_2:H_2 reactant ratios > 1, where CH_4 production is observed to decrease with time-on-stream, however a near proportionate increase in CO production is observed, suggesting the CH_4-producing Rh NP's are converting into CO-producing isolated Rh sites.

Here we utilize probe molecule diffuse reflectance infrared Fourier transform spectroscopy (DRIFTS) with known site-specific extinction coefficients to quantify the fraction of Rh sites residing as atomically dispersed isolated sites (Rh_{iso}), as well as Rh sites on the surface of Rh nanoparticles (Rh_{NP}) for a series of TiO_2 supported Rh catalysts. Strong correlations were observed between the catalytic reverse water gas shift turn over frequency (TOF) and the fraction of Rh_{iso} sites and between catalytic methanation TOF and the fraction of Rh_{NP} sites. Furthermore, it was observed that reaction condition induced disintegration of Rh nanoparticles, forming Rh_{iso} active sites, controls the changing reactivity with time on stream. This work demonstrates that isolated atoms and nanoparticles of the same metal on the same support can exhibit uniquely different catalytic

selectivity in competing parallel reaction pathways and that disintegration of nanoparticles under reaction conditions can play a significant role in controlling stability.

3.2 Introduction:

Approaches for designing optimal heterogeneous catalysts rely on structure-function relationships between active site characteristics and performance. Variations in metal surface structure on model single crystal catalysts, or in size and shape controlled metal nanoparticles, have often been exploited to experimentally correlate active site geometries to catalytic reactivity.[1–6] However, it has been identified that isolated metal atoms on oxide supports can play an unexpected role in governing the reactivity of heterogeneous metal catalysts, and that metallic nanostructures can undergo significant geometric changes under reaction conditions.[7–12] These findings raise questions to the validity of surface structure based active site identification strategies.

Inconsistencies in catalytic structure-function relations have recently been highlighted in efforts dedicated to designing catalysts for the selective reduction of CO_2 by H_2 to produce higher valued products. Studies examining reactivity and selectivity trends for CO_2 reduction by H_2 over heterogeneous transition metal catalysts have hypothesized that particle size is a dominant characteristic controlling catalyst performance and stability under reaction conditions.[5,13–17] However, transmission electron microscopy (TEM) based studies have qualitatively suggested that isolated transition metal sites may also contribute to metal weight loading dependent selectivity and stability trends.[18,19] Direct evidence relating hypothesized particle size and isolated site dependent phenomena in CO_2 reduction catalysis to the nature of active sites controlling catalytic functionality are lacking.

Herein we show quantitative evidence that isolated Rh sites on TiO_2 supports are responsible for controlling catalytic selectivity and stability in CO_2 reduction by H_2. Using probe molecule infrared spectroscopy, the fraction of catalytically active Rh sites existing as atomically dispersed isolated sites (Rh_{iso}) and as Rh sites on the surface of Rh nanoparticles (Rh_{NP}) was quantified for a series of catalysts. Strong correlations were observed between the catalytic reverse water gas shift (r-WGS, $CO_2 + H_2 \leftrightarrow CO + H_2O$) turn over frequency (TOF) and the fraction of Rh_{iso} sites and between catalytic methanation ($CO_2 + 4H_2 \leftrightarrow CH_4 + 2H_2O$) TOF and the fraction of Rh_{NP} sites. Further it was found that Rh nanoparticle disintegration under reaction conditions to form Rh_{iso} sites controls the instability of catalytic selectivity. Our work highlights stark differences in selectivity exhibited by atomically dispersed and nanoparticle based active catalytic sites in parallel reaction pathways and that inter-conversion between these site types is a dynamic process under reaction conditions, providing important information for the design of selective CO_2 reduction catalysts.

3.3 Experimental Methods

3.3.1 Materials

Catalyst precursor rhodium nitrate hydrate ($Rh(NO_3)_3 \cdot xH_2O$) (~36% Rh) was purchased from Sigma-Aldrich. TiO_2 nanoparticle support (P25) was obtained from Evonik. 35% Hydrogen Peroxide (H_2O_2) and 37% Hydrochloric Acid (HCl) were both obtained from Fisher Scientific. All gases used in synthesis, characterizations, and reactions were purchased from Airgas, with the purities and concentrations mentioned in their respective sections.

3.3.2 Material Synthesis

Five weight loadings of Rh (0.5, 2, 3, 4 and 6%) were deposited on TiO_2 nanoparticles (Evonik P25), to produce total sample masses of 300 mg each, using a simple impregnation technique. The quantity of ($Rh(NO_3)_3xH_2O$) necessary for each weight loading was dissolved in an evaporation dish with 600 μL of water. TiO_2 was mixed with the aqueous Rh solution using a stir rod until homogeneous in appearance, dried at 95 °C for 4 hours, ground up with a mortar and pestle, and calcined in a tube furnace at 450 °C in air for 4 hours. *In situ* reduction of the catalysts in pure H_2 (99.999%) at 350 °C for 1 hour was performed to obtain the desired metallic Rh oxidation state prior to CO chemisorption-based analyses (volumetric and diffuse reflectance infrared Fourier transform spectroscopy (DRIFTS)), reactivity experiments in the packed bed reactors and the leaching treatment. A leaching procedure was developed to selectively dissolve Rh nanoparticles off the TiO_2 surface without removing isolated Rh atoms from the TiO_2 surface.[20] The leaching process was executed by suspending 100 mg of reduced catalyst in 10 mL of 11.6 M HCl/1% H_2O_2 solution while constantly stirring for 3 hours at 65 °C. The sample was then washed 4 times in distilled water, separated using centrifugation, dried at 95 °C for 4 hours, and reduced *in situ* prior to catalytic testing or DRIFTS analysis.

3.3.3 Transmission Electron Microscopy

Reduced samples were characterized using a Philips CM300 Transmission Electron Microscope (TEM) operated at 300kV accelerating voltage. After reduction, sample powders were suspended in distilled water using ultra-sonication and added drop-wise onto a holey carbon coated copper grid sample holder. Rh particle size distributions were

determined by measuring the diameter of at least 100 particles for each sample via ImageJ software.

3.3.4 Volumetric CO Chemisorption

Volumetric CO chemisorption analyses were performed with a Micromeritics ASAP 2020. Catalysts were packed in a quartz tube sample holder and heated in H_2 at a heating rate of 10 °C/min to 350 °C with a reduction time at 350 °C of 1 hour. The sample was evacuated at 350 °C for 10 minutes and cooled to 35 °C under vacuum prior to CO chemisorption analysis. Two CO adsorption isotherms were performed (at 35 °C and from 100-450 mmHg) with an evacuation step between the two to remove physisorbed CO. The first isotherm represented both irreversible-chemisorption and reversible-physisorption, where the second isotherm only involved the reversible-physisorption. The difference between the two isotherms represented the total amount of CO chemisorbed to surface Rh atoms. An assumed ratio of 1 CO molecule per surface Rh atom was used to convert the number of chemisorbed CO molecules into the number of surface Rh atoms. This value was corrected, as described below, to account for CO adsorption geometries with non 1:1 CO:Rh ratios.

3.3.5 DRIFTS CO chemisorption

Catalyst samples were packed into a Harrick Praying Mantis™ high temperature reaction chamber (ZnSe windows) mounted inside of a Thermo Scientific Praying Mantis™ diffuse reflectance adapter, set inside of a Thermo Scientific Nicolet™ iS™10 FT-IR spectrometer. Gases were flowed to the reaction chamber using Teledyne mass flow controllers. This setup was used to quantitatively determine the fraction of Rh_{iso} and Rh_{NP}

sites on each catalyst. In all measurements, spectra were obtained by averaging 40 sequentially collected scans at a resolution of 4 cm^{-1}. The spectra were obtained in Kubelka-Munk (KM) units, which have been shown to scale linearly with adsorbate concentration.[21] This analysis was used in 3 different applications: quantifying the Rh_{iso} and Rh_{NP} site fractions of freshly prepared reduced catalysts, quantifying the impact of reaction conditions on the relative quantity of site type fractions, and verifying that the CO chemisorption analyses did not significantly alter the site fractions or structure of the samples during the process of characterization.

3.3.6 Site fraction quantification

Approximately 30 mg of pure TiO_2 (Evonik P25) was packed in the reaction chamber (to minimize use of the Rh/TiO_2 samples) and approximately 10 mg of each Rh/TiO_2 sample was then packed on top. For the 4% and 6% Rh weight loading samples, a 1:1 dilution of the top 10 mg of Rh loaded samples with plain TiO_2 was used to improve the signal by reducing absorption. The samples were purged with pure H_2 (99.999%) at 100 sccm for 15 minutes at room temperature and then reduced in pure H_2 at 20 sccm and 350 °C for 1 hour. The reactor was then cooled to room temperature and purged with Ar (99.999%) at 100 sccm for 10 minutes and then a baseline spectrum was taken of the sample. 50 sccm of a 10%CO/90%Ar stream was then introduced to the sample for 10 minutes to allow for complete CO adsorption. The sample was then purged with 100 sccm Ar for 10 minutes and a DRIFT spectrum was acquired to quantitatively determine the fraction of both Rh_{iso} and Rh_{NP} sites. To verify that 10 minutes of CO adsorption was enough time to reach monolayer saturation and examine the stability of the catalysts during the site fraction

quantification, the site fractions were also monitored on a per minute basis during the CO exposure and Ar purge steps. The peak intensities, I_i, were determined from de-convolution using Omnic software and were converted into site fractions using previously determined extinction coefficients[22] for each vibrational mode and the following equation:

$$X_{iso} = \frac{I_{iso}/\left(\epsilon_{iso} \times \left(\frac{CO}{Rh}\right)_{iso}\right)}{\sum_{i=1}^{3}\left[I_i/\left(\epsilon_i \times \left(\frac{CO}{Rh}\right)_i\right)\right]} \quad 3.1$$

The three types of CO configurations considered were gem-dicarbonyl (Rh_{iso}), linear (Rh_{NP}), and bridge bound (Rh_{NP}), where the Rh_{iso} sites were quantified based on the intensity of the symmetric gem-dicarbonyl CO stretch. Rh_{NP} site fraction (X_{NP}) was calculated as X_{NP} = 1- X_{iso}. The extinction coefficients, ε_i, used for the symmetric gem-dicarbonyl, linear, and bridge configurations were 74, 26, and 85 (cm/mole)(10^8) respectively.[22] The extinction coefficients were used from an earlier study on Rh/Al_2O_3, where the nature of the support may slightly affect the extinction coefficient, particularly the gem-dicarbonyl species. Although, the similarity of vibrational frequencies of the gem dicarbonyl species on the two supports suggests that this difference wouldn't impact our results. The CO:Rh ratios for the symmetric gem-dicarbonyl, linear, and bridge configurations were 2, 1, and 0.5 respectively.

3.3.7 Volumetric CO Chemisorption Mimic Experiment

To examine catalyst stability during the volumetric CO chemisorption measurements (Section 2.3.2), we designed a DRIFTS-based experiment to mimic the volumetric measurements while simultaneously quantifying Rh_{iso} and Rh_{NP} site fractions. The

experiment utilized the same procedure described above to determine the initial site fractions and utilized flowing 10%CO/Ar and Ar (99.999%) over the sample to mimic the CO adsorption isotherm and evacuation steps, respectively. After the initial site fractions were measured, the 6% Rh/TiO_2 sample was heated from 25 °C to 35 °C and exposed to 10%CO/Ar flow for 3 hours, followed by pure Ar flow for 1 hour and finally 3 hours with flowing 10%CO/Ar while simultaneously collecting DRIFT spectra every 10 minutes. Spectra processing and site quantification was executed identically to the approach described above.

3.3.8 Reaction conditions induced catalyst restructuring

To study the effect of reaction conditions on the Rh_{NP} and Rh_{iso} site fractions, the same procedure as mentioned above was performed to obtain initial site fractions, followed by 90 minutes under reaction conditions and then post reaction CO adsorption analysis. All of these steps were performed sequentially, *in situ*, in the Harrick reaction chamber. After the initial CO adsorption spectrum was acquired, the reactor was purged and heated to a reaction temperature of 200 °C under 100 sccm Ar flow. All 5 Rh weight loadings were tested at the $10CO_2$:H_2 ratio to mimic the reaction conditions explored in the catalytic testing experiments. After 90 minutes at reaction conditions, the samples were purged with Ar and cooled back to 25 °C where a new background was obtained. CO adsorption, followed by Ar purging and DRIFT spectra collection was then executed on the post-reaction samples. The CO DRIFT spectra were processed in the same manner described above to determine how and to what degree the site fractions changed as a function of Rh weight loading due to reaction conditions.

3.3.9 Reactor Experiments

Catalysts were reduced *in situ* at 350 °C for 1 hour in pure H_2 prior to catalytic testing. All CO_2 reduction reaction rates were measured using 15-30 mg of catalyst at 200 °C in a ¼" OD borosilicate packed bed reactor operating at atmospheric pressure and running under differential reactor conditions (conversion of limiting reagent < 10%) with the effluent quantified by online gas chromatography (SRI MG #3). CO_2 was separated from other gases using a molecular sieve (MS13X) packed column, while H_2, N_2, CH_4, and CO were separated using a Hayesep D column. The separated gases were then quantified using a Helium Ionization Detector (HID) and a Thermal Conductivity Detector (TCD). The total reactant flow rate in all studies was 100 standard cm^3 per minute (sccm). Gases were delivered via Teledyne mass flow controllers. The CO_2:H_2 ratio was varied from stoichiometric methanation conditions, 1:4, to H_2-lean conditions, 10:1, by varying individual flow rates. Inert N_2 carrier gas was used at all conditions with a flow rate of greater than 89 sccm. It is important to note that for each reaction condition a fresh sample was loaded into the reactor to ensure each experiment was measuring the reactivity of freshly prepared samples. Reaction rates and selectivity were calculated based on the average of five measurements taken during the first hour on stream. See Table 3.1 for experimental details regarding reactant flow rates for each condition.

Table 3.1 Reactant flow rates in packed bed reactor experiments

Gas	CO_2:4H_2	3CO_2:H_2	10CO_2:H_2
CO_2 (sccm)	1	3	10
H_2 (sccm)	4	1	1
N_2 (sccm)	95	96	89

3.3.10 TOF Calculations

In this work, we will report overall TOFs on the basis of reaction rates per total number of sites (Rh_{iso} + Rh_{NP}) and site-specific TOFs which refer to the TOFs for a specific reaction on the basis of specific site type concentration (Rh_{iso} or Rh_{NP}). Below we will describe our approach to calculating overall TOF's and the site-specific TOF calculation is discussed in the results section. Hereafter, site-specific TOFs will be denoted as so and all other mentions of TOF will be on an overall sites basis. CO can adsorb to Rh sites in three main configurations, the gem-dicarbonyl, linear, and bridge configurations, which exhibit CO to Rh ratios (CO:Rh) of 2:1, 1:1 and 1:2, respectively. Different fractions of each site type exist for each Rh weight loading, and thus the overall CO:Rh ratios will be different for each weight loading when a saturated CO monolayer is added. Therefore, the ratio of 1:1 for CO:Rh assumed in the volumetric CO chemisorption analysis must be corrected to account for the varying CO:Rh ratio and allow for accurate TOF calculations in the units molecules/Rh atom/second for each catalyst. The correct ratio of CO:Rh was determined from the DRIFTS analysis described above by determining the fraction of each CO adsorption site type for each Rh weight loading. Finally, the number of Rh sites per weight of catalyst measured by volumetric CO chemisorption was divided by the CO:Rh ratio

measured in the DRIFTS experiments to provide an accurate Rh site concentration for each catalyst weight loading, which was used in the TOF calculations.

3.4 Results

3.4.1 Site Specific Reactivity

The 5 weight loadings of Rh on TiO_2 were characterized by TEM and DRIFTS CO chemisorption to determine Rh nanoparticle sizes and the fraction of Rh sites existing as Rh_{NP} and Rh_{iso}. Representative micrographs of each Rh weight loading and the measured average particle sizes are shown in Figure 3.1. Only small variations in average particle sizes were observed, ranging from 1-1.5 nm for Rh weight loadings 0.5-4% (all within measurement error) and increasing to 2.5 nm for the 6% Rh weight loading. It is important to note that we made no attempt to quantify isolated site concentration from TEM, due to the difficulty of detecting the species and the very small sample size we would obtain in such a measurement, and thus the reported particle size represents the average size of metallic particles with diameter greater than ~0.3 nm. Regardless of the quantitative

shortcomings of electron microscopy, the micrograph in figure 3.2 verifies that isolated Rh sites were indeed present in our samples. Figure 3.3(a) shows a typical DRIFT spectrum acquired following CO adsorption at 300K on a fresh, reduced 4% Rh/TiO_2 catalyst. The

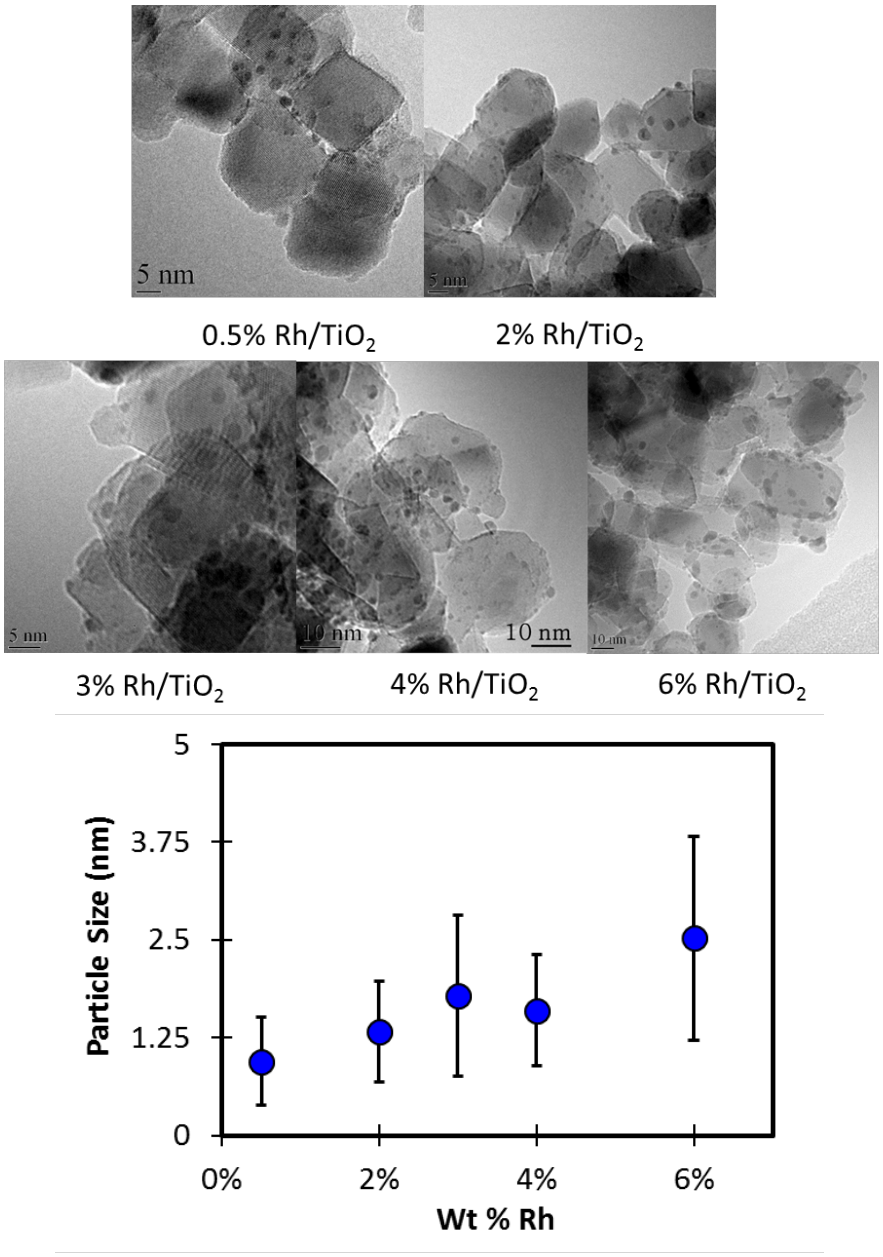

Figure 3.1 The top panel shows representative micrographs of the 5 samples used in this study. The bottom panel shows the measured Rh particle diameter as a function of Wt % Rh. Error bars represent standard deviation from at least 100 particles measured.

peaks at ~2097 and ~2028 cm^{-1} are associated with the symmetric and asymmetric stretches of the $Rh(CO)_2$ gem-dicarbonyl species that exist uniquely at Rh_{iso} sites on the TiO_2 support.[23,24] The assignment of these peaks to an isolated Rh atom on a support with two CO molecules bound to it has been thoroughly substantiated in previous studies.[22–25] The peaks at 2068 and 1860 cm^{-1} are associated with CO adsorbed in linear and bridge bound geometries at Rh_{NP} sites.[23,24] Schematic depictions of these adsorption geometries are shown in Figure 3.3(a). The DRIFT spectra obtained for CO on all 5 Rh weight loadings are shown in Figure 3.3(b) and normalized by the symmetric gem-dicarbonyl peak height. Variations in the linear CO peak height with Rh weight % correlate to increasing fractions of Rh_{iso} sites. A similar trend was not observed for the bridge bound CO geometry.

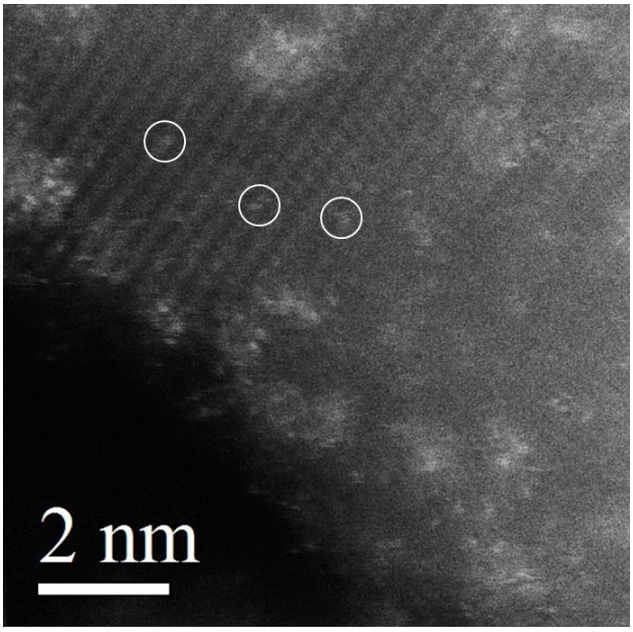

Figure 3.2 STEM analysis of 2% Rh/TiO2. Isolated Rh atoms are denoted by white circles.

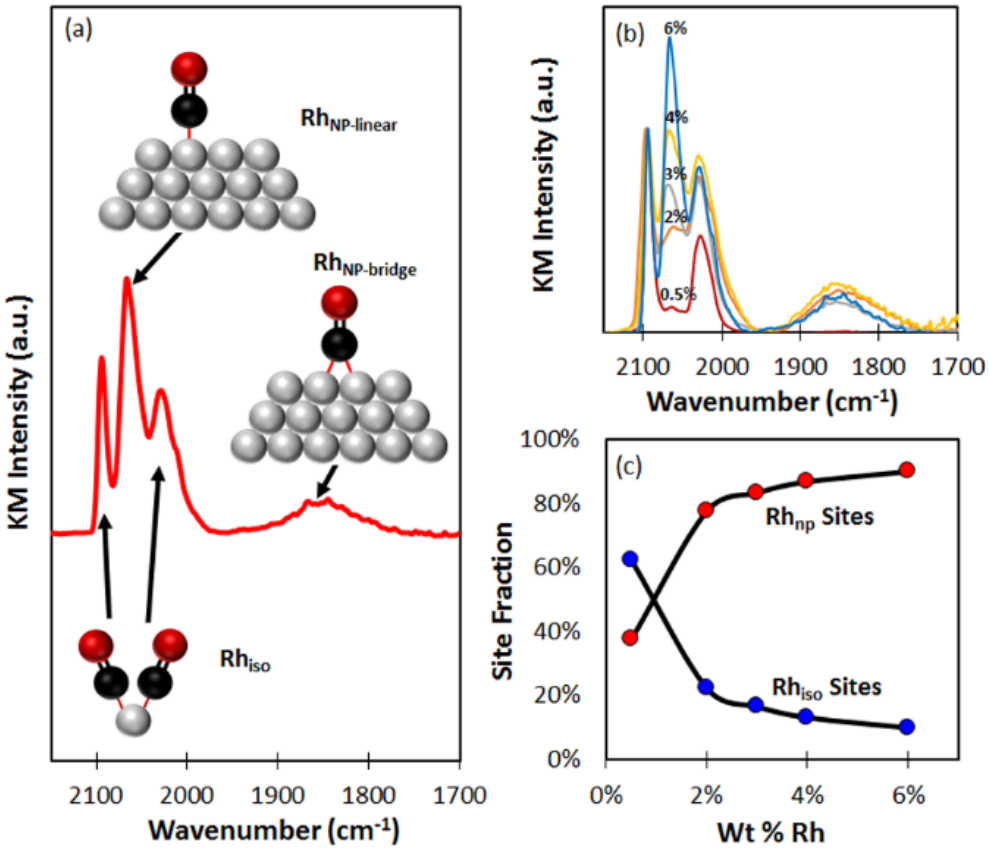

Figure 3.3 a) DRIFT spectrum obtained from a saturated layer of CO adsorbed at 300K on 4%Rh/TiO_2. Insets show ball-and-stick models of assigned vibrational modes. b) DRIFT spectra of CO on all 5 weight loadings of Rh/TiO_2 catalysts. The spectra are displayed in Kubelka-Munk (KM) units and normalized by the symmetric gem-dicarbonyl peak (2097 cm^{-1}) height to allow for comparison. c) Site fraction (%) of isolated (Rh_{iso}) and nanoparticle based Rh sites (Rh_{NP}), calculated based on equation 1 and the spectra in b), as a function of Wt % Rh.

This inconsistency was due to the broader and weaker nature of this peak along with it residing between the asymmetric gem-dicarbonyl and adsorbed water peaks at lower wavenumber (not shown here), which made this species consistently difficult to baseline and quantify. The absolute intensity of the bridge peak had a minimal impact on the quantified Rh_{NP} and Rh_{iso} site fractions, due to its low magnitude and high extinction coefficient. The fractions of each site type (Rh_{iso} and Rh_{NP}) were quantified for the five catalyst weight loadings, using equation 1 and the spectra in Figure 3.3(b), and are shown

in Figure 3.3(c)[22]. At the smallest Rh weight loading (0.5%) a relatively high fraction of Rh_{iso} sites exists on the TiO_2 support (~62%), Figure 3.3(c). The fraction of Rh_{iso} sites drops significantly (<20%) as the Rh weight loading was increased to 2%. Our results are consistent with prior literature,[25] demonstrating that the CO:Rh ratio in a saturated CO monolayer decreased with increasing Rh weight % loading. We observed that the CO:Rh ratios at saturation coverage were 1.62, 1.13, 1.12, 1.04 and 1.06 for the 0.5, 2, 3, 4, and 6 % Rh catalysts, respectively. Alternative to site fraction, Figure 3.4 shows the concentration (number of sites per gram catalyst) of Rh_{iso} and Rh_{NP} site types as a function of Rh weight % loading. The concentration of Rh_{NP} sites increased ~5-fold as Rh weight% increased from 0.5% to 2% and remained constant from 2% to 6%, whereas the concentration of Rh_{iso} sites gradually decreased as Rh weight% increased from 0.5% to 6%.

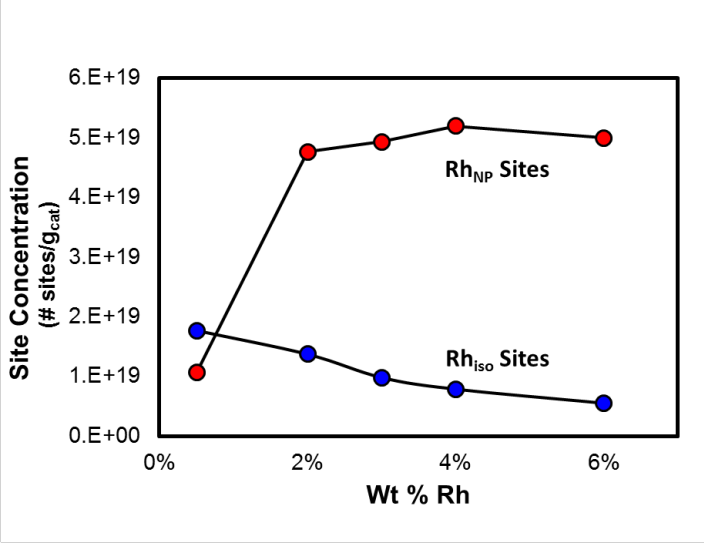

Figure 3.4 Site concentration as a function of Wt % Rh for both Rh_{NP} and Rh_{iso} site types. Site concentrations were calculated by using DRIFTS corrected volumetric chemisorption to determine total number surface Rh sites per gram of catalyst and then multiplied by the fraction of site type values shown in Figure 3.3(c).

It is well known that CO can induce restructuring of supported Rh nanostructures, even at ambient conditions[26] similar to the those used in our DRIFTS and volumetric CO chemisorption analyses of site fractions and total site concentration.[25] We performed experiments to monitor site fractions over time during the course of these analyses to ensure that the measurements themselves were not inducing changes in catalyst structure or site fraction. As shown in Figure 3.5(a), the site fractions were relatively constant during the course of the DRIFTS CO chemisorption studies, exhibiting only a small change toward the end of the 10 min Ar purge after CO adsorption. The reasonable stability during the first 15 minutes of the experimental protocol used in these measurements justifies that the site fractions in Figure 3.3(c) are good representations of the freshly synthesized and

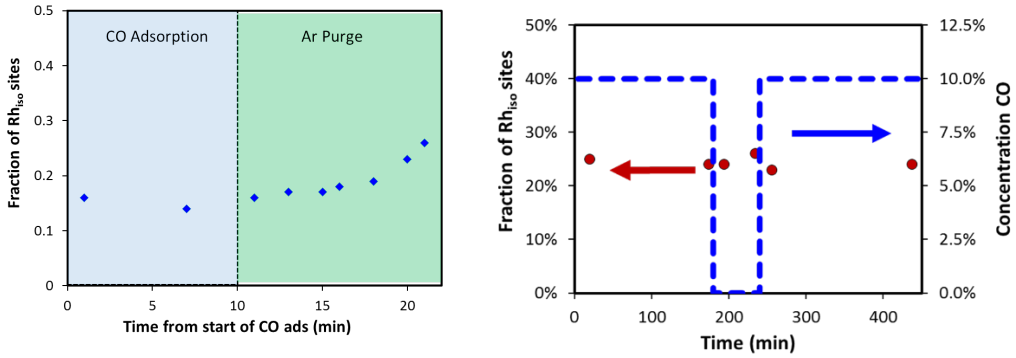

Figure 3.5 a) Measured Rh_{iso} site fraction of 3%Rh/TiO_2 as a function of time during the course of a CO adsorption experiment. CO was introduced into the system at t = 0 min and the Ar purge started at t = 10 min. The Rh_{iso} site fraction was seen to be relatively stable for the course of this experiment. b) Rh_{iso} site fraction as a function of time on a 6%Rh/TiO_2 sample during an experiment meant to mimic the volumetric CO chemisorption measurements. At t = 0, 10% CO/Ar was introduced to the system at a flow rate of 100 standard cubic centimeters per minute (sccm). At t = 180 min pure Ar was introduced to the system at 100 sccm. At t = 240 min 10%CO/Ar was once again introduced to the system at 100 sccm. Clearly the Rh_{iso} site fraction was constant during the course of this measurement. The dots correspond to the fraction of Rh_{iso} sites on the left axis and the dotted line correspond to the concentration of CO on the right axis. It is important to note the difference in site fraction between this plot and the 6%Rh/TiO_2 sample used in Figure 3.3(c) can be attributed to them being different batches of catalyst. Upon repeated analysis of any given batch, the site fractions were consistent for the sample characterized in Figure 3.3. All other figures in the paper and supplemental information besides this one used consistent batches.

reduced catalysts. Another experiment was performed to verify the experimental procedure for volumetric CO chemisorption measurements did not impact the site fractions. We mimicked the volumetric measurements *in situ* in the DRIFTS reaction cell and observed constant site fractions during the course of the experiment, Figure 3.5(b). These two experiments justify that the site fraction and Rh:CO values derived from the DRIFTS and volumetric CO chemisorption measurements (that are used for TOF calculations) are an excellent representation of the fresh synthesized and reduced catalysts. To summarize the catalyst characterization, it was seen while the relative site fractions of Rh_{iso} and Rh_{NP} vary most significantly for the smaller weight loading catalysts (0.5-3% Rh), the particle size was constant for all weight loadings except the highest (6% Rh).

Catalytic selectivity toward CH_4 production (r-WGS, CO production, is the competing reaction) was measured for the 5 Rh weight loadings on TiO_2 under varying CO_2:H_2 ratios, Figure 3.6. Under stoichiometric methanation conditions (CO_2:$4H_2$), 0.5%

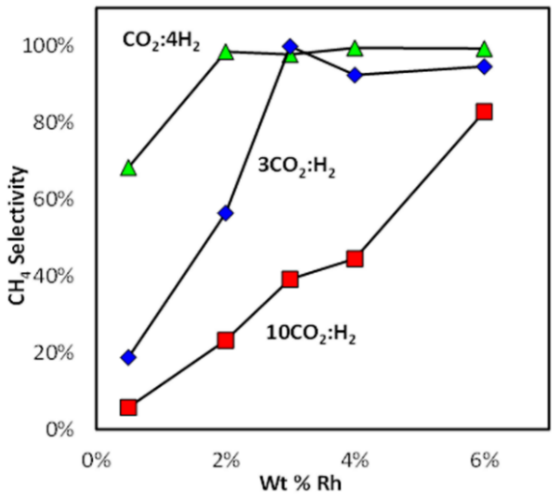

Figure 3.6 CH_4 selectivity as a function of Wt % Rh for 0.25, 3, and 10CO_2:H_2 feed ratios measured at 200 °C.

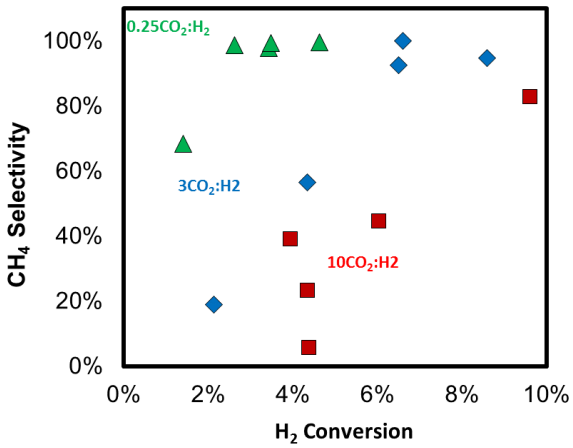

Figure 3.7 Methane Selectivity vs H_2 Conversion. The high methane selectivity across the range of H_2 conversions indicates that conversion was not the primary driver for the methane selectivity trends observed in Figure 2, as would be expected at these low conversions.

Rh/TiO_2 exhibited a CH_4 selectivity of 65%, whereas all other weight loadings exhibited >98% CH_4 selectivity. As the CO_2:H_2 ratio was increased to more CO_2 rich conditions, the CH_4 selectivity decreased at all weight loadings, which is consistent with the positive CO_2 reaction order for r-WGS and zero reaction order for methanation over Rh catalysts.[27] For all CO_2:H_2 feed ratios tested, a positive dependence of CH_4 selectivity on Rh weight loading was observed. It's important to note that the effect of H_2 conversion on selectivity was considered in Figure 3.7, and the high selectivity across the whole range of conversions suggests conversion is not the primary driver for the trends observed, as expected based on the low conversions. By examining the CO and CH_4 production TOFs separately, as a function of Rh weight loading as shown in Figure 3.8 and Figure 3.9, respectively, we can explore the origin of the CO_2 reduction selectivity dependence on Rh weight loading. Figure 3.8(a)-(c) show an agreement between the trend of CO production TOF and fraction

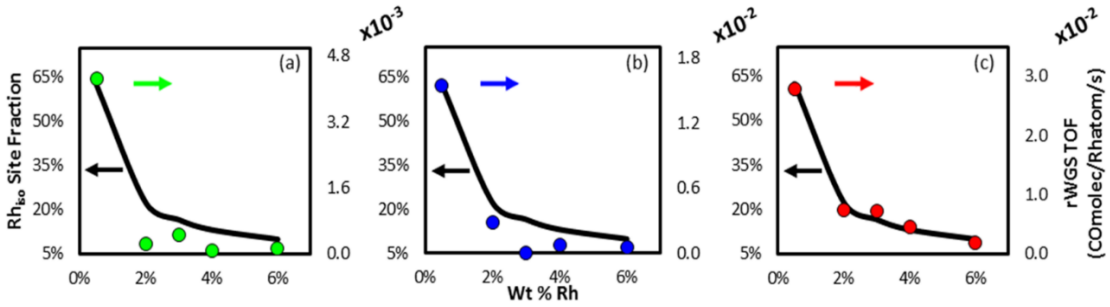

Figure 3.8 Rh_{iso} site fraction and r-WGS TOF plotted as a function of Wt % Rh at a) $1CO_2$:$4H_2$ b) $3CO_2$:H_2, c) 10 CO_2:H_2 feed ratios. The left axes are Rh_{iso} site fractions, which are displayed in the plots as a black line connecting the measured values for graphical clarity. The green, blue, and red data points correspond to measured r-WGS TOF and are quantified in the right axis of each plot.

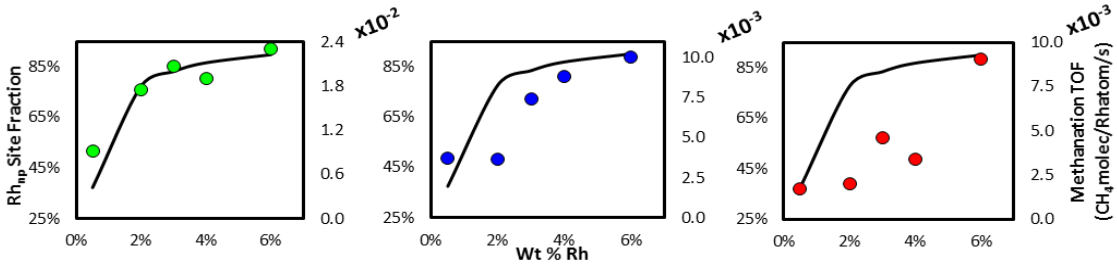

Figure 3.9 a) Rh_{NP} site fraction and methanation TOF plotted as a function of Wt % Rh at a) $1CO_2$:$4H_2$ b) $3CO_2$:H_2, c) 10 CO_2:H_2 feed ratios. The left axes are Rh_{NP} site fractions, which are displayed in the plots as a black lines connecting the measured values for graphical clarity. The green, blue, and red data points correspond to measured methanation TOF and are quantified in the right axis of each plot.

of Rh_{iso} sites as a function of Rh weight loading for the three conditions tested. In this plot the site concentration and reaction rates are both normalized on a per total Rh sites basis, providing site fraction and TOF, respectively, allowing a consistent comparison. Of particular note is that the relative magnitude of change of the CO production TOFs and Rh_{iso} site fractions as a function of Rh weight loading are quantitatively similar. For example, at 3:1 CO_2:H_2 feed ratio, the CO production TOF decreased from $0.57x10^{-3}$ to $0.29x10^{-3}$ CO molecules/Rhatom/second as the weight loading was increased from 0.5% to 2% Rh, where a similar ~3 fold decrease in Rh_{iso} site fraction was observed. A similar

consistency is seen between the Rh weight loading dependent CH_4 production TOF and the fraction of Rh_{NP} sites in Figure 3.9.

The trend between CO production TOF and Rh_{iso} site fraction was evaluated through an alternative comparison by plotting the rate of r-WGS per gram catalyst as a function of number of Rh_{iso} sites per gram catalyst, as shown in Figure 3.10. Linearity in the plot for each CO_2:H_2 feed ratio corresponds to the agreement between Rh_{iso} site fraction and r-WGS TOF shown in Figure 3.8. The slopes of the lines in Figure 3.10 provide site-specific TOF for r-WGS exclusively on Rh_{iso} sites and are an average of the site-specific TOF measured across all tested catalysts at a given condition. For example, the average site-specific r-WGS TOF for 10 and 0.25 CO_2:H_2 ratios were 0.029 and 0.0049 CO molecules/Rh_{iso} site/second, respectively. The same analysis and similar linear trends were observed for the methanation rate and Rh_{NP} sites, which yielded average site-specific methanation TOF for 10 and 0.25 CO_2:H_2 of 0.0059 and 0.024 CH_4 molecules/Rh_{NP} site/second, respectively.

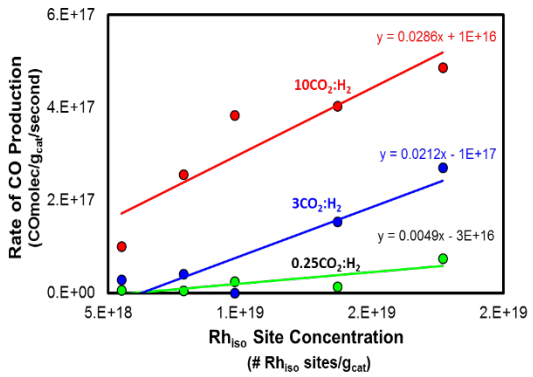

Figure 3.10 Rate of CO production as a function of Rh_{iso} Site Concentration for 0.25, 3, and 10 CO_2:H_2.The linearity in this plot corresponds to the agreement between Rh_{iso} site fraction and rWGS TOF observed in Figure 3.8. The slopes of the lines represent average TOFs for rWGS specifically on the Rh_{iso} sites (CO molecules/Rh_{iso} sites/second).

While we expect the site-specific TOF for r-WGS on Rh_{iso} sites to be relatively constant for all Rh_{iso} sites, the site-specific methanation TOF on Rh_{NP} sites represent the population weighted average of the TOF specific to various site types (terrace, edge, and corner) that exist on metal nanoparticle surfaces. This last point is discussed more thoroughly in the discussion section.

The agreement in the trends between the site fraction and TOF in Figures 3.8 and 3.9 and the linearity displayed in Figure 3.10 suggests that the relative fraction of Rh_{iso} sites controls the TOF for CO production, whereas the relative fraction of Rh_{NP} sites controls the TOF for CH_4 production. Thus, selectivity between the branching pathways of CO_2 reduction into CO and CH_4 is controlled by the ratio of these site types. This selectivity controlling mechanism is further substantiated by incongruence between the relatively constant particle sizes and large variations in TOF values in the Rh weight loading range 0.5-4%, suggesting that particle size effects do not significantly control the observed variations in selectivity.

3.4.2 Impact of Nanoparticle Leaching

Quantitative agreement between variations in the TOF's and site fractions as a function of Rh weight % allowed us to postulate that the Rh_{iso} and Rh_{NP} sites operate as nearly exclusive active sites for driving their respective CO and CH_4 production reaction pathways. Another simple approach to probe the reactivity of a particular site type is to test the selectivity of a material with one exclusive site type. Leaching has been previously used to distinguish the importance of isolated catalytic sites from nanoparticle-based sites, by removing the nanoparticles and observing very little change in the catalytic activity,

suggesting the nanoparticles served more as a spectator than active catalyst site. For example, NaCN based leaching has been used to remove Au clusters and nanoparticles from a support without leaching away the single Au sites to identify the single Au sites as being the active site for driving the WGS reaction.[10,11] In a similar thought process, we treated a 2% Rh/TiO_2 sample with a HCl/H_2O_2 based leaching process to remove Rh_{NP} sites from the support and substantiate the relationship between Rh_{iso}/Rh_{NP} site fraction and CO_2 reduction selectivity.[20] Figure 3.11(a) shows DRIFT spectra for CO chemisorbed to the 2% Rh catalyst before and after leaching. A significant decrease in the relative fraction of Rh_{NP} sites (from 78 to 51%) was observed, as indicated by the significant decrease in the CO-linear and CO-bridge peak intensities (2068 and 1860 cm^{-1}). Although the nanoparticles were not completely removed, the significant change in the site fraction suggests that the leaching procedure selectively removed Rh nanoparticles, leaving behind a majority of Rh_{iso} sites on the support. Because volumetric CO chemisorption experiments were not executed after leaching, the DRIFT spectra only allow us to assert that the relative fraction of Rh_{NP} sites decreased significantly, but we cannot comment on the absolute number of each site type remaining.

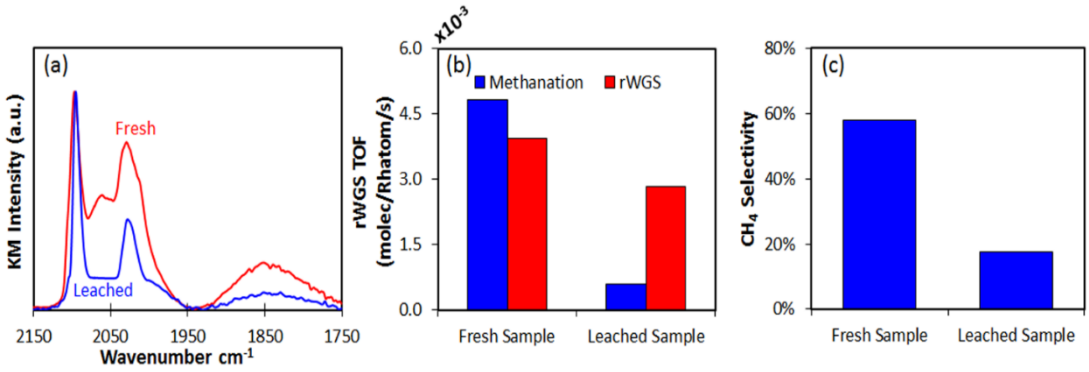

Figure 3.11 a) DRIFT spectra for CO adsorbed on the fresh 2% Rh/TiO_2 and HCl/H_2O_2 leached samples, where spectra are displayed in KM units and normalized by the symmetric gem-dicarbonyl peak (2097 cm^{-1}) height. b) TOF for both CO_2 reduction pathways measured on the fresh 2% Rh/TiO_2 and leached samples at 200 °C and a feed ratio of $3CO_2:H_2$. The quantified number of Rh sites for the fresh catalyst was also used for the TOF calculations in the leached sample, see main text for discussion on this. c) CH_4 selectivity plotted for the fresh and leached samples at 200 °C and a feed ratio of $3CO_2:H_2$.

Catalytic testing of the leached material at $3CO_2:H_2$ conditions and 200ºC showed a significant reduction in the CH_4 production TOF (-88%), with a decrease in r-WGS TOF to a much lesser degree (-28%) compared to the same experiment performed on fresh material, Figure 3.11(b). The reported TOFs for the leached material were calculated using the fresh material's surface area (Rh sites/weight), and as a result the change in TOFs are representative of the absolute changes in the number of each site type due to leaching, suggesting a fairly complete leaching of Rh nanoparticles from the support. The larger decrease in CH_4 production TOF, compared to CO production TOF, as a result of leaching led to a decrease in CH_4 selectivity from 58% to 17%, Figure 3.11(c). The leaching induced decrease in CH_4 selectivity of ~40% is reasonably consistent with the measured decrease in Rh_{NP} site fraction of ~27%, particularly when considering other potential impacts of the leaching procedure including Cl poisoning of nanoparticle sites. The correlated

relationships between Rh_{iso} (Rh_{NP}) site concentration and CO (CH_4) production (analyzed by Rh Wt % dependence and leaching) provides strong evidence that Rh_{iso} sites are highly selective for CO production, whereas Rh_{NP} sites are highly selective for CH_4 production.

3.4.3 Site switching controls instability

At the most H_2 lean conditions, $10CO_2$:H_2, the agreement between weight loading dependent trends for the CO (CH_4) TOF and Rh_{iso} (Rh_{NP}) site fractions were not as good as under more H_2 rich conditions (see Figure 3.9). Examination of time dependent changes in catalytic reactivity provides evidence explaining this behavior and further substantiates the assigned site type-reactivity relationships. The deviation in agreement observed for the $10CO_2$:H_2 feed ratio is due to an observed change in the reactivity of the catalyst under these conditions during the course of the TOF measurement; TOF's were calculated based on the average measured rate in the first hour under reaction conditions. Figure 3.12(a) and (b) show the rates of change of the measured TOF's ($\frac{dTOF}{dt}$) for CO and CH_4 production at CO_2:$4H_2$ and $10CO_2$:H_2 feed conditions, respectively, calculated for the first hour under reaction conditions (see Figure 3.13 for explanation of the rate of change calculation). Figure 3.12(a) shows that all tested catalysts were stable under CO_2:$4H_2$ reaction conditions for the first hour on stream. However, under 10 CO_2:H_2 feed conditions the CO TOF increased with time on stream while the CH_4 TOF decreased with time on stream. There was a quantitative agreement between the rates of TOF change for CO and CH_4 production,

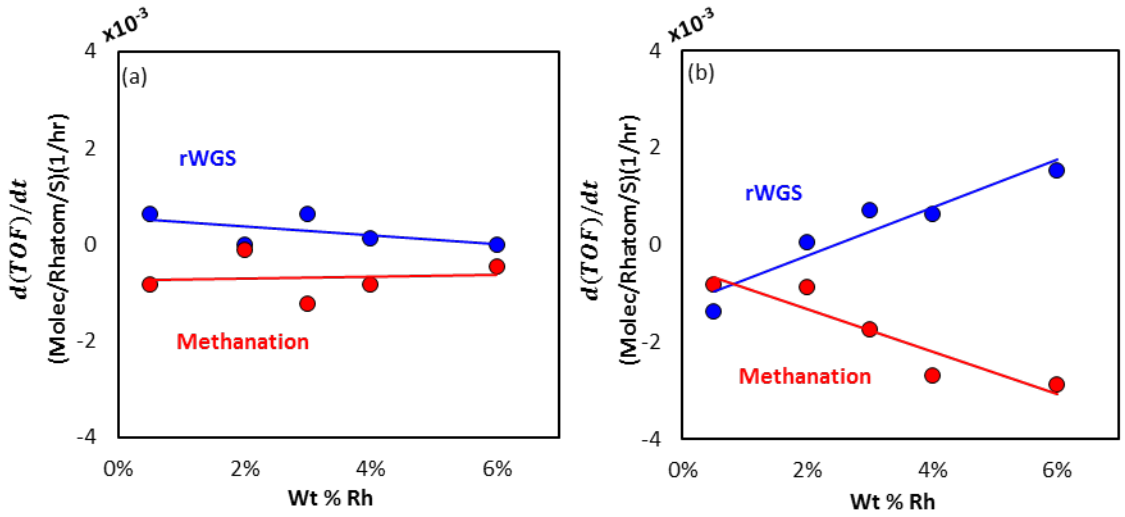

Figure 3.12 Rate of TOF change (d(TOF)/dt) for both reaction pathways as a function of Wt % Rh measured at 200 °C and feed ratio of a) $0.25CO_2$:H_2 and b) $10CO_2$:H_2. Rates of change for the r-WGS TOF are shown in blue points and methanation TOF in red points. The linear fits to the data are added for visual clarity.

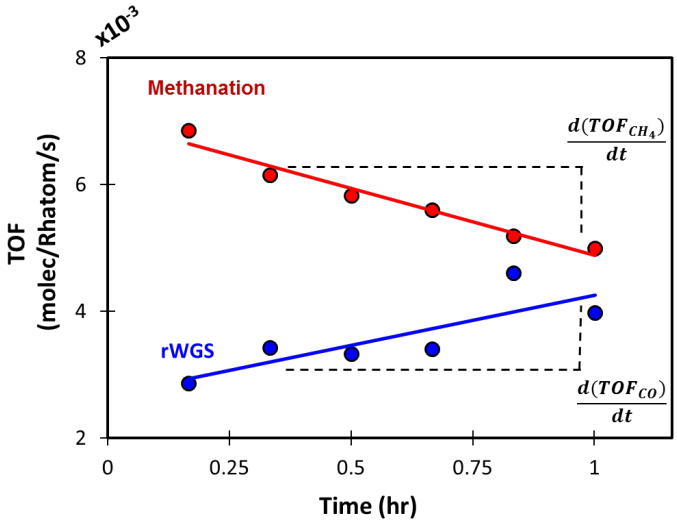

Figure 3.13 TOF for both reaction pathways plotted as a function of time-on-stream for the 6% Rh/TiO_2 catalyst at 200 °C and a feed ratio of $10CO_2$:H_2. Also displayed is how the rate of TOF changes (d(TOF)/dt) shown in Figure 3.12 were calculated.

ity

relationships assigned above, suggest that under H_2 lean reaction conditions Rh nanoparticles disintegrate to form increased concentrations of Rh_{iso} sites and that this process controls the increase in CO TOF and concomitant decrease in CH_4 TOF with time on stream. The changing reactivity during the first hour on stream at the $10CO_2$:H_2 feed conditions also explains why the trends in TOF and site concentration seen in Fig 3.9 aren't in excellent agreement, because the fraction of site types was changing during the TOF measurements.

To quantitatively explore the proposed reaction condition induced Rh nanoparticle disintegration mechanism, CO chemisorption DRIFTS measurements were used to determine the fraction of Rh_{iso} and Rh_{NP} sites before and after 90 minutes on stream under $10CO_2$:H_2 feed ratio and 200 °C; see section 2.3.3 for details. Figure 3.14(a) shows an example of data obtained from these measurements, where DRIFT spectra for CO adsorbed at 300K and saturation coverage before and after 90 minutes on stream are compared for a 6%Rh/TiO_2 sample. The relative strength of the peaks associated with the Rh_{NP} sites slightly decreases due to reaction conditions. Alternatively, the relative strength of the peaks associated with Rh_{iso} sites increased significantly after 90 minutes on stream. This suggests that under reaction conditions, metal atoms from Rh nanoparticles disperse to form isolated Rh atoms on TiO_2. Although the spectra taken after the reaction looks to have had a net increase in total sites, this can be explained by the much larger extinction coefficient corresponding to the Rh_{iso} sites than the Rh_{NP} sites. As previously mentioned, the bridge peak resolution may have limited our ability to observe a change in intensity due to time-on-stream. Once again the CO chemisorption DRIFT spectra are only used to

calculate relative Rh_{NP} and Rh_{iso} site fractions, but not to quantify the absolute number of sites. To calculate a change in relative site fractions due to reaction conditions it was assumed that the loss of Rh_{NP} sites was due exclusively to a gain in Rh_{iso} sites; no Rh vaporization or dissolution into the TiO_2 bulk were considered. These measurements were performed for all 5 Rh weight loadings.

The measured rates of change in CH_4 selectivity and fraction of Rh_{NP} sites are shown in Figure 3.14(b) and (c), respectively, as a function of Rh weight loading. At the lowest Rh weight loading (0.5%) a 4 % decrease in the CH_4 selectivity and 3% reduction in the fraction of Rh_{NP} sites were observed for the first hour on stream. However, the 6% Rh sample showed a 27% decrease in CH_4 selectivity and 26% reduction in fraction of Rh_{NP} sites during the first hour on stream. Figure 3.14(b) and (c) show an excellent correlation between the change in CH_4 selectivity and the conversion of Rh_{NP} sites into Rh_{iso} sites as a function of time on stream for all Rh weight loadings. Furthermore, it was observed that the rate of loss in methane selectivity and Rh_{NP} site fraction increased with increasing Rh

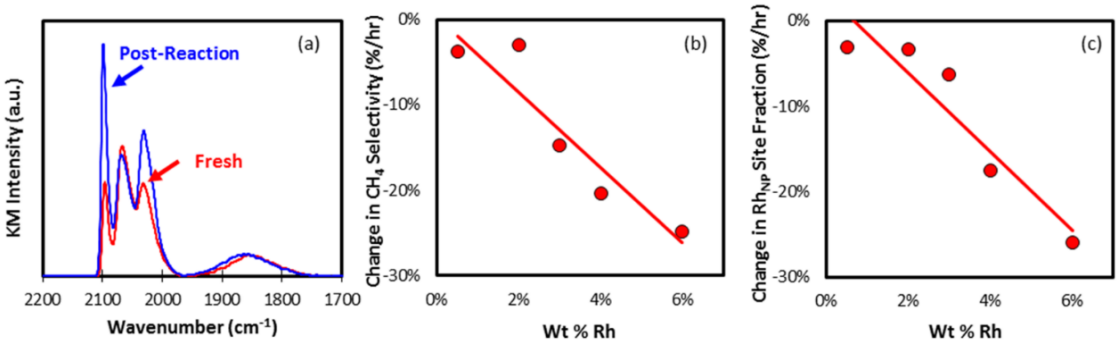

Figure 3.14 a) DRIFT spectra of CO adsorbed at 300K on the fresh 6 Wt % Rh/TiO_2 sample and after 90 minutes under reaction conditions at 200 °C and $10CO_2$:H_2 feed ratio. The spectra are presented in baseline subtracted, raw KM units with no normalization. b) Rate of CH_4 selectivity change (%/hr) measured at identical conditions as a). c) Rate of Rh_{NP} site loss (%/hr), resulting in Rh_{iso} site production, measured at identical conditions to a) and b).

weight loading. The results shown in Figures 3.12,3.14 provide strong evidence that the observed reduction in CH_4 selectivity with time on stream in H_2 lean conditions is due to reaction condition induced disintegration of Rh nanoparticles to form a higher concentration of Rh_{iso} sites that are uniquely selective for CO production. Based on the higher rate of selectivity and site fraction change at higher Rh weight loadings it also seems that the driving force for the reaction condition induced disintegration of Rh nanoparticles is the initial concentration of Rh nanoparticles.

3.5 Discussion

Recent reports have demonstrated the significant catalytic reactivity of supported isolated catalytic atoms or single atoms that were previously masked by the co-existence of metal clusters or nanoparticles. A majority of this work investigated noble metals (Pt, Pd, Au, and Rh) catalyzing the water-gas-shift (WGS) reaction and CO oxidation.[7,10–12,28–32] For instance, Fu et al. identified the water-gas-shift active site to be single nonmetallic Au or Pt atoms supported on ceria, where the metallic nanoparticles served as spectator species.[10] Another interesting application of isolated catalytic atoms is the single atom alloy system, where a metal is isolated at the surface of a different metal to exploit the functionality of both metals. Kyriakou et al. showed that functionality can be added by introducing isolated Pd atoms which drive H_2 dissociation on a Cu surface which allows for facile product desorption, to obtain a more ideal balance between dissociation and desorption.[7] These reports typically rely on synthetic protocols to create catalysts with a predominance of single isolated sites and microscopy or spectroscopy based characterizations to identify the existence of the species. Through this approach reactivity

assignments of the isolated sites are demonstrated. However, in these approaches it can be difficult to quantitatively demonstrate these relationships due to the small sample size of microscopy based characterization, or difficult fitting procedures for X-Ray absorption spectroscopy analysis of samples with heterogeneous distributions of metal cluster sizes.[33] Furthermore, the focus of these studies has been on the unique reactivity of isolated sites in single reaction pathway reactions (i.e. only one potential product) rather than the potential for isolated sites to exhibit unique selectivity compared to nanoparticles consisting of the same metal.

Unlike the previous demonstrations, our investigation relies on site-specific characterization approaches that allow for quantitative site type-reactivity assignments, which demonstrate that isolated metal atoms and metal nanoparticles composed of the same metal on the same support can exhibit unique selectivity in a parallel reaction pathway. Similar relationships were recently suggested for Pd and Ru based systems, although only qualitative evidence could be provided based on TEM analyses of the catalysts.[18,19] In addition, unique reactivity of $Rh(C_2H_4)_2$ complexes and few atom Rh clusters for ethane hydrogenation and dimerization have been qualitatively correlated based on x-ray absorption spectroscopy.[12] In our studies, the DRIFTS based CO chemisorption characterization approach was crucial for quantifying site type fractions and allowing proper CO:Rh normalization of total Rh site concentrations that enabled quantitative TOF calculations. In demonstrating quantitative site type-reactivity relationships, we relied on the unique frequencies and existing extinction coefficients for CO intramolecular vibrational modes on different Rh site types. In the context of single site reactivity, our

work highlights the utility of probe molecule FTIR spectroscopy for quantifying the concentration of isolated and nanoparticle metal sites on a catalyst to convincingly assign the unique reactivity to each site type in parallel reaction pathways.

It is worth discussing a quantitative comparison of the results shown in Figures 3.10, 3.12(b) and 3.14(b,c). The measurements in Figure 3.10 show that at a $10CO_2$:H_2 feed ratio the average site-specific r-WGS TOF on Rh_{iso} sites is 0.029 molecules CO/Rh_{iso} site/second while the site-specific methanation TOF on Rh_{NP} sites was determined to be 0.0059 molecules CH_4/Rh_{NP} site/second. This shows that the site-specific TOF for the r-WGS reaction on the Rh_{iso} sites is nearly 5 times faster than the average site-specific methanation TOF on the Rh_{NP} sites at these conditions. However, under the same conditions there is a proportional 1:1 agreement observed between the rates of change in TOF (d(TOF)/dt) for the r-WGS (increase) and methanation (decrease), as shown in Figure 3.12(b). Consistent with the data in Figure 3.12(b), there is also a 1:1 agreement between the decrease in methane selectivity and in Rh_{NP} site fraction, as shown in Figures 3.14(b),(c). The proportional agreement observed in Figure 3.12,3.14 require the following equality to hold true:

$$TOF_{iso} \times \Delta Rh_{iso} = \sum_{i=1}^{n} TOF_{NP,i} \times \Delta Rh_{NP,i}$$

In this equality the TOFs represent site-specific TOFs, where TOF_{iso} is for r-WGS on Rh_{iso} sites and TOF_{NP} are for methanation on Rh_{NP} sites. Based on the results in Figure 3.8, 3.9 and 3.10 it is assumed that r-WGS only occurs at Rh_{iso} sites, while methanation only occurs at Rh_{NP} sites. The ΔRh's represent the change in concentration of each site type due to time on stream under reaction conditions, which we attribute primarily to the

disintegration of nanoparticles to form Rh_{iso} sites. For Rh_{NP} sites, a concentration-weighted sum is used because different sites existing on nanoparticles (corner, edge, terrace, and perimeter) potentially exhibit different site-specific methanation TOFs. To rationalize this equality in the context of the measured average site-specific TOF, we will first consider how the disintegration of nanoparticles to form isolated sites occurs.

Recently, it was predicted that smaller Rh particles are more likely to undergo disintegration than larger Rh particles, due to their high surface free energies.[34,35] The small particles (<1.5 nm) that are most likely to disintegrate have high surface to bulk atom ratios (dispersions nearing 1) and thus when a single Rh_{NP} atom is removed from a small nanoparticle to form an Rh_{iso} site on the support, it is likely that there would not be an underlying bulk Rh atom to expose. This suggests that $\Delta Rh_{iso} \sim \sum_{i=1}^{n} \Delta Rh_{NP,i}$. Considering the similar absolute change in Rh_{iso} and Rh_{NP} site concentrations and the average site-specific TOF ratio of ~5TOF_{iso}:TOF_{NP} under conditions explored in Figure 3.12 and 3.14, the Rh_{NP} sites that transfer from the nanoparticle surface to become Rh_{iso} sites must have site-specific methanation TOFs much larger than the average site-specific methanation TOF_{NP}. The proposed difference in reactivity between different site types is justified by recent studies showing that the CO_2 methanation TOF on Ru nanoparticles increases ~5-fold in the diameter window 1-1.5 nm.[36] Based on this analysis we propose that the change in CH_4 selectivity with time on stream occurs by disintegration of small Rh nanoparticles to form Rh_{iso} sites and that disintegration occurs by loss of Rh_{NP} sites that exhibit site-specific methanation TOF much larger than the average site-specific TOF of all Rh_{NP} sites. Future studies will focus on exploring this disintegration process, specifically to identify

the nanoparticle sizes that are most probable to disintegrate and on the types and number of Rh_{NP} sites being lost during this process.

Our results raise questions about why the two active site types (Rh_{NP} and Rh_{iso}) exhibit such different selectivity in CO_2 reduction. The significant difference in CO_2 reduction selectivity can be rationalized by considering the ensemble of active sites surrounding Rh_{iso} and Rh_{NP} sites. Rh sites located on a nanoparticle, Rh_{NP}, will be surrounded by other Rh sites that are active for H_2 dissociation, but also bind CO very strongly. This suggests that sequential steps hydrogenating CO, or directly CO_2, to produce CH_4 will be favored over CO desorption.[37,38] Alternatively, isolated Rh sites on oxide supports bind CO more weakly than Rh nanoparticles sites, suggesting that the final step for r-WGS should be more facile on Rh_{iso} sites compared to Rh_{NP} sites. In addition, the lack of atomic H adsorption sites on the oxide support surrounding Rh_{iso} sites suggests that sequential hydrogenations of CO or CO_2 on the oxide or Rh_{iso} site would be quite improbable. Another way the selectivity difference between the Rh_{NP} and Rh_{iso} can be rationalized is based on the difficulty associated with an 8-electron reduction of CO_2 to CH_4 occurring at single metal atoms, which would be more facile at an Rh_{NP} site with an ensemble of other Rh atoms surrounding. This simple mechanistic picture substantiates our proposed assignments of Rh_{iso} sites being uniquely active for r-WGS and Rh_{NP} sites being uniquely active for CO_2 methanation.

It is also important to discuss the observed reaction condition induced disintegration of Rh nanoparticles into Rh_{iso} sites that is in opposition to typically seen agglomeration of small collections of metal atoms into larger nanoparticles, Ostwald ripening. Previous

studies have shown that exposure of Rh nanoparticles on oxide supports to ambient temperature CO environments induced disintegration of nanoparticles into isolated Rh sites.[8,26,34,39] It has also been shown that elevated temperatures, in solely H_2 or CO environments, can cause the Rh_{iso} sites to re-associate with nearby Rh nanoparticles.[26,40] To investigate the effect of reaction environment on disintegration, we tested 6% Rh/TiO_2 at 200 °C in 10%CO_2:1%H_2, 10% CO_2, 10%CO:4% H_2, and 10% CO all with an Ar balance for 90 minutes. 10% CO_2 had no observable effect on site fractions, whereas both 10%CO:4%H_2 and 10% CO caused the Rh_{iso} sites to convert to Rh_{NP} sites in direct contrast to the Rh_{NP} to Rh_{iso} conversion observed at 10%CO_2:H_2 shown in figure 3.14. The results suggest that high chemical potentials of surface bound species specific to CO_2 methanation on Rh nanoparticles experienced under the H_2 lean conditions (10CO_2:H_2) drove the disintegration of Rh nanoparticles into Rh_{iso} sites. Furthermore, the driving force for the disintegration may be a complex function of surface bound species on Rh, as well as the TiO_2 surface termination, which could both impact the stability of isolated sites.

3.6 Conclusions:

To summarize, we have demonstrated quantitative relationships between the concentration of isolated and nanoparticle-based Rh sites on TiO_2 supports and the CO_2 reduction selectivity towards CO and CH_4 production, respectively. It was also observed that the relative fraction of these site types on TiO_2 change dynamically under reaction conditions through nanoparticle disintegration to form isolated sites and that this process controls the unstable reactivity of higher Rh weight loadings under H_2 lean conditions with time on stream. These insights provide important information for the design of highly

reactive and selective CO_2 reduction catalysts and stress the importance of considering how the catalyst structures may change under reaction conditions. Furthermore, this work emphasizes the importance of considering catalytic sites that may go undetected with traditional TEM approaches when developing rigorous structure function relationships in catalysis.

3.7 References:

1 Nørskov, J. K.; Bligaard, T.; Hvolbaek, B.; Abild-Pedersen, F.; Chorkendorff, I.; Christensen, C. H. *Chem. Soc. Rev.* **2008**, *37*, 2163.

2 Schweitzer, N. M.; Schaidle, J. a; Ezekoye, O. K.; Pan, X.; Linic, S.; Thompson, L. T. *J. Am. Chem. Soc.* **2011**, *133*, 2378.

3 Christopher, P.; Linic, S. *J. Am. Chem. Soc.* **2008**, 11264.

4 Christopher, P.; Linic, S. *ChemCatChem* **2010**, *2*, 78.

5 Andersson, M. P.; Remediakis, I. N.; Bligaard, T.; Jones, G.; Lytken, O.; Horch, S.; Nielsen, J. H.; Sehested, J.; Chorkendorff, I. *J. Catal.* **2008**, *255*, 6.

6 Underwood, R. P.; Bell, A. T. *Appl. Catal.* **1987**, *34*, 289.

7 Kyriakou, G.; Boucher, M. B.; Jewell, A. D.; Lewis, E. a; Lawton, T. J.; Baber, A. E.; Tierney, H. L.; Flytzani-Stephanopoulos, M.; Sykes, E. C. H. *Science* **2012**, *335*, 1209.

8 Tao, F.; Dag, S.; Wang, L.-W.; Liu, Z.; Butcher, D. R.; Bluhm, H.; Salmeron, M.; Somorjai, G. a. *Science* **2010**, *327*, 850.

9 Tao, F.; Grass, M. E.; Zhang, Y.; Butcher, D. R.; Renzas, J. R.; Liu, Z.; Chung, J. Y.; Mun, B. S.; Salmeron, M.; Somorjai, G. A. **2008**, 932.

10 Fu, Q.; Saltsburg, H.; Flytzani-Stephanopoulos, M. *Science* **2003**, *301*, 935.

11 Flytzani-Stephanopoulos, M. *Acc. Chem. Res.* **2014**, *47*, 783.

12 Serna, P.; Gates, B. C. *Angew. Chemie* **2011**, *123*, 5642.

13 Karelovic, A.; Ruiz, P. *J. Catal.* **2013**, *301*, 141.

14 González-Carballo, J. M.; Pérez-Alonso, F. J.; Ojeda, M.; García-García, F. J.; Fierro, J. L. G.; Rojas, S. *ChemCatChem* **2014**, *6*, 2084.

15 Bezemer, G. L.; Bitter, J. H.; Kuipers, H. P. C. E.; Oosterbeek, H.; Holewijn, J. E.; Xu, X.; Kapteijn, F.; van Dillen, a J.; de Jong, K. P. *J. Am. Chem. Soc.* **2006**, *128*, 3956.

16 Behrens, M.; Studt, F.; Kasatkin, I.; Kühl, S.; Hävecker, M.; Abild-Pedersen, F.; Zander, S.; Girgsdies, F.; Kurr, P.; Kniep, B.-L.; Tovar, M.; Fischer, R. W.; Nørskov, J. K.; Schlögl, R. *Science* **2012**, *336*, 893.

17 Karelovic, A.; Ruiz, P. *Appl. Catal. B Environ.* **2012**, *113-114*, 237.

18 Kwak, J. H.; Kovarik, L.; Szanyi, J. *ACS Catal.* **2013**, *3*, 2449.

19 Kwak, J. H.; Kovarik, L.; Szanyi, J. *ACS Catal.* **2013**, *3*, 2094.

20 Harjanto, S.; Cao, Y.; Shibayama, A.; Naitoh, I.; Nanami, T.; Kasahara, K.; Okumura, Y.; Liu, K.; Fujita, T. *Mater. Trans.* **2006**, *47*, 129.

21 Sirita, J.; Phanichphant, S.; Meunier, F. C. *Anal. Chem.* **2007**, *79*, 3912.

22 Duncan, T. M.; Yates Jr., J. T.; Vaughan, R. W. *J. Chem. Phys.* **1980**, *73*, 975.

23 Yang, A.C., Garland, C. . *J. Phys. Chem.* **1957**, *61*, 1504.

24 Yates Jr., J. T.; Duncan, T. M.; Worley, S. D.; Vaughan, R. W. *J. Chem. Phys.* **1979**, *70*, 1219.

25 Cavanagh, R. R., Yates Jr., J. T. *J. Chem. Phys.* **1981**, *74*, 4150.

26 Solymosi, F.; Pdsztor, M. *J. Phys. Chem.* **1985**, 4789.

27 Zhang, Z.; Verykios, X. *J. Catal.* **1994**, *148*, 737.

28 Boccuzzi, F.; Chiorino, A.; Manzoli, M.; Andreeva, D.; Tabakova, T. *J. Catal.* **1999**, *185*, 176.

29 Fu, Q.; Deng, W.; Saltsburg, H.; Flytzani-Stephanopoulos, M. *Appl. Catal. B Environ.* **2005**, *56*, 57.

30 Fu, Q.; Kudriavtseva, S.; Saltsburg, H.; Flytzani-Stephanopoulos, M. *Chem. Eng. J.* **2003**, *93*, 41.

31 Liu, Z.-P.; Jenkins, S.; King, D. *Phys. Rev. Lett.* **2005**, *94*, 196102.

32 Yang, M.; Allard, L. F.; Flytzani-Stephanopoulos, M. *J. Am. Chem. Soc.* **2013**, *135*, 3768.

33 Fierro-Gonzalez, J. C.; Kuba, S.; Hao, Y.; Gates, B. C. *J. Phys. Chem. B* **2006**, *110*, 13326.

34 Goldsmith, B. R.; Sanderson, E. D.; Ouyang, R.; Li, W.-X. *J. Phys. Chem. C* **2014**, *118*, 9588.

35 Ouyang, R.; Liu, J.-X.; Li, W.-X. *J. Am. Chem. Soc.* **2013**, *135*, 1760.

36 Abdel-Mageed, A. M.; Eckle, S.; Anfang, H. G.; Behm, R. J. *J. Catal.* **2013**, *298*, 148.

37 Beuls, A.; Swalus, C.; Jacquemin, M.; Heyen, G.; Karelovic, A.; Ruiz, P. *Appl. Catal. B Environ.* **2012**, *113-114*, 2.

38 Porosoff, M. D.; Chen, J. G. *J. Catal.* **2013**, *301*, 30.

39 N. Kruse, A. G. *J. Catal.* **1993**, *144*, 525.

40 Solymosi, F.; Pásztor, M. *J. Phys. Chem.* **1986**, *90*, 5312.

Chapter 4 Adsorbate-Mediated Strong Metal-Support Interactions in Oxide Supported Rh Catalysts

4.1 Summary

Optimization of supported metal catalysts predominantly focuses on engineering the metal site, where physical insights based on extensive theoretical and experimental contributions have enabled rational design of active sites. While it is well known that supports can influence the catalytic properties of metals, physically transparent insights into how metal-support interactions can be exploited to optimize metal active site properties are lacking. In this chapter, we utilize *in-situ* spectroscopy and microscopy to identify and characterize a support-effect in oxide-supported heterogeneous Rh catalysts, where strongly bound adsorbates (HCO_x) on reducible oxide supports (TiO_2 and Nb_2O_5) induce oxygen-vacancy formation in the support, causing HCO_x functionalized support encapsulation of Rh nanoparticles. The encapsulation layer is permeable to reactants, stable under reaction conditions, and strongly influences the catalytic properties of Rh, enabling rational and dynamic tuning of CO_2 reduction selectivity.

4.2 Introduction

The identification of optimal active sites on supported metal catalysts often focuses on engineering the composition or geometry of the metal site for maximizing reaction rate or controlling reaction selectivity.[1–5] Much less is known about how metal-support interactions can be exploited to control the reactivity of heterogeneous metal oxide supported metal catalysts, although support characteristics can impact catalytic reactivity or selectivity as considerably as characteristics of the metal.[6,7] Demonstrated mechanisms of support effects on metal nanoparticle reactivity include small cluster stabilization,[8]

charge transfer,[9–12] support participation in catalysis,[7,13,14] and oxide encapsulation of metal nanoparticles.[15–19]

Encapsulation of metal nanoparticles by reducible oxide support overlayers is the only mechanism by which supports can affect catalysis at a majority of active sites on metal particles with a diameter larger than 1-2 nm,[12] and was designated by Tauster[15] as strong metal support interactions (SMSI). The SMSI encapsulation state forms due to high temperature H_2 treatment of reducible oxide-supported Pt-group metals, causing a reduction of the oxide support to sub-stoichiometric oxygen concentrations and inducing oxide migration on top of metal nanoparticles. Bonding between cationic support metal atoms and the metal catalyst surface makes migration of the support onto the metal thermodynamically favorable.[20]

Excitement surrounding the discovery of SMSI overlayers was stoked by the suggestion that the SMSI state could potentially be used to tune metal catalyst reactivity via partial decoration of metals by oxide overlayers.[16] However, the SMSI state rarely finds an intermediate configuration where partial metal coverage by the oxide allows interaction with a majority of exposed metal sites. Instead, the oxide overlayer either covers all metal sites, rendering catalysts inactive, or retreats off the metal due to re-oxidation of the reduced support by H_2O or O_2,[21,22] creating a situation where only a small fraction of metal sites are influenced by the partially reduced support, specifically at the metal-support interface.[23–26] The poisoning or receded SMSI overlayer structures that exist under catalytic reaction conditions have curtailed the use of SMSI overlayers to increase reactivity or control selectivity on supported metal catalysts.

Here we demonstrate an SMSI encapsulation state that forms due to treatment of TiO_2 and Nb_2O_5 supported Rh nanoparticles in CO_2-H_2 (CO_2-rich) environments at temperatures of 150-300 °C. *In-situ* spectroscopy and microscopy show that a high coverage of adsorbates (HCO_x) on the support induces oxygen vacancy formation, driving migration of the adsorbate-functionalized support onto the metal. This adsorbate-mediated SMSI (A-SMSI) encapsulation state is stabilized against re-oxidation by H_2O and modifies the reactivity of all remaining exposed Rh sites, appearing to be comprehensive in covering Rh but amorphous and permeable to reactants. Formation of the A-SMSI state induces a selectivity switch in the CO_2 reduction reaction from CH_4 production on bare Rh particles to CO production in the A-SMSI state, effectively rendering Rh less active for C-H bond formation. Our results show that the A-SMSI state represents a powerful support effect, enabling rational manipulation of metal catalyst reactivity.

4.3 Methods

4.3.1 Synthesis: Rh/TiO_2

Six weight loadings of Rh (0.2%, 0.5%, 1%, 2%, 4%, and 6%) were deposited on TiO_2 (Evonik-P25), to produce total sample masses of 1g each, using a simple impregnation technique. The necessary mass of ($Rh(NO_3)_3 \cdot xH_2O$, Sigma-Aldrich-#83750) for each weight loading was dissolved in an evaporation dish with 2mL of distilled water. TiO_2 was mixed with the aqueous Rh solution using a stir rod until homogeneous, dried at 95 °C for 4 h, ground with a mortar and pestle, and calcined in a tube furnace at 450 °C in air for 4 h. All reductions of the samples were performed in-situ prior to the kinetic and characterization analyses and will be mentioned in their corresponding sections. Similar

catalysts were investigated in chapter 3, and characterization of particle size distributions, concentration of isolated Rh atoms and active surface area can be found there.

4.3.2 Synthesis: Rh supported on Nb_20_5, Al_2O_3, and CeO_2

We also examined the effect of supports by comparing Rh on γ-Al_2O_3 (Inframat Advanced Materials-#26R-0804UPG)), CeO_2 (Sigma-Aldrich-#544841), and Nb_2O_5 (CBMM-HY 340) where the synthesis procedure was identical to the procedure mentioned above, however only 2% Rh was impregnated on these additional supports. All of these supports are non-porous, with surface areas of 83 (γ-Al_2O_3), 63 (CeO_2), 52 (TiO_2), and 122 m^2/g (Nb_2O_5). Based on the similar structures and surface area of the supports, minimal impact of the support geometry was expected in terms of the impact of 20%CO_2:2%H_2, (20CO_2:2H_2 hereafter), treatment on the reactivity.

4.3.3 Catalyst Testing

CO_2 reduction reaction rates and selectivity were measured using 15–20 mg of catalyst at 200 °C in a 1/4" OD borosilicate packed bed reactor operating at atmospheric pressure and running under differential reactor conditions (conversion of limiting reagent <8%) with the effluent quantified by online gas chromatography (GC, SRI MG #3). CO_2 was separated from other gases using a Hayesep D column, while H_2, N_2, CH_4, and CO were separated using a molecular sieve (MS13X) packed column. The separated gases were then quantified using a flame ionization detector (FID) and a thermal conductivity detector (TCD). The total reactant flow rate in all studies was 100 standard cubic cm per minute (sccm). Specifics regarding reactant concentrations and pretreatment conditions can be found in the listed protocols in in sections 4.4.3, 4.4.6, 4.4.7, and 4.4.11.

The standard experimental procedure for all data shown in Figure 4.5,4.6, 4.10-4.14, 4.21a, 4.27(a-c), 4.28 was as follows:

1. **Reduction:** Pure H_2 flow (20 sccm) over catalyst at 450 °C for 1 hour*
2. **Reactivity Assay:** Reduce temperature to 200 °C and flow 1 sccm CO_2, 1sccm H_2, 98 sccm He for reactivity assay of reduced material for 4 hours. Reported CO and CH_4 production rates are associated with steady-state measurements obtained by averaging 5 GC injections over the final hour.
3. **A-SMSI Formation:** Increase temperature to 250 °C and change flow rates to 20 sccm CO_2, 2 sccm H_2, and 78 sccm He for 4 hours.**
4. **Reactivity Assay:** Reduce temperature to 200 °C and flow 1 sccm CO_2, 1sccm H_2, 98 sccm He for reactivity assay of reduced material for 4 hours. Reported CO and CH_4 production rates are associated with steady-state measurements obtained by averaging 5 GC injections over the final hour.
5. **Re-Reduction:** Increase temperature to 450 °C and switch environment to pure H_2 flow (20 sccm) for 4 hours.

*In the case of Rh/Nb_2O_5, a reduction temperature of 300 °C was used to minimize complete Rh encapsulation via traditional SMSI, prior to analyzing the impact of $20CO_2$:$2H_2$ treatment on the reactivity of Rh nanoparticles.[20] This is shown directly in Figure 4.27(c) where the reactivity of the Rh/Nb_2O_5 is compared after 300 °C reduction (bare Rh particles), 400 °C reduction (traditional stable SMSI encapsulation state) and $20CO_2$:$2H_2$ treatment.

** The temperature of the A-SMSI formation step was varied in Figure 4.21(A) to identify similarity to previous observations with formic acid induced TiO_2 reduction.

To demonstrate the reversibility of the impact of reduction and $20CO_2$:$2H_2$ treatments on catalytic reactivity, steps 2-5 were repeated at least 2 times, as seen in Figure 4.6,4.10-4.12. Variations of the protocol described above were used to test the catalyst stability, Figure 4.21(B), 4.1-4, 4.7-9, 4.20 and are described below.

4.3.4 Effect of Various Treatments on Catalytic Reactivity

Experiments analyzing the impact of CO_2, H_2 and CO treatments on the CO_2 reduction reactivity of Rh catalysts were performed by treating catalysts for 4 hours at 250 °C with 100 sccm total flowrate using the gas compositions listed in Table 4.1. After treatment, catalysts were tested at the standard reactivity assay conditions of 200 °C 1% CO_2, 1% H_2, 100 sccm total flow rate. Essentially, the protocol was identical to what is shown above, with a modified step 3 to test the impact of other treatments on the catalysts reactivity.

4.3.5 Stability testing of the CH_4 and CO producing states

Experiments were designed with the goal of finding CO_2 reduction reaction conditions where Rh/TiO_2 catalysts were stable in both the CO (A-SMSI) and CH_4 (bare Rh particles) producing states and to identify conditions where both of these states become unstable. To test the stability of the CH_4 producing state, Rh/TiO_2 catalysts were reduced at 450 °C, and then exposed to CO_2 reduction reaction conditions with varying CO_2 and H_2 partial pressures at a constant temperature of 200 °C starting at low ratios tested in ascending the ratios as shown in Figure 4.2.

4.3.6 DRIFTS Characterization

DRIFTS measurements were executed to identify how the various treatments explored in this study impact the species adsorbed on the catalyst surface in reaction conditions. Generally, catalysts were loaded into a Harrick Praying Mantis high temperature reaction chamber (ZnSe windows) mounted inside of a Thermo Scientific Praying Mantis diffuse reflectance adapter, set inside of a Thermo Scientific Nicolet iS10

FT-IR spectrometer with a MCT-A detector. Measurements were taken with 128 scans, 4 cm^{-1} resolution, and a 30-40 standard liters per minute N_2 purge of the spectrometer and Praying Mantis adapter box to minimize the effect of variations in atmospheric water and CO_2 from falsely appearing in the spectra. Typically, 10 mg of the catalyst sample was packed on top of 100 mg of α-alumina. The reactor effluent was routed to the GC to monitor reactivity of the catalyst and ensure consistent behavior with experiments performed in the glass reactors.

After loading the catalysts in the reactor, the following steps were taken for the DRIFTS cycling experiments to identify how the species on the catalyst surface under reaction conditions (1%CO_2:1%H_2:98%He, 180 °C) following reduction and A-SMSI formation, and the reversibility of this process, (Figure 4.2, 4.29-4.30, 4.29-4.31):

1. **Reduction:** Pure H_2 flow (20 sccm) over sample at 350 °C* for 1 hour
2. **FTIR Background:** Changed temperature to 180 °C* and collected background spectrum in H_2.
3. **Reactivity Assay:** Changed flows to 1 sccm CO_2, 1 sccm H_2, 98 sccm He and allowed the system 20 minutes to reach steady state prior to collecting a spectrum of the reduced material in reaction conditions.
4. **A-SMSI Formation:** Changed temperature to 210 °C* and flowrates to 20 sccm CO_2, 2 sccm H_2, and 78 sccm He for 16 hours* to induce A-SMSI formation.
5. **Reactivity Assay:** Changed temperature to 180 °C* and flowrates to 1 sccm CO_2, 1 sccm H_2, 98 sccm He and allowed the system 20 minutes to reach steady state prior to collecting a spectrum of the catalyst in reaction conditions and the A-SMSI state.
6. **Re-Reduction:** Pure H_2 flow (20 sccm) over sample at 350 °C* for 4 hour.
7. **Reactivity Assay:** Changed temperature to 180 °C* and flowrates to 1sccm CO_2, 1sccm H_2, 98 sccm He and allowed the system 20 minutes to reach steady state prior to collecting a spectrum of the re-reduced catalyst.

*Note: The A-SMSI formation step was performed for 16 hours in the DRIFTS studies instead of 4 hours used in the reactivity studies due to a lower temperature at the top of the catalyst bed (where IR spectra are collected from) compared to the set-point

temperature of the catalyst bed. Later temperature calibration indicated the surface of the catalyst was approximately 210 °C rather than the 250 °C used in the kinetic reactor for A-SMSI formation. The 200 °C sampling temperature was also found to only be approximately 180 °C. The 450 °C reduction temperature was later determined to actually be 350 °C. Based on the robustness and consistency of the observed reactivity changes and accompanied changes in adsorbed species in the FTIR experiments, these small temperature differences had no impact on the experimental results or conclusions drawn from the experiments.

4.3.7 DRIFTS Analysis of CO_2 Removal and TPD Experiments (Figure 4.18)

The goals of this experiment were to observe (a) which surface species were acting as reaction intermediates, (b) the coverage dependence of the CO stretch frequency and (c) in the case of the A-SMSI state, the impact of the HCO_x species on the frequency of the stretch associated with CO bound to Rh. We only examined the 2% Rh/TiO_2 catalyst in this set of experiments. In the case of the reduced catalyst, CO_2 was removed from the reactant stream and time-resolved DRIFT spectra were collected to identify reactive species and the coverage dependent frequency of the CO stretch, see Figure 4.19. In the case of the catalyst in the A-SMSI state, an identical experiment was performed, followed by a temperature programmed desorption in He, See Figure 4.18(B). Detailed description of the protocol for each experiment is provided below.

<u>Reduced Catalyst</u>

1. **Reduction:** Pure H_2 flow (20 sccm) over sample at 350 °C* for 1 hour
2. **FTIR Background:** Changed temperature to 180 °C* and obtained FTIR background in H_2.

3. **Reactivity Assay:** Changed flows to 1sccm CO_2, 1sccm H_2, 98 sccm He for 20 minutes to obtain a spectrum of the reduced material in reaction conditions.
4. **CO_2 removal:** Turned off CO_2 flow for 15 minutes and collected spectra every 1-2 minutes.
5. $20CO_2$:$2H_2$ Treated Catalyst
6. **Reduction:** Pure H_2 flow (20 sccm) over sample at 350 °C* for 1 hour
7. **FTIR Background:** Changed temperature to 180 °C* and collected background spectrum in H_2.
8. **Reactivity Assay:** Changed flows to 1 sccm CO_2, 1 sccm H_2, 98 sccm He and allowed the system 20 minutes to reach steady state prior to collecting a spectrum of the reduced material in reaction conditions.
9. **A-SMSI Formation:** Changed temperature to 210 °C* and flowrates to 20 sccm CO_2, 2 sccm H_2, and 78 sccm He for 16 hours* to induce A-SMSI formation.
10. **Reactivity Assay:** Changed temperature to 180 °C* and flowrates to 1 sccm CO_2, 1 sccm H_2, 98 sccm He and allowed the system 20 minutes to reach steady state prior to collecting a spectrum of the catalyst in reaction conditions and the A-SMSI state.
11. **CO_2 removal:** Turned off CO_2 flow for one hour and collected spectra every 5-15 minutes.
12. **He Purge:** A 15 minute 200 sccm He purge was performed to remove any H_2 still in the system, while still at 180 °C*.
13. **TPD:** The sample was then heated at a rate of 20 °C/min with a scan taken every 20 °C to observe at what temperatures the surface formate and carbonate species desorbed and if this affected the monocarbonyl peak.

*Note: The A-SMSI formation step was performed for 16 hours in the DRIFTS studies instead of 4 hours used in the reactivity studies due to a lower temperature at the top of the catalyst bed (where IR spectra are collected from) compared to the set-point temperature of the catalyst bed. Later temperature calibration indicated the surface of the catalyst was approximately 210 °C rather than the 250 °C used in the kinetic reactor for A-SMSI formation. The 200 °C sampling temperature was also found to only be 180 °C. The 450 °C reduction temperature was later determined to actually be 350 °C. Based on the robustness and consistency of the observed reactivity changes and accompanied changes in absorbed species in the FTIR experiments, these small temperature differences had no impact on the experimental results or conclusions drawn from the experiments.

4.3.8 XAS Characterization

XAS experiments were performed at Beamline 2-2 at the Stanford Synchrotron Radiation Light source (SSRL). A double-crystal Si (220) monochromator was used to scan X-ray energy from -100 to 200 eV and -200 eV to 1300 eV relative to the Rh K-edge (23,220 eV) for XANES and EXAFS spectra, respectively. About 20 mg of 2% Rh/TiO_2 catalyst was placed in 2.4 mm OD quartz tubes and into a resistance heating-capable Claussen cell[27] with gas flowing through the powder. Rh foil was placed between the transmission and reference X-ray detectors and measured simultaneously with the nanoparticle samples for X-ray energy calibration and data alignment. Data were recorded for an untreated sample at room temperature, at 400 °C in H_2 flow for reduced catalyst and at 250 °C with 20%CO_2/2%H_2/78%He flow all at 20 mL/min. Although the XAS data were obtained in both transmission and fluorescence modes, only transmission spectra are presented. Rh foil was placed between the transmission and reference X-ray detectors and measured simultaneously with the nanoparticle samples for X-ray energy calibration and data alignment. Data processing and analysis were performed using the IFEFFIT package.[28] The amplitude and phase photoelectron scattering functions for the first nearest neighbor (1NN) photoelectron path were calculated using the FEFF6 program[29] and used to fit the EXAFS equation in R-space.

4.3.9 Ex-Situ and In-Situ Scanning Transmission Electron Microscopy (STEM)

All STEM analysis was executed on a JEOL 3100R5 with double Cs corrector operated at 300kV. The 2%Rh/TiO_2 samples were suspended in methanol via sonication

and drop casted onto lacy carbon-on-copper grids for *ex-situ* analysis and a special SiN heater chip for *in-situ* observation, which utilized a Protochips Atmosphere system. The purity of gases used in the *in-situ* experiment was 99.9995%. All reported temperatures were based on the Protochips calibration.

4.3.10 Sinter-Induced Rh particle growth for EELS and STEM

A sintering process was employed to increase Rh particle size to improve STEM resolution of overlayer covering Rh NP's and to test the effect of Rh particle size on the observed catalytic behavior after $20CO_2$:$2H_2$ treatment as mentioned in the main text.

Rh NP Sintering Protocol

A 6% Rh/TiO_2 sample was synthesized with the method described in section 4.3.1 and then sintered at 800 ˚C in N_2 for 3h to induce Rh particle size growth. The Rh particle size increased from 1-3 nm up to 10-50 nm and the TiO_2 crystallite size grew from 20-30nm up to 100-200nm as a result of the sintering treatment, as shown in Figure 4.22.

4.3.11 Reactivity experiments investigating effect of larger Rh particle size

After sintering treatment was performed to increase Rh particle size, the reactivity of this 6%Rh/TiO_2 sample with larger Rh particle size was tested to ensure that the larger particles behave similarly to smaller particles with respect to reactivity so that images of the larger NPs can translate to the smaller NPs. These experiments were performed using the same setup and protocol described in S2 with the exception that ~70mg of sample was packed into the reactor to make up for dramatically decreased dispersion associated with 10-50 nm Rh particle diameter. The order of experimental steps was as follows:

1. **Reduction:** Pure H_2 flow (20 sccm) over catalyst at 450 °C for 1 hour

2. **Reactivity Assay:** Reduce temperature to 200 °C and flow 1 sccm CO_2, 1sccm H_2, 98 sccm He for reactivity assay of reduced material for 4 hours. Reported CO and CH_4 production rates are associated with steady-state measurements obtained by averaging 5 GC injections over the final hour.
3. **A-SMSI Formation:** Increase temperature to 250 °C and change flow rates to 20 sccm CO_2, 2 sccm H_2, and 78 sccm He for 4 hours.
4. **Reactivity Assay:** Reduce temperature to 200 °C and flow 1 sccm CO_2, 1sccm H_2, 98 sccm He for reactivity assay of reduced material for 4 hours. Reported CO and CH_4 production rates are associated with steady-state measurements obtained by averaging 5 GC injections over the final hour.

4.3.12 Observing the Physical and Chemical Nature of the SMSI and A-SMSI Overlayer using In-Situ STEM and EELS with Sintered 6%Rh/TiO_2

SMSI A 6% Rh/TiO_2 sample prepared according to section S1 (450 ˚C calcination) was sintered in N_2 at 800 ˚C for 3h and then placed in sample holder and STEM as described in 4.3.9. Catalyst was then *in-situ* treated with H_2 at 550 ˚C for 10 minutes to observe crystalline bilayer SMSI overlayer formation Figure 4.23(A).

A-SMSI A 6% Rh/TiO_2 sample prepared according to 4.3.1 (450 ˚C calcination) was sintered in N_2 at 800 ˚C for 3h and then placed in sample holder and STEM as described in 4.3.9. Catalyst was then *in-situ* treated with $20CO_2$:$2H_2$ at 250 ˚C for 3 hours to observe the formation of an amorphous overlayer as shown in Figure 4.23(B).

Electron Energy Loss Spectroscopy was performed to identify the existence of Ti in the amorphous A-SMSI overlayer and characterize the Ti valance state. EELS data was collected in-situ when the sample was sandwiched between two SiN membranes, with a total thickness of 80nm, using the Gatan #965 Quantum Imaging Filter (GIF). The spot size was 1.0-1.5Å in diameter and typical acquisition time was 10 seconds. The Ti valence was quantified by using Multiple Linear Least Square (MLLS) Fitting with Digital Micrograph.

4.4 Results

4.4.1 Changes in reactivity

In a recent analysis of TiO_2 supported Rh (Rh/TiO_2) catalysts for the reduction of CO_2 by H_2, we observed a dynamic decrease in the rate of CH_4 production and increase in that of CO production when operating at CO_2:H_2 ratios greater than 1.[5] Based on an assignment of CO production occurring at isolated Rh atoms and CH_4 production occurring at Rh nanoparticle surfaces, the dynamic reactivity change was attributed to Rh nanoparticle disintegration into isolated Rh atoms. However, the disproportionate magnitude of the change in CO and CH_4 production rates with longer times on stream

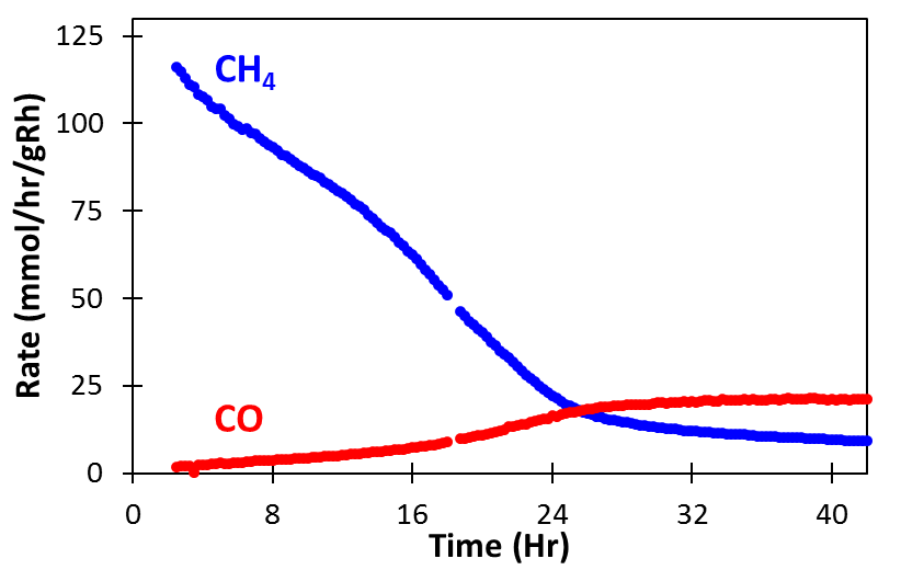

Figure 4.1 Fig. 4.1 Rate of CO and CH_4 production as a function of time on stream over 6% Rh/TiO_2 catalyst operating at 200 °C 5% CO_2:5%H_2, 100 sccm. Over the course of 42 hours, an 11-fold decrease in CH_4 production and 12-fold increase in CO production was observed. If the mechanism of the switch in reactivity were due to Rh nanoparticle disintegration into exclusively isolated Rh atoms, the total number of active sites would increase, and therefore the total CO_2 reduction rate should also increase. However, the total CO_2 conversion rate decreases as the selectivity to CO increases suggesting Rh disintegration is not the mechanism driving changes in catalyst reactivity.

(Figure 4.1) cannot be rationalized by the disintegration mechanism, suggesting that a more complex physical catalyst transformation was responsible for the changing selectivity.

.To understand the controllability and mechanism of the observed dynamic change in CO_2 reduction selectivity, a series of oxide-supported Rh catalysts with varying oxide composition and Rh weight loadings were synthesized via an impregnation method, 4.3.1 and 4.3.2. To explore the effect of various treatments on CO_2 reduction selectivity, Rh/TiO_2 catalysts were reduced at 450 $^{\circ}C$ in H_2, evaluated for reactivity at $1\%CO_2$:$1\%H_2$:98%He and 200 $^{\circ}C$ (reaction conditions were chosen for catalyst stability, see Fig. 4.2 and 4.3 used throughout the report except when stated otherwise), exposed to various environments (see Table 4.1), and evaluated again for reactivity at $1\%CO_2$:$1\%H_2$:98%He and 200 $^{\circ}C$. Only treatments in CO_2:H_2 environments with CO_2:H_2 feed ratio greater than 1 induced a rapid (on the time scale of 4 hours) selectivity switch from CH_4 production on the reduced catalysts to CO production on the treated Rh/TiO_2 catalysts.

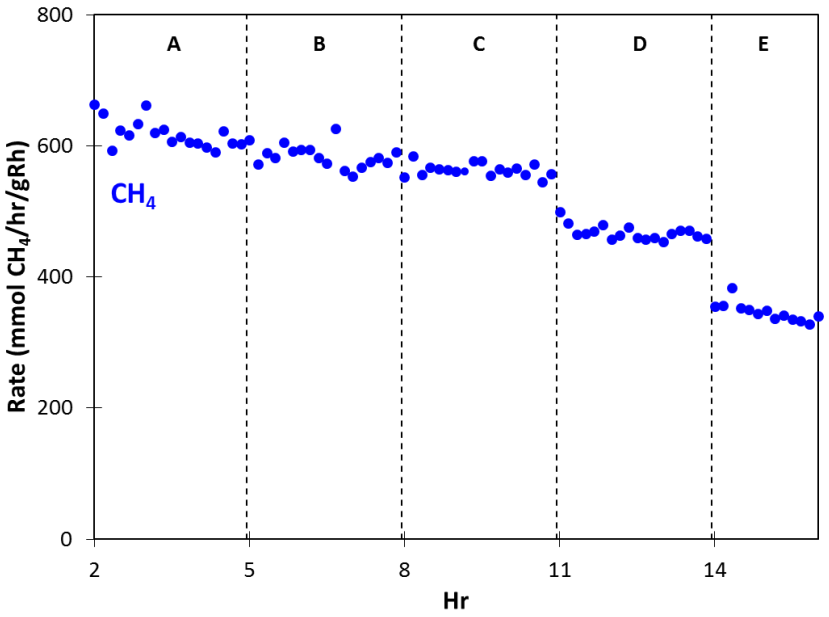

Figure 4.2 Impact of CO_2:H_2 ratio on CH_4 production stability. Rate of CH_4 production over 4 hour time periods at varying CO_2:H_2 flow rates (A-4:16, B-4.5:13.5, C-6:12, D-9:9, E-12:6, all in sccm with balance He to 100 sccm total flow) over 6% Rh/TiO_2 at 200 °C. The catalyst showed stable reactivity until the CO_2:H_2 ratio was larger than 1:1 (E), where we started to observe increased CO production and decreased CH_4 production. CO was not observed in this experiment, due to the use of a different GC (lower detection limit) than the rest of the experiments in this work.

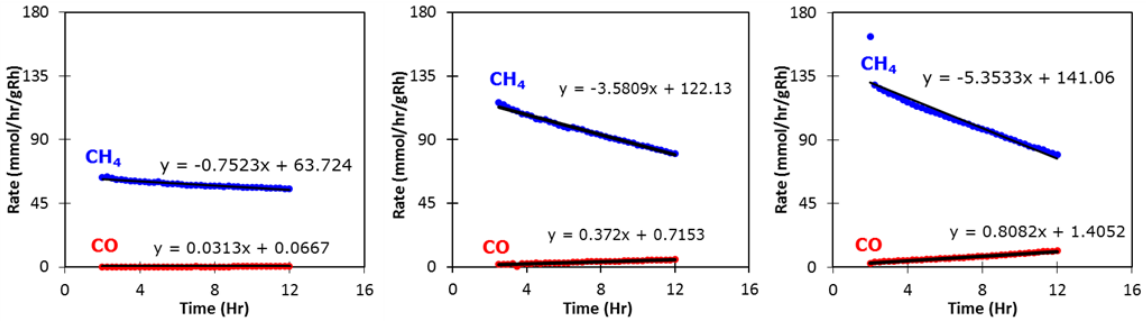

Figure 4.3 Effect of reactant partial pressure during sampling at a) 1%CO_2:1%H_2:98%He, b) 5%CO_2:5%H_2:90%He c) 9%CO_2:9%H_2:82%He. These experiments were performed with 6% Rh/TiO_2, which was the least stable weight loading and 200 °C. Here we show the change in rate of production over time, demonstrating good stability in 1:1 at short time scales.

Table 4.1 Effect of varying environmental conditions on CH_4 selectivity, all treated catalysts were sampled at standard 1%CO_2/1%H_2/98%He conditions (100 standard cubic centimeters per minute, sccm, total) and 200 ˚C

Pretreatment Gases	Effect
20% CO_2/2% H_2	Decrease in Methane Selectivity
20% CO_2	No change in Methane Selectivity
10% CO/1% H_2	No change in Methane Selectivity
20% CO	No change in Methane Selectivity
4.6% Formic Acid (25 sccm)	Decrease in Methane Selectivity, See Fig 4.21(B)

After identifying optimal treatment conditions (20%CO_2:2%H_2:78% He at 250 °C for 4 hours, hereafter 20CO_2:2H_2 treatment) for inducing a selectivity switch from CH_4 to CO production, the reversibility was tested by exposing the 20CO_2:2H_2 treated catalyst to H_2 environments. H_2 treatment at temperatures greater than 350 °C for 4 hours restored the original CH_4 selectivity of the reduced catalyst, see Fig. 4.4.

A complete cycle is shown in Fig. 4.5 for 6% Rh/TiO_2, where CH_4 selectivity decreased from 98% after reduction (450 °C for 4 hours) to 11% following 20CO_2:2H_2 treatment and returned to 98% CH_4 selectivity after re-reduction (450 °C for 4 hours). The switch in CO_2 reduction selectivity was induced by a 40-fold decrease in CH_4 formation rate from ~28 to 0.7 mmol $CH_4/h/g_{Rh}$, and a 10-fold increase in CO formation rate from 0.5 to 5 mmol $CO/h/g_{Rh}$ and was completely reversible for multiple cycles of reduction and 20CO_2:2H_2 treatments, Fig. 4.6. Typical H_2 conversions measured at 1%CO_2:1%H_2:98%He and 200 ˚C were below 8%. To ensure that the change in selectivity following 20CO_2:2H_2 treatment was not due simply to lower reactant conversion, selectivity was compared at

identical conversions (~4%), Fig. 4.7 at 300 ˚C and Fig. 4.8 at 200 ˚C, where large differences in selectivity were still observed.

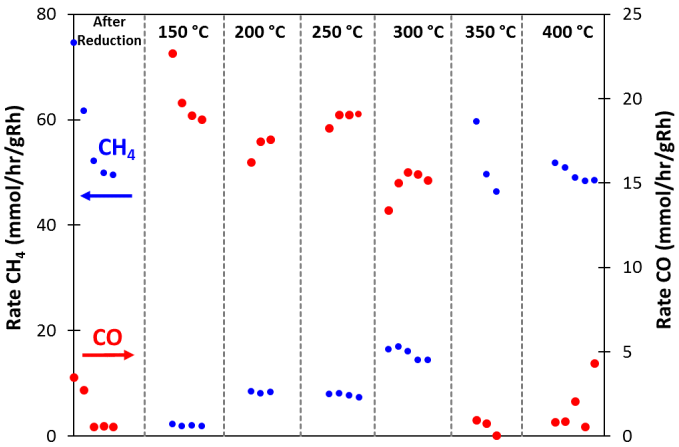

Figure 4.4 Fig. 4.4 Effect of Reduction Temperature on CH_4. The rate of CO and CH_4 production on 2% Rh/TiO_2 catalyst at 200 °C, 1%CO_2:1%H_2 following reduction (panel 1) and 20CO_2:2H_2 treatment followed by re-reduction in H_2 at 150-400 ˚C for four hours (panel 2-7). This experiment was performed sequentially such that after each re-reduction treatment the reactivity was assayed at the standard conditions, exposed to the 20CO_2:2H_2 treatment and re-reduced at an increased temperature. The data shows that the CO producing state was relatively stable during H_2 treatments until the temperature increased above 300 °C CH_4

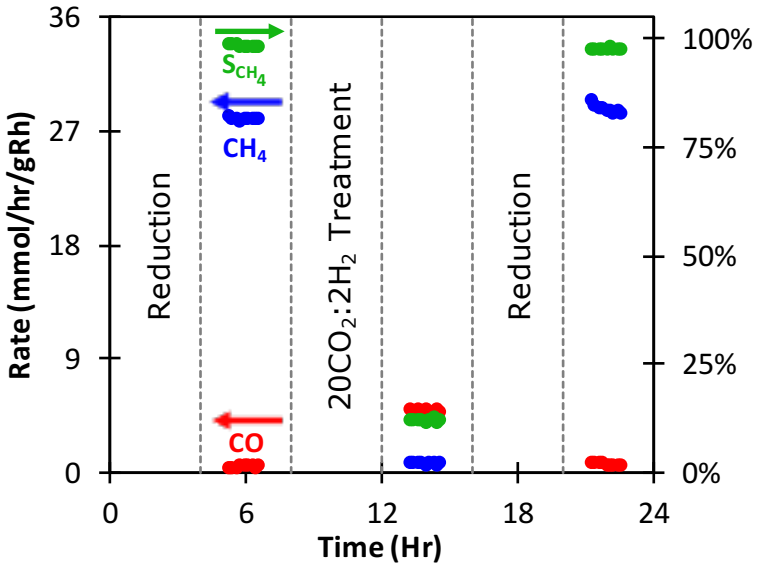

Figure 4.5 Controlling CO_2 reduction selectivity on Rh via catalyst pretreatment. (A) Rate of CO and CH_4 production and selectivity to CH_4 over 6% Rh/TiO_2 measured at 200 °C with a feed composition of 1% CO_2, 1% H_2, 98% He (100 standard cubic centimeters per minute, sccm, total) following pure H_2 at 450 °C (reduction) and 20% CO_2, 2% H_2 and 78% He (100 sccm total, 20CO_2:2H_2) treatments.

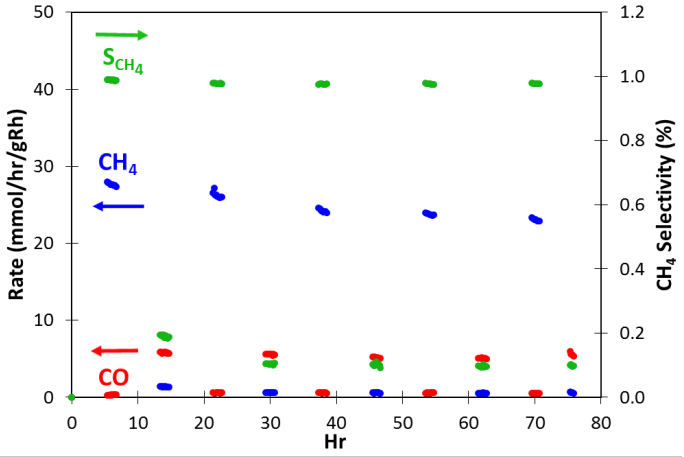

Figure 4.6 Fig. 4.6 Catalyst stability with multiple cycles. The rate of CO and CH_4 production operating at 200 °C 1% CO_2:1%H_2, 100 sccm following sequential cycles of reduction and 20%CO_2:2%H_2 treatment for the 6% Rh/TiO_2 catalyst. The data with high CH_4 production rate and selectivity were after being reduced at 450 °C in pure H_2 for 4h and the data with the high CO production rate and selectivity were after being 20%CO_2:2%H_2 treated. The small decrease in overall rate following each treatment cycle can be attributed to minimal sintering of Rh and loss of active surface area.

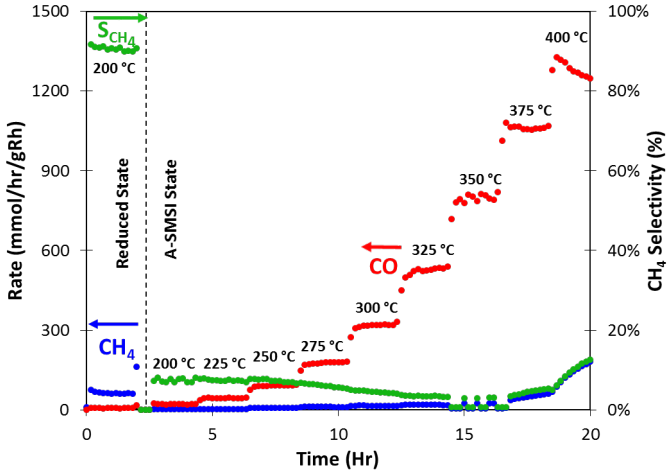

Figure 4.7 Fig. 4.7 Effect of reaction temperature on catalyst stability in A-SMSI state

Rate of CO/CH_4 formation and CH_4 selectivity on 2% Rh/TiO_2 measured at 1% CO_2, 1% H_2, balance He, 200°C after reduction and then 20CO_2:2H_2 treatment, followed by reactivity measurements at increasing temperature. The rate of CH_4 formation didn't begin increasing until reaching >350 °C, or about the temperature that HCO_x adsorbates desorb from TiO_2.

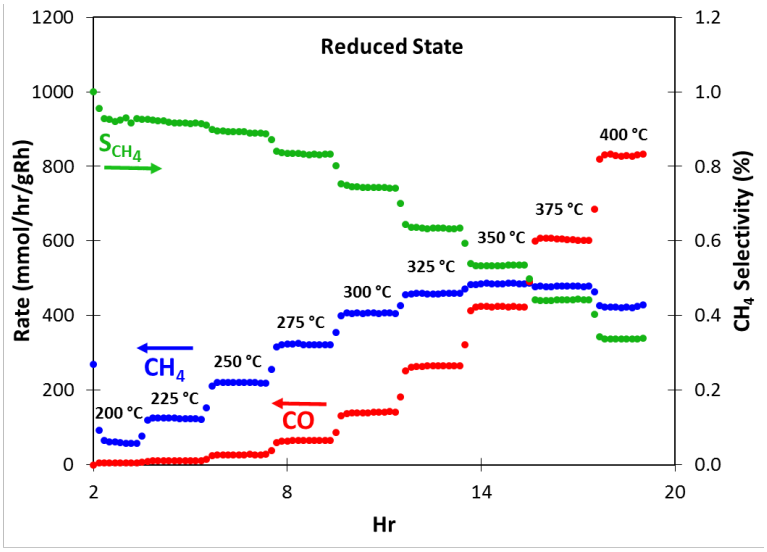

Figure 4.8 Effect of reaction temperature on catalyst stability in H_2-treated state. Rate of CO/CH_4 formation and CH_4 selectivity on 2% Rh/TiO_2 measured at 1% CO_2, 1% H_2, balance He after reduction, as a function of reaction temperature. CH_4 selectivity decreased from 92% at 225 °C to 34% at 400 °C, which is a well-known effect of thermodynamics in this reaction.

Stability of the CH_4 and CO producing states were tested at varying H_2 treatment temperatures, reaction temperatures and reactant partial pressures and it exhibited robust behavior despite being in conditions where significant H_2O concentration is produced. The results are shown in Figure 4.1-4.3 where it was observed that the CH_4 producing state was stable on short time scales (<4 hours) for all reaction conditions with CO_2:H_2 feed ratios <1. Furthermore, it was observed that the catalyst exhibited good stability in the CH_4 and CO producing states under reaction conditions consisting of 1%CO_2:1%H_2:98%He, 200 °C and a total flow rate of 100 sccm. The stability of the CH_4 producing state under the 1%CO_2:1%H_2:98%He feed conditions was also tested as a function of reaction temperature, see Figure 4.8. It was observed that at temperatures >275 °C, significant CO production begins to accompany CH_4 production, however this effect is well known to occur due to CO production being favored thermodynamically at higher temperature.(*23*)

Based on the good stability and lack of thermodynamic effects on selectivity, reaction conditions consisting of 1%CO_2:1%H_2:98%He, 200 °C and a total flow rate of 100 sccm were chosen to maximize catalyst stability and demonstrate the impact of 20CO_2:2H_2 treatment on the reaction selectivity in a kinetically controlled regime. The results in Figure 4.1-4.3 also demonstrate that the onset of a switch in selectivity from CH_4 to CO production occurs at long time scales under reaction conditions with CO_2:H_2 feed ratio of 1 and occurs more rapidly at feed ratios >1. We found that at reaction conditions of 20%CO_2:2%H_2:78%He and 250 °C, maximum changes in selectivity were consistently induced on a time scale of shorter than 4 hours. Thus, 20%CO_2:2%H_2:78%He and 250 °C for 4 hours was chosen as the treatment condition to induce the A-SMSI formation and switch in CO_2 reduction reaction selectivity.

Similar experiments were designed to examine the stability of the A-SMSI, CO producing, state. Because it was observed in Figure 4.1 and 4.3 that at long time scales, and 1:1 CO_2:H_2 feed ratios the catalyst ultimately favored existing in the CO producing state, we could ensure that the CO producing state was stable in the chosen standard reaction conditions, 1%CO_2:1%H_2:98%He, 200 °C. To identify where the A-SMSI, CO producing, state of the catalysts became unstable we formed the A-SMSI state by exposing Rh/TiO_2 catalysts to 20%CO_2:2%H_2:78%He and 250 °C for four hours followed by various treatments. In Figure 4.4, following A-SMSI formation on a 2% Rh/TiO_2 catalyst the catalyst was exposed to H_2 for 4 hours at increasing temperature. Following each H_2 treatment the reactivity of the catalyst was assayed at 1%CO_2:1%H_2:98%He, 200 °C. It was identified that the A-SMSI state was stable up to a H_2 treatment of 300 °C, where at 350

˚C and above, the catalyst returned to the original high CH_4 selectivity observed on the freshly reduced catalyst. The stability of the A-SMSI state was tested as a function of reaction temperature under typical reaction conditions, 1%CO_2:1%H_2:98%He, where high stability was found up to ~350 °C, Figure 4.7. The stability of the A-SMSI state was also tested as a function of CO_2 and H_2 partial pressure, with a constant CO_2:H_2 feed ratio of 1 and temperature of 200 °C, where it was found that CO was the predominant product until > 20%CO_2:20%H_2 reaction conditions, Figure 4.9 and Table 4.2. These results clearly show that the A-SMSI, CO producing, state was highly stable over a range of reactant partial pressures and reaction temperatures where significant amounts of H_2O were produced during the reaction.

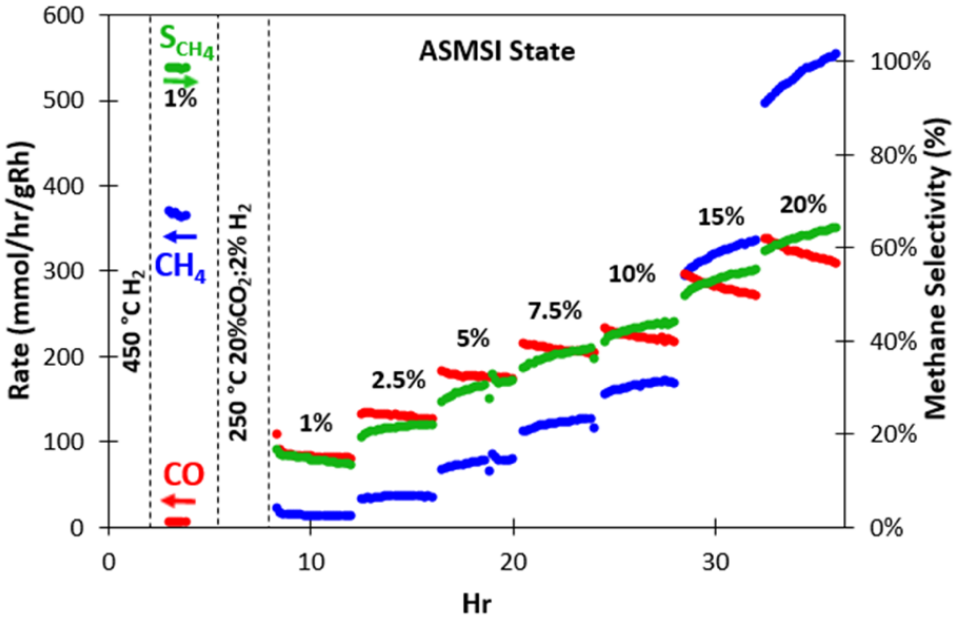

Figure 4.9 Effect of CO_2 and H_2 partial pressures on stability in A-SMSI state. Rate of CO/CH_4 formation and CH_4 selectivity on 2% Rh/TiO_2 measured at 1% CO_2, 1% H_2, balance He, 200 °C after reduction and then 20CO_2:2H_2 treatment, followed by reactivity measurements at increasing CO_2 and H_2 partial pressures (constant 1:1 CO_2:H_2 feed ratio with % partial pressure of each reactant annotated in the plot with balance He), and constant temperature (200 °C). We note that even at 20% CO_2:20%H_2, CH_4 selectivity did not return to the level of the initially reduced material.

Table 4.2
Partial pressure of reactant gases testing A-SMSI stability
*Conditions used for Fig 4.9

H_2 (sccm)	CO_2 (sccm)	He (sccm)	Total Flow	%CO_2 and H_2
1	1	98	100	1%
2.5	2.5	95	100	3%
5	5	90	100	5%
7.5	7.5	85	100	7.5%
10	10	80	100	10%
10	10	46.6	67	15%
10	10	30	50	20%

After being identified as the optimal treatment for switching the CH_4 selectivity, the influence of $20CO_2$:$2H_2$ treatment on CO_2 reduction selectivity was tested for various Rh weight loadings on TiO_2 (0.2-6%), see Fig. 4.10-4.12, and the results are summarized in Fig. 4.13. Consistently the $20CO_2$:$2H_2$ treatment induced a decrease in CH_4 production and increase in CO production, which was reversible upon re-reduction. Low CH_4 selectivity on lower Rh weight loading catalysts following reduction was due to high concentrations of CO-producing isolated Rh atom active sites. The largest selectivity changes were observed for higher Rh weight loadings that predominantly consist of Rh nanoparticle active sites, suggesting that $20CO_2$:$2H_2$ treatment modified the reactivity of Rh nanoparticles. The negligible change in CO production on 0.2% Rh/TiO_2, Fig. 4.10, where nearly all catalytic sites are isolated Rh atoms, indicates that the $20CO_2$:$2H_2$ treatment has little effect on the reactivity of isolated Rh atoms. The production rate of ethane and propane (C_2+ products) was also suppressed by the $20CO_2$:$2H_2$ treatment, as shown for 2% Rh/TiO_2 in Fig. 4.14, which is consistent with prior work, where catalysts exhibiting high CH_4 selectivity typically produce more C_2+ products.[30] The results in Fig. 4.5, 4.13, 4.14 demonstrate that the reactivity of Rh/TiO_2 for the CO_2 reduction reaction is dynamically

tunable via $20CO_2{:}2H_2$ and H_2 treatments, where Rh nanoparticle reactivity following $20CO_2{:}2H_2$ treatment is consistent with the catalytic behavior of more noble (Pt, Pd, Cu) metal catalysts.[31–33]

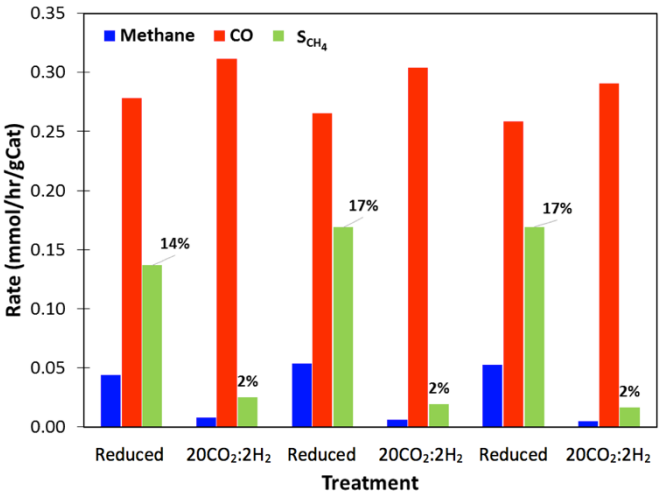

Fig. 4.10 Catalyst performance after cycling with H_2 and $20CO_2{:}H_2$ treatments 0.2%RhThe rate of CO and CH_4 production, and CH_4 selectivity on 0.2% Rh/TiO_2 measured at 200 °C 1 sccm CO_2, 1 sccm H_2, 98 sccm He following sequential treatments of 4 hours of 20 sccm H_2 at 450 °C and 4 hours of $20CO_2{:}H_2$ treatment at 250 °C. Reported rate and selectivity represent an average of 5 GC injections 200 °C 1 sccm CO_2, 1 sccm H_2, 98 sccm He following each treatment.

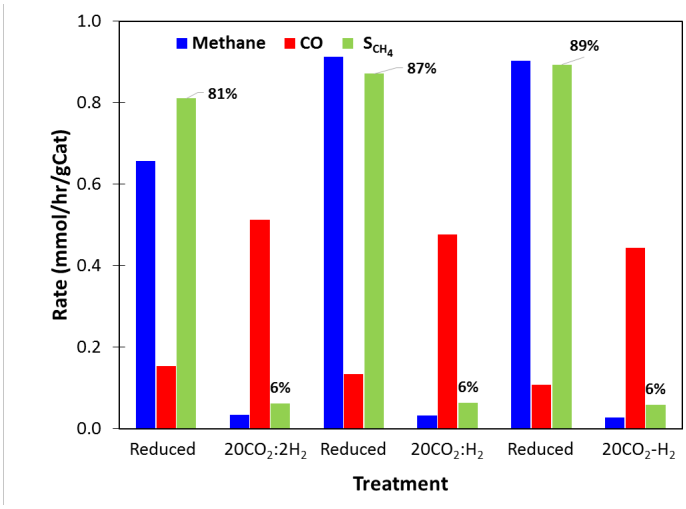

Fig. 4.11 Catalyst performance after cycling with H_2 and $20CO_2:H_2$ treatments 2%Rh

The rate of CO and CH_4 production, and CH_4 selectivity on 2% Rh/TiO_2 measured at 200 °C 1 sccm CO_2, 1 sccm H_2, 98 sccm He following sequential treatments of 4 hours of 20 sccm H_2 at 450 °C and 4 hours of $20CO_2:H_2$ treatment at 250 °C. Reported rate and selectivity represent an average of 5 GC injections 200 °C 1 sccm CO_2, 1 sccm H_2, 98 sccm He following each treatment

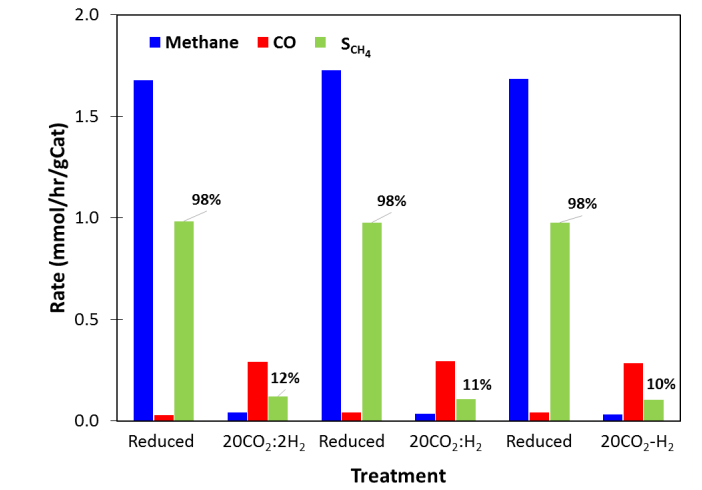

Fig. 4.12 Catalyst performance after cycling with H_2 and $20CO_2:H_2$ treatments 6%Rh

The rate of CO and CH_4 production, and CH_4 selectivity on 6% Rh/TiO_2 measured at 200 °C 1 sccm CO_2, 1 sccm H_2, 98 sccm He following sequential treatments of 4 hours of 20 sccm H_2 at 450 °C and 4 hours of $20CO_2:H_2$ treatment at 250 °C. Reported rate and selectivity represent an average of 5 GC injections 200 °C 1 sccm CO_2, 1 sccm H_2, 98 sccm He following each treatment.

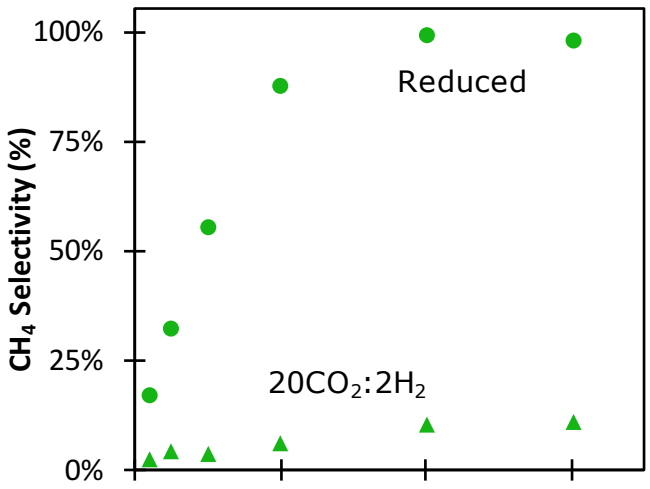

Figure 4.13 (B) Effect of $20CO_2{:}2H_2$ treatment on CH_4 selectivity measured at 200 °C with a feed composition of 1% CO_2, 1% H_2, 98% He (100 sccm total) as a function of Rh weight loading (%) on TiO_2.

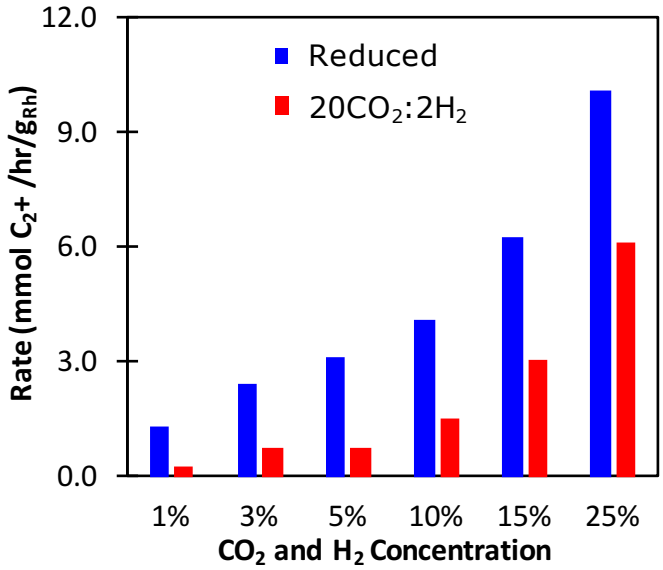

Figure 4.14(c) Effect of $20CO_2{:}2H_2$ treatment on Ethane + Propane (C_2+) production rate over 2% Rh/TiO_2 catalyst as a function of feed composition with equimolar CO_2 and H_2 feed and a balance of He.

4.4.2 Feasibility of Disintegration Mechanism with In-Situ XAS and Ex- Situ HR-STEM

Considering that isolated Rh atoms are selective for CO production and Rh nanoparticles are selective for CH_4 production, the cause of the dynamic decrease in CH_4 could be hypothesized that $20CO_2$:$2H_2$ treatment disintegrates Rh nanoparticles to form isolated Rh atoms on the TiO_2 surface.[34,35] *In-situ* X-ray absorption spectroscopy (XAS) following the Rh K-edge on a 2% Rh/TiO_2 catalyst during $20CO_2$:$2H_2$ treatment was used to analyze the possibility of Rh structural transformations. No significant difference between the reduced catalyst and following $20CO_2$:$2H_2$ treatment was observed, with a nearly constant particle size of ~1.3 nm based on Rh-Rh coordination number (7.7 ± 0.6), Fig 4.15, 4.16. XAS results were consistent with *ex-situ* scanning transmission electron micrographs (STEM) of 2% Rh/TiO_2 catalysts following reduction and $20CO_2$:$2H_2$ treatment that showed no evidence of Rh structural changes, Fig. 4.15-4.17. Based on the lack of structural changes in Rh observed by XAS and STEM and disproportionate changes in the rate of CH_4 and CO production (Fig. 4.1,4.5), the switch in reactivity induced by $20CO_2$:$2H_2$ treatment is attributed to modified Rh-TiO_2 interactions.

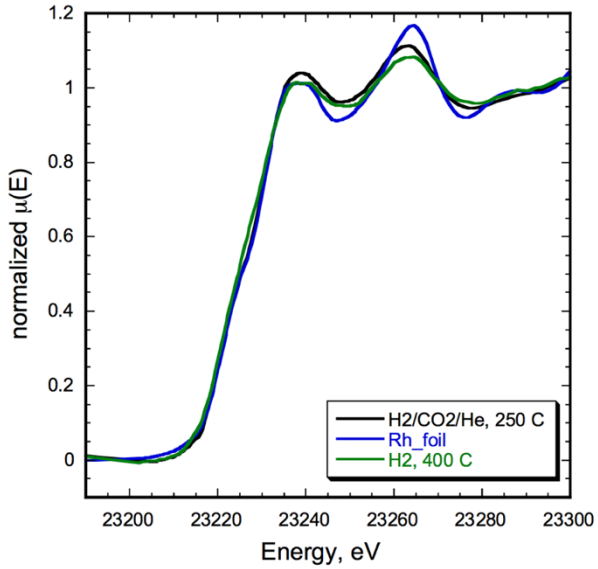

Fig. 4.15 *In-situ* XANES analysis of 2% Rh/TiO_2 Normalized *in situ* XANES spectra of Rh K-edge for Rh foil (blue) and 2%Rh/TiO_2 sample treated in 400 °C H_2 flow (green) and 250 °C 20%CO_2/2%H_2/78% He conditions (black). Similar spectra for both H_2 and 20CO_2:2H_2 treated samples show no significant change in Rh structure between the two treatments. Difference between the 2% Rh/TiO_2 samples and Rh foil around 23,265 eV peak shows a difference in Rh coordination number indicating the TiO_2-supported particles are small.

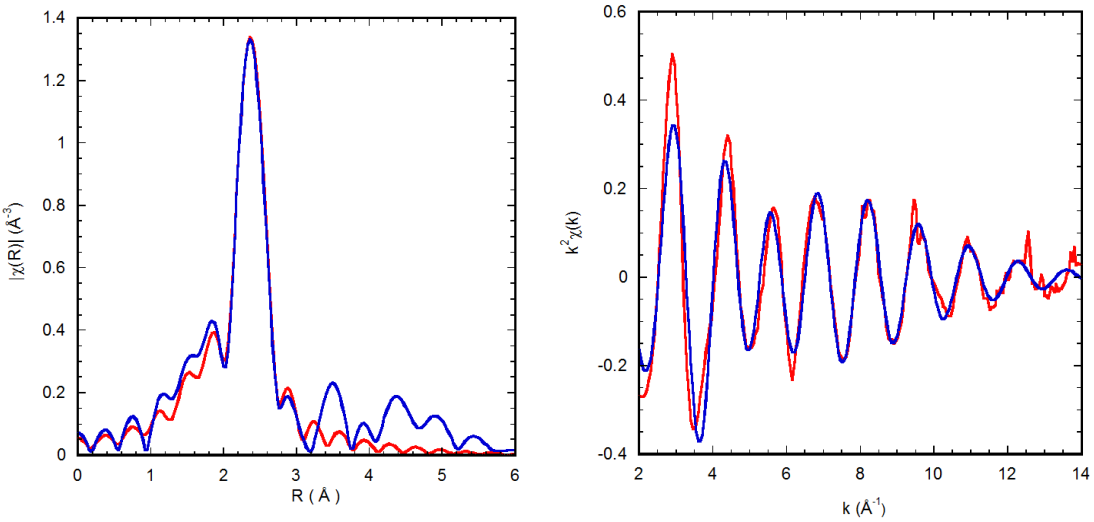

Fig. 4.16 In-Situ EXAFS Analysis of 2% Rh/TiO_2

In-situ A) Fourier transform magnitude (R-space) and B) radial distance (k-space) spectra of the 2% Rh/TiO_2 catalyst at 250 °C in a 20%CO_2/2%H_2/78% He gas mixture; raw EXAFS data (red) and first shell fit (blue line). The average coordination number (ACN) obtained was 7.7 ± 0.6 corresponding to a particle of ~55 atoms with a 1.3 nm diameter, in good agreement with STEM spectra shown in figures 4.17, 4.24, 4.25.

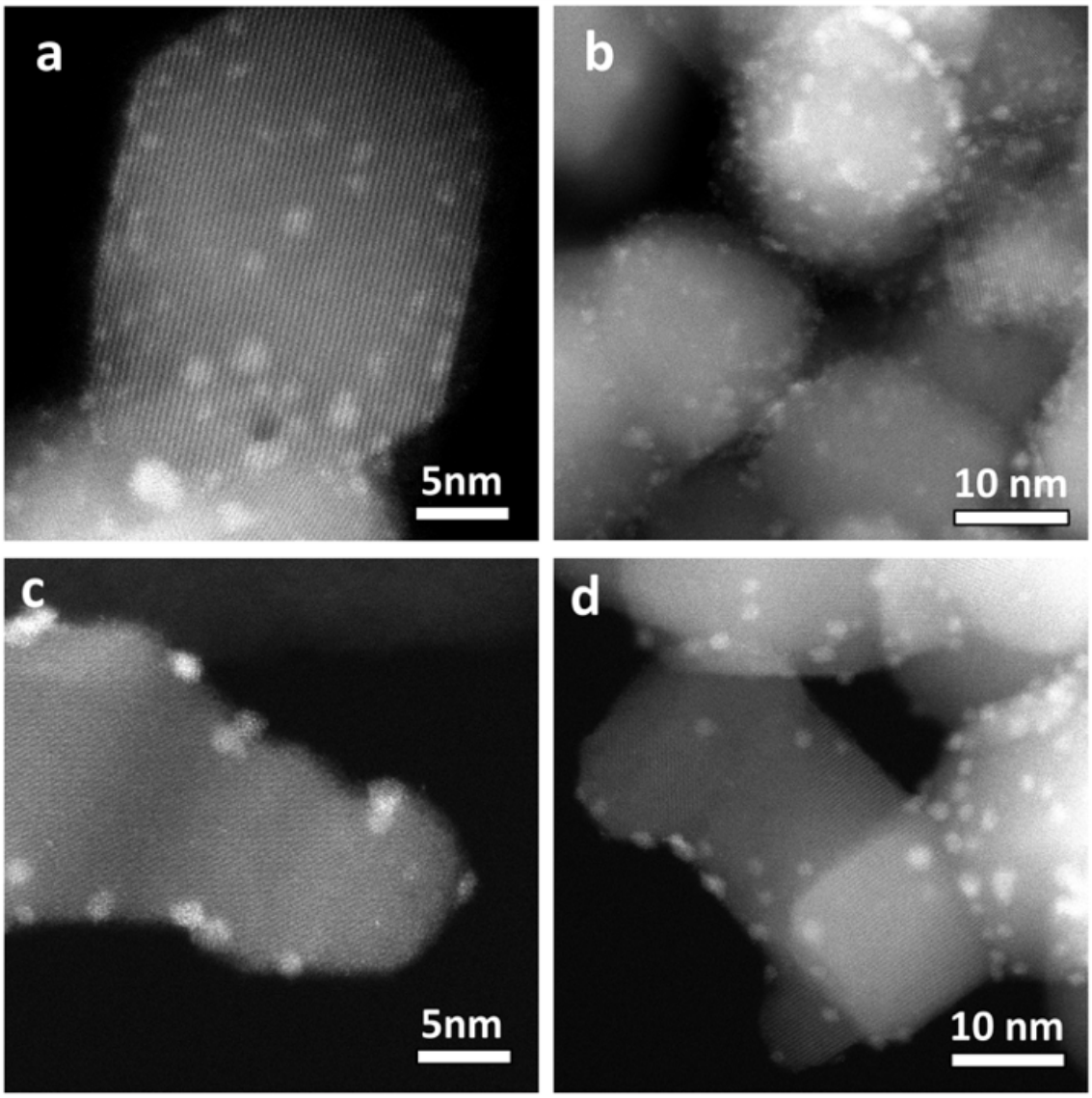

Fig. 4.17 Ex-Situ High resolution transmission electron micrographs of 2%Rh/TiO_2 (a,b) following reduction at 450 °C in H_2 for 1 hour and (c,d) following $20CO_2$:$2H_2$ treatment. No obvious differences in particle size or density were observed, suggesting no Rh nanoparticle disintegration to isolated Rh atoms.

4.4.3 In-Situ DRIFTS: Investigating Transformation at the Catalyst Surface

To test the idea that this catalytic transformation induced by $20CO_2$:$2H_2$ treatment was due to modified Rh-TiO_2 interactions, *In-situ* diffuse reflectance infrared Fourier transform spectroscopy (DRIFTS) was used to examine the effect of $20CO_2$:$2H_2$ treatment on the species adsorbed to Rh and TiO_2 under reaction conditions. Fig. 4.18(A) shows *in-situ* DRIFT spectra acquired from 2% Rh/TiO_2 under reaction conditions (1%CO_2:1%H_2:98%He and 200 $^{\circ}$C) following reduction, $20CO_2$:$2H_2$ treatment, and re-reduction; essentially identical to Fig. 4.5. Under reaction conditions, the DRIFT spectrum of the reduced catalyst shows features associated with CO linearly bound to Rh top (2046 cm^{-1}) and bridge (1880 cm^{-1}) sites and low adsorbate coverage on TiO_2, aside from H_2O (1620 cm^{-1}), in agreement with previous reports.[36,37] Following $20CO_2$:$2H_2$ treatment, the switch in CO_2 reduction selectivity was correlated with a ~50 cm^{-1} red-shift in the frequency of linear and bridge bound CO stretching modes, and a 2-fold decrease in the integrated area of the linearly bound CO stretch. The red-shift in frequency and decreased intensity of the CO stretches could be explained by a decrease in CO coverage on the Rh surface,[38] or the physical blocking of Rh sites coupled with the polarization of CO bonds, induced by charge transfer to Rh,[39] a local electric field induced Stark effect,[40] or coordination of CO across a metal-support interface.[23] $20CO_2$:$2H_2$ treatment also introduced high coverage of formate (HCO_2, 2973, 2923, 2853, 1531, and 1351 cm^{-1}) and a bicarbonate-like species (HCO_3, 1444 cm^{-1}) on the TiO_2 surface,[41] which were only observed under reaction

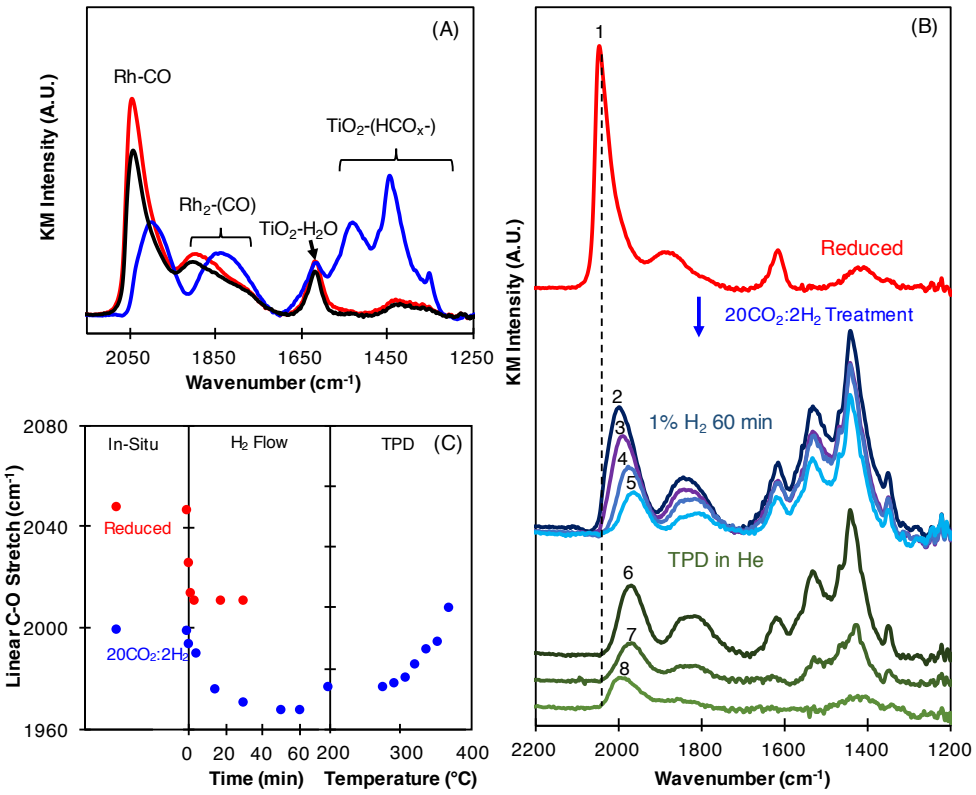

Figure. 4.18 DRIFTS analysis of selectivity switch. (An) In-situ DRIFT spectra collected from 2% Rh/TiO2 at reaction conditions (180 °C, 1% CO2, 1% H2, 98% He), for reduced (red), 20CO2:2H2 treated (blue) and re-reduced (black) catalyst. (B) DRIFT spectra of 2% Rh/TiO2 under reaction conditions after reduction (spectrum 1), after 20CO2:2H2 treatment (spectrum 2), CO_2 flow removed (only 1% H2) for 5, 15, 60 minutes (spectra 3-5). Spectra (6-8) were collected during TPD in pure He at 213, 312, and 370 °C, respectively, immediately following collection of spectrum (5). Vertical dotted line represents the frequency of the CO stretch on reduced 2% Rh catalyst under reaction conditions. (C) Peak positions of the linear CO stretching frequency during the experiments in Fig. 2(B) and S18.

conditions following the $20CO_2$:$2H_2$ treatment. Re-reduction of the catalyst regenerated spectral characteristics of the freshly reduced catalyst, consistent with regenerated reactivity shown in Fig. 4.5.

To identify whether the ~50 cm^{-1} red-shift and decreased intensity of the CO stretching modes were simply caused by a decrease in CO coverage on Rh, CO_2 was removed from the reactant stream leaving H_2 to react with adsorbates. The decrease in the

Rh-CO stretch intensity as a result of removing CO_2 from the reactant stream suggests that Rh was still the active site in the reaction, as the intermediate species should react away before spectator species. Following removal of CO_2 from the reactant stream, CO stretches red-shifted ~35-40 cm^{-1} as CO coverage decreased on both the reduced and $20CO_2$:$2H_2$ treated catalysts, (spectra 1-4 on Fig. 4.19 and spectra 2-5 on Fig. 4.18(B). This is shown quantitatively in Fig. 4.18(C), where both the reduced and $2OCO_2$:$2H_2$ treated catalysts exhibit a similar decrease in CO stretching frequency in H_2 flow. The coverage dependent red-shift in CO stretching frequency of 35-40 cm^{-1} (spectra 1-4 on Fig. 4.19 and spectra 2-5 on Fig. 4.18(B)) is consistent with the effect of reduced dipole coupling on nanoparticle catalyst surfaces,[38] indicating that the $2OCO_2$:$2H_2$ treatment induced 50 cm^{-1} red-shift (Fig. 4.18(A)) in CO stretching frequency was not caused by a change in local CO coverage. This demonstrates that the 50 cm^{-1} shift in CO stretching frequency under reaction conditions, driven by $20CO_2$:$2H_2$ treatment, was related to modified Rh-TiO_2 interactions that polarized CO bound to Rh. The polarization of CO bonds is consistent with high CO selectivity, as this would decrease CO binding energy and cause Rh to behave similarly to more noble metal catalysts.[31–33] The origin of the 50 cm^{-1} shift in CO stretching frequency was further probed by executing a temperature programmed desorption (TPD) in He, following the coverage dependent experiment, (spectra 6-8 in Fig. 4.18(B)). HCO_x species desorbed from TiO_2 above ~300 °C with a simultaneous blue-shift in frequency of the remaining linearly bound CO by ~35 cm^{-1} to ~1996 cm^{-1}. As the HCO_x species desorbed above 300 ˚C, the CO stretching frequency returned to the frequency observed at low

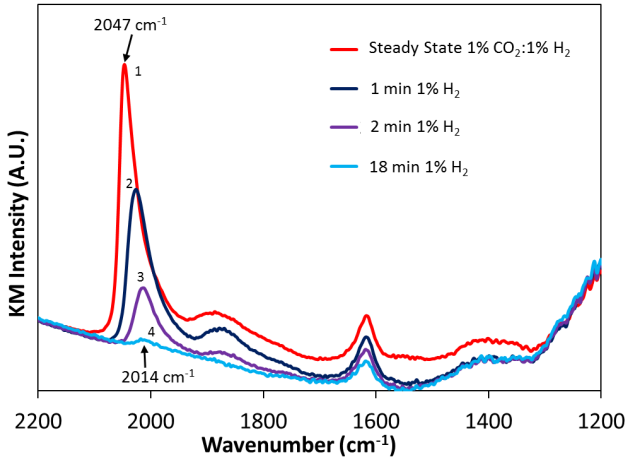

Fig. 4.19 *In-Situ* DRIFT spectrum of 2% Rh/TiO_2 after reduction, under steady state reaction conditions of 200 °C, 1% CO_2, 1%H_2, 100 sccm total flow (Red). The CO_2 feed was then removed leaving a stream of 1% H_2/He with the dark blue, purple, and light blue spectra taken at 1, 2, and 18 minutes, respectively, after removing CO_2. The CO stretch on Rh red-shifted 33 cm^{-1} with coverage, supporting the hypothesis that an additional mechanism to coverage effects was needed to explain the 80 cm^{-1} red-shift observed in fig 4.18b.

coverage on the reduced catalyst, Fig. 4.18(C). Catalyst performance was tested after HCO_x species were desorbed from the $20CO_2$:H_2 treated sample (He flow at 450 °C for 4 hours) and the production rates of CH_4 and CO under reaction conditions were restored to the behavior of the original reduced catalyst state, Fig 4.20. Correlation between the removal of HCO_x species from TiO_2 and blue-shift in CO stretching frequency, as well as the return of the reduced catalyst reactivity, demonstrates that modified reactivity induced by $20CO_2$:$2H_2$ treatment is mediated by interactions between HCO_x and the support.

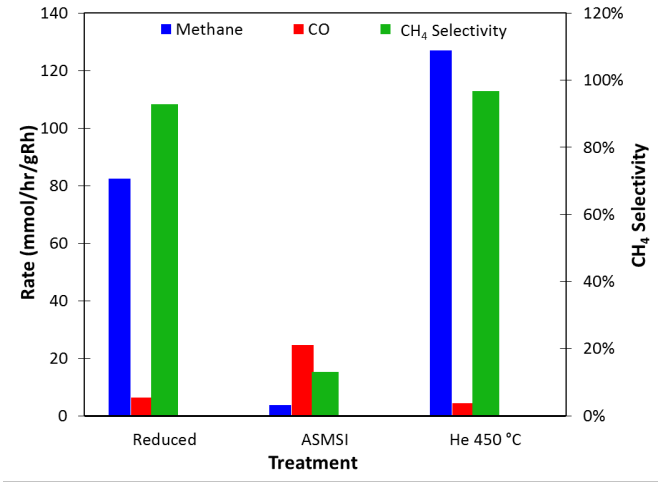

Fig. 4.20 Investigating reversibility of A-SMSI state at elevated temperature in He
Rate of CO/CH_4 formation and CH_4 selectivity after reduction, $20CO_2$:H_2 treatment, and 4 hours of pure He at 450 °C on a 2%Rh/TiO2 catalyst all under reaction conditions at 200 °C 1 sccm CO2, 1 sccm H2, 98 sccm He. The restoration of the catalytic performance to the reduced state indicates that the A-SMSI transformation is mediated by HCOx adsorbates on the support.

The decreased intensity of the CO stretching modes on Rh under reaction conditions following $20CO_2$:$2H_2$ treatment and resulting influence of HCO_x functionalized TiO_2 on all remaining Rh-CO bonds, both in terms of reactivity and spectroscopically, are consistent with SMSI overlayer effects.[19,23] However, the traditional SMSI state for Rh on TiO_2 forms at higher temperature (500 °C) and more reducing conditions (pure H_2) than the $20CO_2$:$2H_2$ treatment and recedes off the metal in the moist atmosphere of CO_2 reduction, resulting in very little influence on reactivity.[21] Furthermore, formation of the traditional SMSI layer for Rh/TiO_2 and analysis in dry atmospheres has shown that the encapsulation layer only blocks available Rh sites for CO adsorption, but does not induce a significant shift in stretching frequency of CO adsorbed at uncovered Rh sites, in contrast to the observations in Fig. 4.18(A).[42]

4.4.4 Formic Acid-Induced Reduction Experiments

The lack of similarity between formation and destruction of the the $20CO_2$:$2H_2$ induced phase and traditional SMSI suggests that traditional SMSI is not being observed in this work. However, we believed that in order to affect all Rh-CO bonds equally, as shown in the complete Rh-CO frequency change, that some type of TiO_x overlayer may have still been forming. To form an overlayer from a reducible oxide, first the oxide must be reduced and in this case, it must be reduced in an environment that is not simply H_2. Interestingly, analysis of formic acid decomposition on TiO_2 has shown that at high formic acid coverages and temperatures greater than ~100 °C, oxygen vacancies at the TiO_2 surface form via the formation of H_2O from neighboring bridge bound hydroxyl groups, leaving a HCO_2 covered, disordered, and reduced TiO_{2-x} surface.[43–45] Formic acid induced oxygen vacancy formation in TiO_2 occurs under conditions that resemble conditions we observed following $20CO_2$:$2H_2$ treatment, where TiO_2 is covered by HCO_x. To compare formic acid induced TiO_2 reduction and $20CO_2$:$2H_2$ treatment induced changes in Rh reactivity, the temperature range at which the $20CO_2$:$2H_2$ treatment induced a switch in CO_2 reduction selectivity was identified, Fig. 4.21(A). The temperature range (~150-300 °C) agrees with that of formic acid induced TiO_2 reduction, where TiO_2 reduction is limited at low temperature (~100 °C) by H_2O desorption kinetics and at high temperature (~300 °C) by formate desorption. To further demonstrate a relationship between formic acid induced TiO_2 reduction and $20CO_2$:$2H_2$ treatment induced modification of Rh/TiO_2 reactivity, a 2% Rh/TiO_2 catalyst was treated in formic acid at 250 °C for 4 hours, after which the reactivity was evaluated. Fig. 4.21(B) shows that similar to the $20CO_2$:$2H_2$

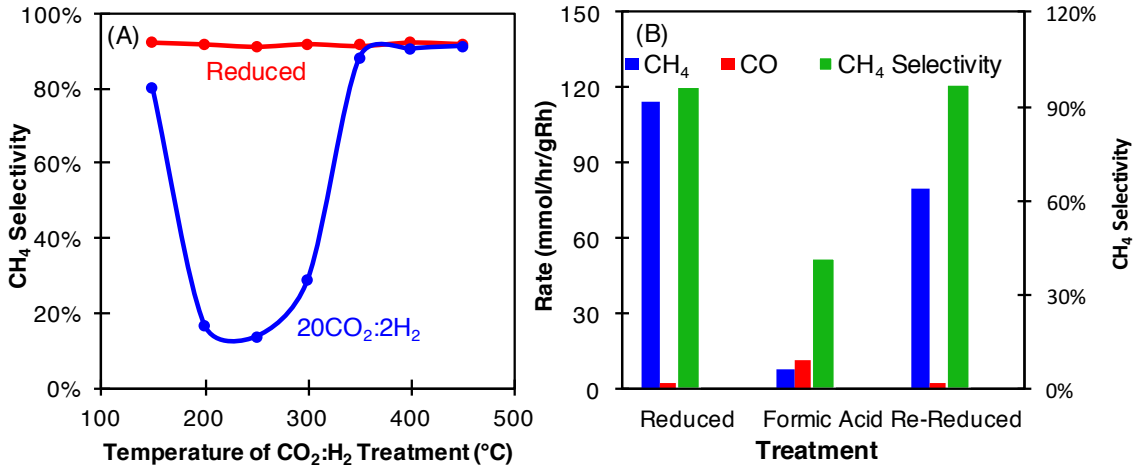

Fig. 4.21 Identifying the mechanism of A-SMSI formation with Formic Acid.

(A) CH_4 selectivity on 2% Rh/TiO_2 as a function of $20CO_2$:$2H_2$ treatment temperature shown in blue measured at 200 °C with a feed composition of 1% CO_2, 1% H_2, 98% He (100 sccm total). The catalyst was re-reduced after each $20CO_2$:$2H_2$ treatment, and the reactivity under identical reaction conditions is shown in red. The experiment was run using identical protocol as in Fig. 4.6, but with increasing temperature during the $20CO_2$:$2H_2$ treatment for each cycle. See protocol in 4.3.3 for details. (B) Rate of CH_4 and CO production and CH_4 selectivity after reduction, formic acid treatment, and re-reduction on a 2%Rh/TiO_2 catalyst all measured under reaction conditions at (200 °C, 1% CO_2, 1% H_2, 98% He, 100 sccm total). Formic acid treatment was 25 sccm pure He bubbled through formic acid at room temperature for 4 hours with a catalyst bed temperature of 250 °C.

treatment, formic acid treatment of 2% Rh/TiO_2 decreased the rate of CH_4 production by 14-fold and increased the rate of CO production by 5-fold compared to the reduced catalyst, which was reversible upon re-reduction. Both of these analyses support the idea that the TiO_2 support could potentially be undergoing reduction and therefore some type of overlayer formation in the $20CO_2$:$2H_2$ treatment conditions.

4.4.5 In-Situ STEM and EELS: Physical and chemical nature of overlayer formation

Similarity between the influence of $20CO_2$:$2H_2$ and formic acid treatments on the reactivity of Rh/TiO_2 catalysts suggests the existence of an adsorbate-mediated SMSI (A-SMSI) state where high coverage of HCO_x induces the formation of oxygen vacancies at the TiO_2 surface, thereby causing migration of the support onto Rh. However, it could be

imagined that charge donation from HCO_x functionalized, reduced TiO_2 into Rh, without migration onto Rh, is causing the modified reactivity. To differentiate HCO_x-induced charge transfer from TiO_2 into Rh without support migration onto the metal from localized interactions at an Rh:TiO_x-HCO_x overlayer interface, a 6% Rh/TiO_2 catalyst was sintered through treatment at 800 ˚C in N_2 for 3 hours, increasing the Rh particle sizes from 1-3 nm to 10-50 nm in diameter, Fig. 4.22. The sintered catalyst was evaluated for reactivity after reduction and $20CO_2$:$2H_2$ treatment, where CH_4 selectivity decreased from 97% following reduction, to 4% following $20CO_2$:$2H_2$ treatment, Fig. 4.22. It has been shown that charge transfer between oxide supports and metal particles, where the metal:support interface is strictly at one metal facet without overlayer formation, is maximized at ~1-2 nm metal particle diameter, and that above this size the charge transferred per metal atom is severely diminished.[12] The almost identical influence of $20CO_2$:$2H_2$ treatment on the sintered and un-sintered 6% Rh/TiO_2, with large differences in Rh particle sizes, strongly supports the mechanism of HCO_x mediated migration of TiO_x onto Rh, because the charge transfer mechanism without overlayer formation would have been suppressed by the increased particle size in the sintered catalyst. Thus, interaction between HCO_x functionalized TiO_2 and the Rh active sites must be locally occurring at a metal:overlayer interface as a result of coordination between the overlayer and Rh surface.

To directly visualize the $20CO_2$:$2H_2$-induced TiO_2 structural transformation, *in-situ* STEM experiments were executed during reduction and $20CO_2$:$2H_2$ treatment of the sintered 6% Rh/TiO_2 catalyst. Following treatment at 550 ˚C in H_2, conditions known to form the traditional SMSI state, a crystalline bilayer of TiO_x quickly formed

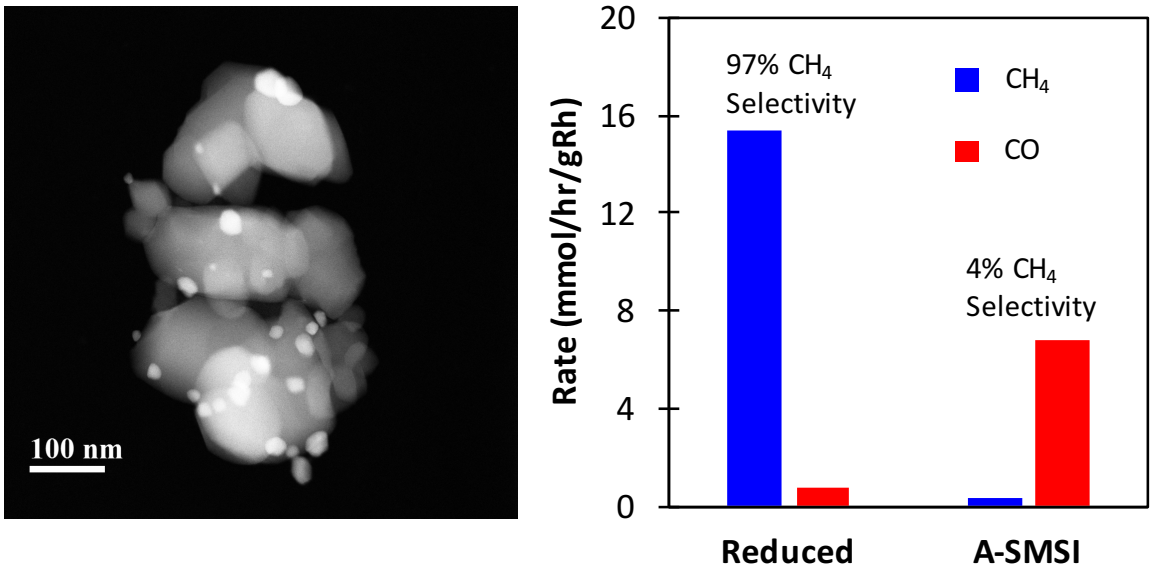

Fig. 4.22 STEM micrograph and reactivity of large Rh NPs via sintering. STEM micrograph of 6%Rh/TiO2 after being sintered in N2 at 800 ˚C for 3 hours as described in section 3.6.1. Treatment increased the grain size of TiO2 particles from 20-30 nm to 100-200 nm and increased Rh particle size from 1-3nm to 10-50nm. B) Rate of CO/CH4 formation and CH4 selectivity on sintered 6%Rh/TiO2 after reduction and 20CO2:2H2 treatment (A-SMSI state) under reaction conditions at 200 °C, 1 sccm CO2, 1 sccm H2, 98 sccm He. The significant decrease in methane selectivity from the 20CO2:2H2 treatment (A-SMSI state) for the larger Rh particle size was in direct agreement with the smaller Rh particle size data shown in Figure 4.12. This similarity across a large particle size range (1-50nm) indicates the phenomena affecting the catalytic selectivity must be localized to the surface of the Rh, as the through support charge transfer mechanism would have been significantly suppressed by the increased particle size in the sintered catalyst.

as a conformal coating on large crystalline Rh particles, where Ti is exclusively in the 3+ oxidation state, Fig. 4.23(A).[26,46–48] In contrast, following $20CO_2:2H_2$ treatment for 3 hours of a freshly sintered catalyst, an amorphous overlayer on Rh was observed to form, Fig. 4.23(B),4.24, 4.25. *In-situ* Electron energy loss spectroscopy (EELS) measurements with a 1.0-1.5 Å spot size focused at various locations on the overlayer

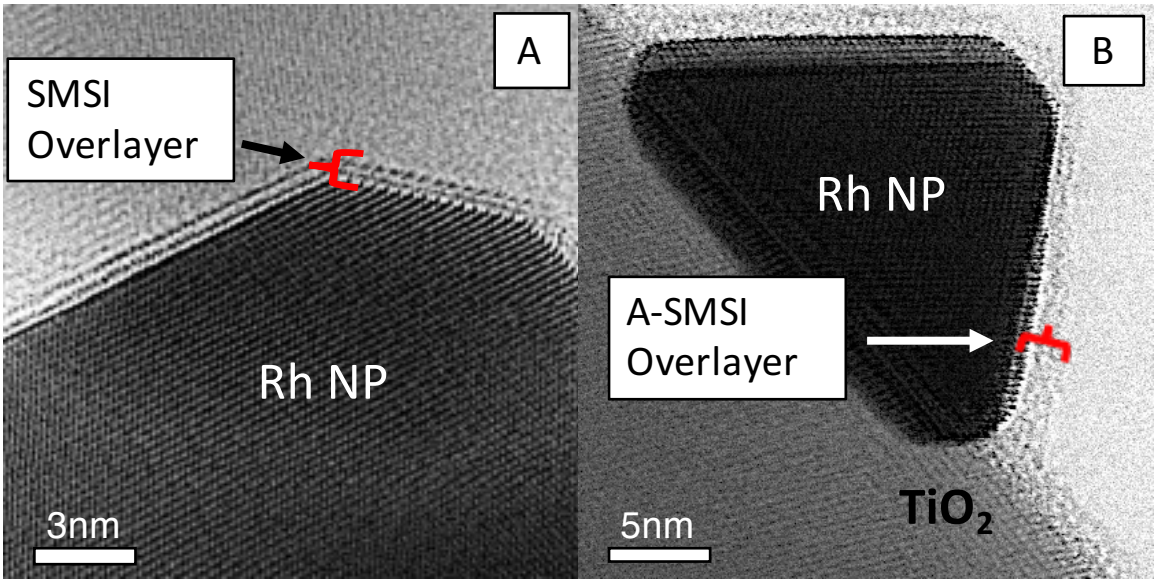

Fig. 4.23 Visualizing the SMSI and A-SMSI States. *In-Situ* HRTEM micrographs of 6%Rh/TiO_2 sintered at 800 ˚C for 3hrs to induce sintering and then treated with: a) 5%H_2/N_2 at 550 ˚C for 10 minutes inducing the formation of a TiO_x SMSI crystalline bilayer overlayer on surface of a Rh NP b) 20CO_2:2H_2 at 250 ˚C for 4 hours causing the formation of an amorphous A-SMSI overlayer on surface of Rh NP.

directly proved that Ti was present in the amorphous overlayer formed from 20CO_2:2H_2 treatment, Fig. 4.26. Ti in the amorphous overlayer was found to exist in a combination of ~30% 3+ and 70% 4+ oxidation states. The *in-situ* STEM and EELS analyses of 20CO_2:2H_2 treated Rh/TiO_2 catalysts conclusively demonstrate the existence of an A-SMSI overlayer on Rh. Differences in Ti oxidation state for the traditional SMSI and A-SMSI overlayers are hypothesized to be due the presence of HCO_x in the A-SMSI overlayer and related to the unique reactivity and stability of the A-SMSI overlayer in humid CO_2 reduction conditions.

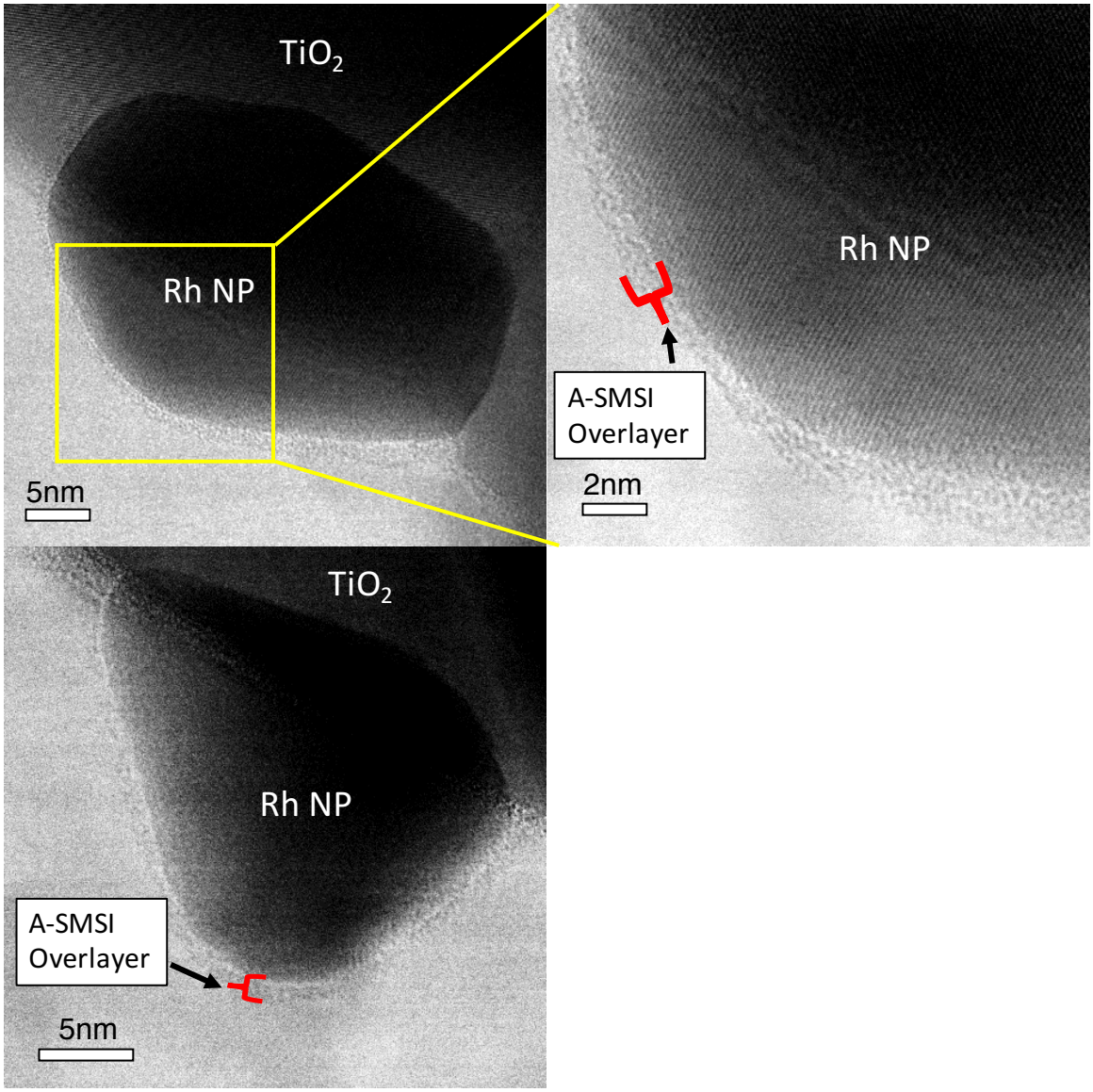

Fig. 4.24 Additional micrographs of A-SMSI overlayer formation in A-SMSI state

In-Situ STEM analysis of sintered 6% $Rh/TiOx_2$ treated at $20CO_2$:$2H_2$ conditions, and 250 ˚C for 4 hours. An amorphous A-SMSI overlayer is observed on the Rh nanoparticles (NP) denoted by the red bracket. These micrographs, along, with Figure 4.23(B) suggest that treating a Rh/TiO_2 with the $20CO_2$:$2H_2$ treatment reduces the TiO_2 support, causing migration onto Rh and formation of an overlayer covering the Rh NP's via a different mechanism than the typical high temperature H_2 induced SMSI.

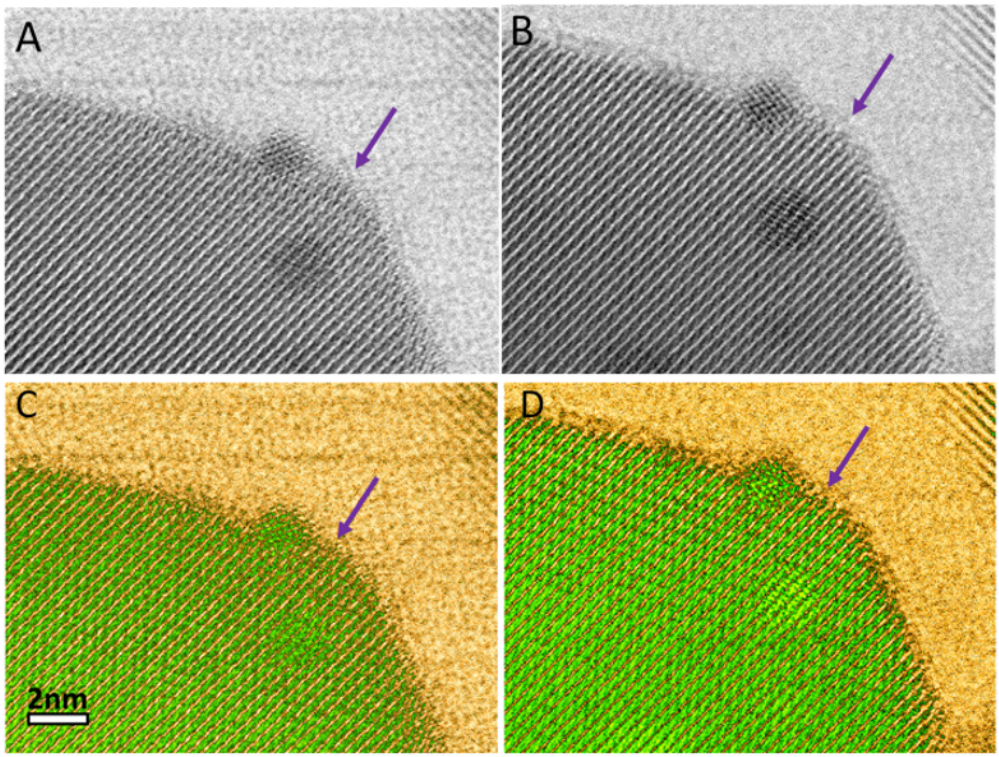

Fig. 4.25 *In-situ* STEM bright field micrographs of 2%Rh/TiO_2 . A) after 1 hour of H_2 reduction and B) 3 hours of $20CO_2$:$2H_2$ treatment. C,D) are A,B with false coloring to emphasize the A-SMSI overlayer. The formation of the comprehensive low-contrast overlayer is pointed out by the arrows in B and D and lack thereof in A and C.

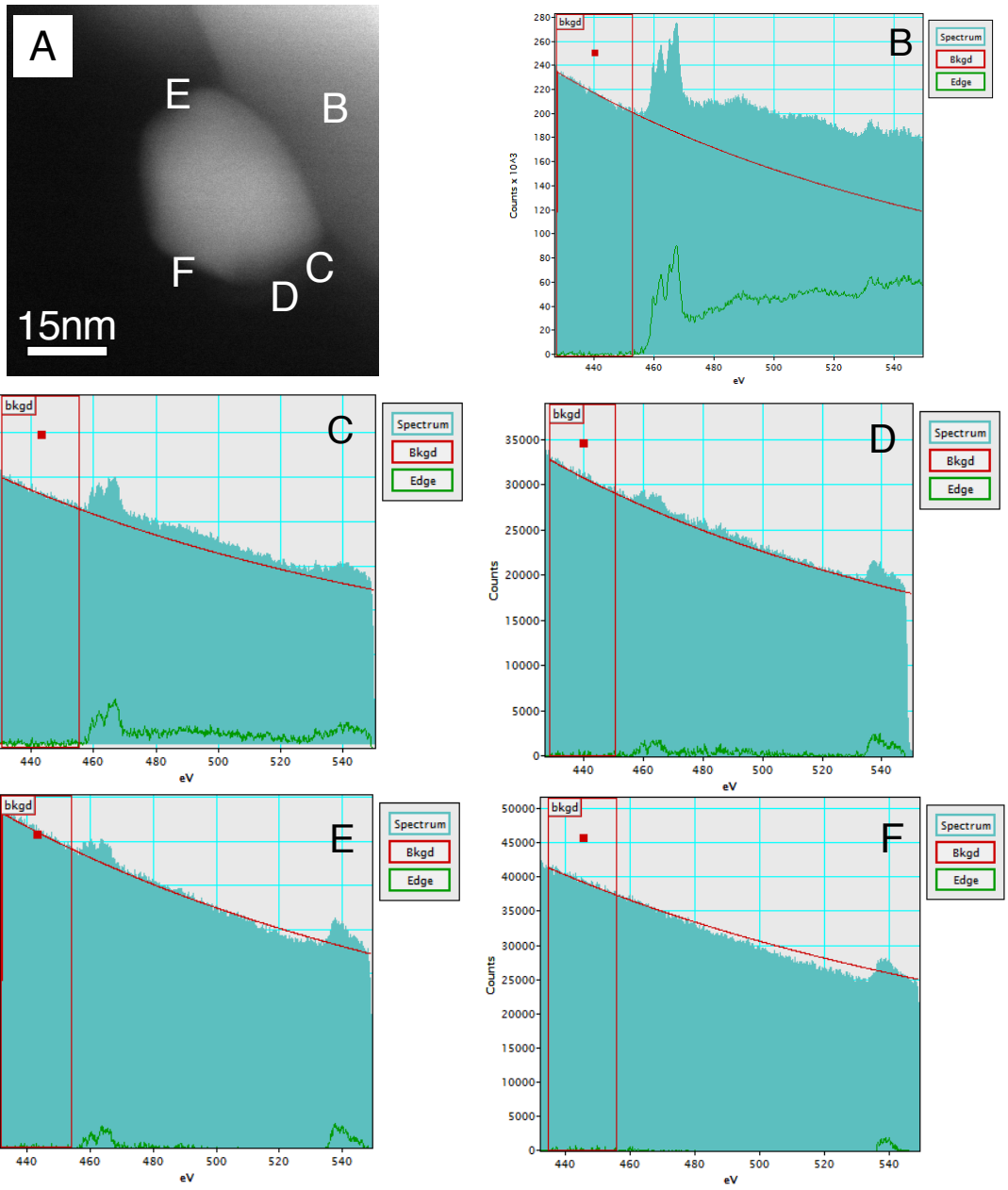
A
E
B
F
D
C
15nm
B
C
D
E
F
bkgd
Spectrum
Bkgd
Edge
Counts x 10^3
Counts
eV

Figure. 4.26 EELS analysis of A-SMSI overlayer. An) *In-situ* STEM dark field micrograph of (800 ˚C-sintered) 6% Rh/TiO_2 sample, after 250 ˚C $20CO_2$:$2H_2$ conditions for 4 hours. This micrograph serves as a map for EELS analysis with the letters (B-F) identifying the position of collected EELS spectra in (B-F). The EELS spot size is 1-1.5 Angstroms. B) Ti L edge showing Ti^{4+} in the TiO_2 support. C) Ti present on the shoulder of the particle. Multiple Linear Least Squares (MLLS) fitting based on standard spectra from $SrTiO_3$ and $LaTiO_3$ indicated that approximately 30% of the Ti was Ti^{3+} and 70% was Ti^{4+}. There was a Ti L edge also found on spots D and E, but not on F. The particle may have been partially covered or the concentration of Ti on the top of the particle (F) may have been below the detection limit of experimental configuration. Note: the sample was enclosed in two pieces of membrane with a total thickness of 80nm, likely attenuating the EELS signal.

4.4.6 Relating SMSI and A-SMSI Behavior

Since the traditional SMSI state initiates via support reduction and we hypothesized that the A-SMSI state initiates via support reduction, from the formic acid induced reduction experiments in 4.4.4, it was hypothesized that supports known to form SMSI encapsulation layers would also form A-SMSI encapsulation layers. Fig. 4.27(A,B) show CH_4 and CO production rates, respectively, following reduction and $20CO_2$:$2H_2$ treatment of 2%Rh on TiO_2, Nb_2O_5, CeO_2 and Al_2O_3, see Fig. 4.28. No significant change in CH_4 or CO production rates was observed on Al_2O_3 and CeO_2 supported Rh, as Al_2O_3, an irreducible support, does not exhibit SMSI behavior and CeO_2 only exhibits SMSI behavior under extremely harsh conditions.[21,22] Rh/Nb_2O_5 responded to $20CO_2$:$2H_2$ treatment similarly to Rh/TiO_2, exhibiting suppressed CH_4 production and increased CO production, which agrees with the known similar SMSI behavior of Nb_2O_5 and TiO_2.

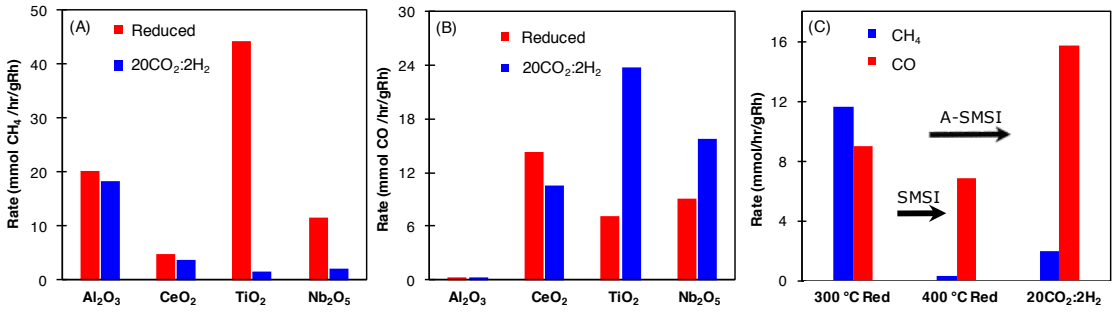

Fig. 4.27 Relating SMSI and A-SMSI behavior.
(A) CH_4 and (B) CO production rate on 2% Rh on various supports following reduction and $20CO_2$:$2H_2$ treatment under standard reaction conditions (200 °C, 1% CO_2, 1% H_2, 98% He). (C) Rate of CH_4 and CO production on 2% Rh/Nb_2O_5 after 300 °C reduction, 400 °C reduction and 300 °C reduction followed by $20CO_2$:$2H_2$ treatment.

In contrast to TiO_2, Nb_2O_5 SMSI overlayers on Rh formed due to high temperature H_2 treatment are stable during CO_2 reduction reaction environment, thus rendering metal

nanoparticles inactive.[20] The stable SMSI overlayer on Nb_2O_5 enables direct comparison of the effects of SMSI and A-SMSI on CO_2 reduction reactivity. Fig. 4.27(C) shows a comparison of the impact of SMSI and A–SMSI formation on the reactivity of 2%Rh/Nb_2O_5. SMSI formation suppressed CH_4 production by ~40-fold on Rh nanoparticles, but left CO production on isolated Rh atoms nearly unchanged. Formation of the A-SMSI state decreased CH_4 formation by ~6-fold, however, the CO production increased by ~2.5-fold, attributed to the HCO_x functionalized NbO_x overlayer effect on the reactivity of Rh nanoparticles.

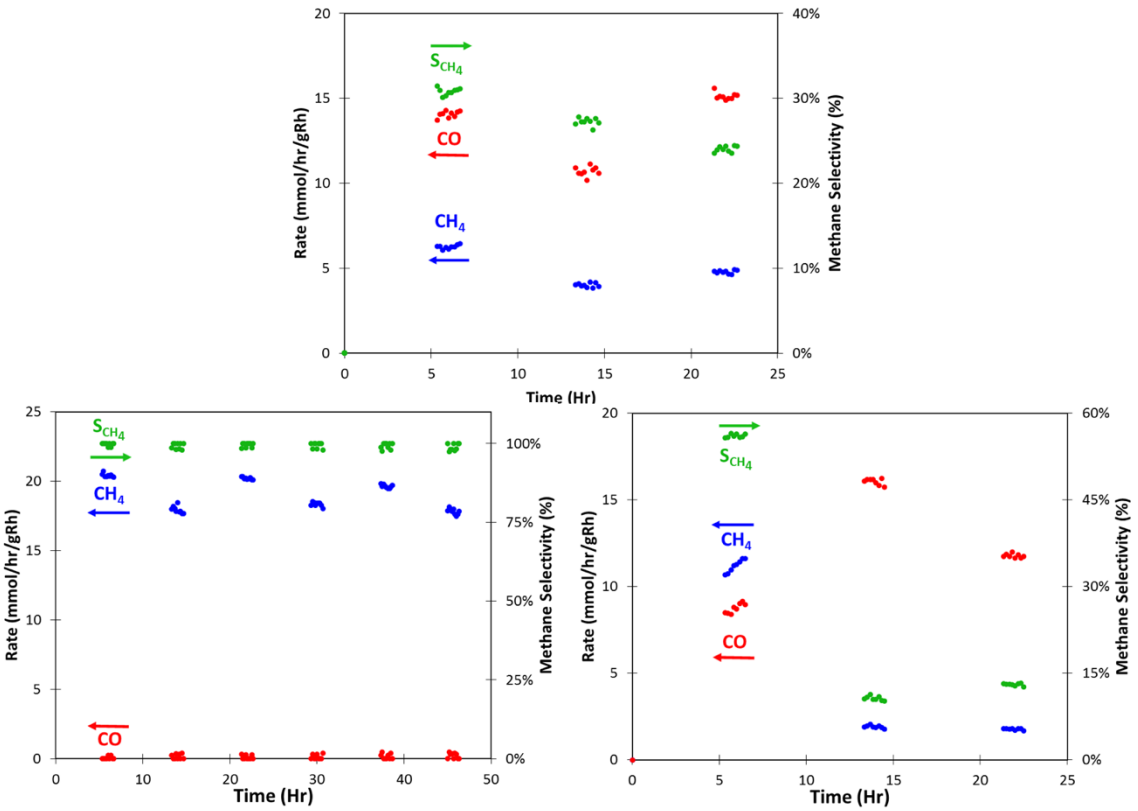

Fig. 4.28 Effect of cycling H_2 and $20CO_2$:H_2 treatments on Al_2O_3, CeO_2, and Nb_2O_5 The rate of CO and CH_4 production, and CH_4 selectivity measured at 200 °C 1 sccm CO_2, 1 sccm H_2, 98 sccm He following sequential 4 hour H_2 and $20CO_2$:H_2 treatments. (A) Cycling 2% Rh/CeO_2 with treatments of 4 hours of 20 sccm H_2 at 450 °C (data at 5-7 hours) and 4 hours of $20CO_2$:H_2 treatment at 250 °C (data at 13-15 hours) and re-reduction for 4 hours of 20 sccm H_2 at 450 °C (data at 21-23 hours). (B) Cycling 2% Rh/CeO_2. The data with the higher CH_4 production rates were after being reduced at 450 °C in pure H_2 for 4h and the data with slightly reduced CH_4 production rate were after being $20\%CO_2$:$2\%H_2$ treated. The small decrease in overall rate following each treatment cycle can be attributed to some sintering of Rh and loss of active surface area. (C) Cycling of 2% Rh/Nb_2O_5 with treatments of 4 hours of 20 sccm H_2 at 300 °C (data at 5-7 hours) and 4 hours of $20CO_2$:H_2 treatment at 250 °C (data at 13-15 hours) and re-reduction for 4 hours of 20 sccm H_2 at 300 °C (data at 21-23 hours). Lower reduction temperature was chosen to minimize the impact of SMSI overlayer formation inherent to Nb_2O_5 supported Rh.[21]

In-Situ DRIFTS was also performed for all four supports to compare with the reactivity results and better understand the effect of the $20CO_2$:$2H_2$. Following reduction, under reaction conditions the spectrum primarily showed CO on Rh (linear stretch at ~2028 cm^{-1}, and broad bridge stretch at ~1880 cm^{-1}) and HCO_x on Al_2O_3 (peaks at 1590 and 1390 cm^{-1}), Figure 29. Under reaction conditions after $20CO_2$:$2H_2$ treatment, a decrease in the intensity of the CO stretch on Rh was observed and accompanied by an increase in the intensity of the HCO_x peaks on Al_2O_3. No shift in the frequency of the CO stretch on Rh was observed and the relative magnitude of the increase in HCO_x on the support was very small compared to the TiO_2 catalyst. The DRIFTS results on Rh/Al_2O_3 are consistent with the small change in reactivity, but no change in selectivity, following $20CO_2$:$2H_2$ treatment, in that the CO stretch on Rh did not shift and the magnitude of the change in support functionalization was minimal.

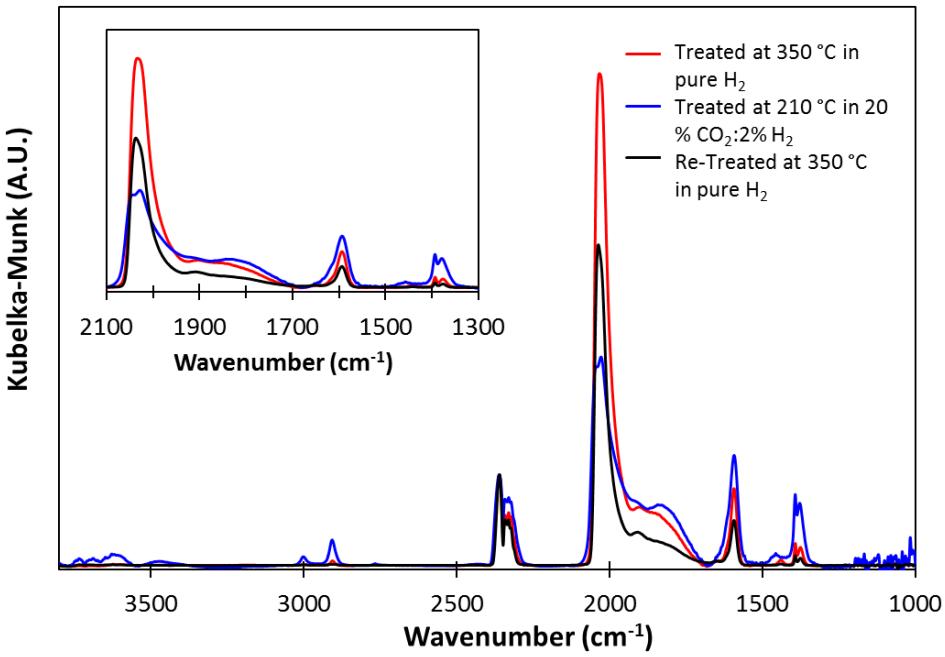

Fig. 4.29 In-situ DRIFT spectra of 2% Rh/Al_2O_3
Spectra were collected at 180 °C, 1sccm H_2, 1sccm CO_2, and 98 sccm He after H_2 reduction at 350 °C for 4 hours (red), 210 °C 20CO_2:2H_2 for 16 hours (blue) and re-reduction at 350 °C for 4 hours (black).

The 2%Rh/CeO_2 supported catalyst showed complex spectra under all reaction conditions indicating significant coverage of HCO_x on CeO_2 following each treatment, Fig 4.30. Essentially the spectra under reaction conditions look very similar following each treatment, which is in excellent agreement with the minimal change in reactivity of the catalyst following $20CO_2$:$2H_2$ treatments. This high coverage of HCO_x agrees with CeO_2 literature, as it is only a reducible support at much higher temperatures.[21]

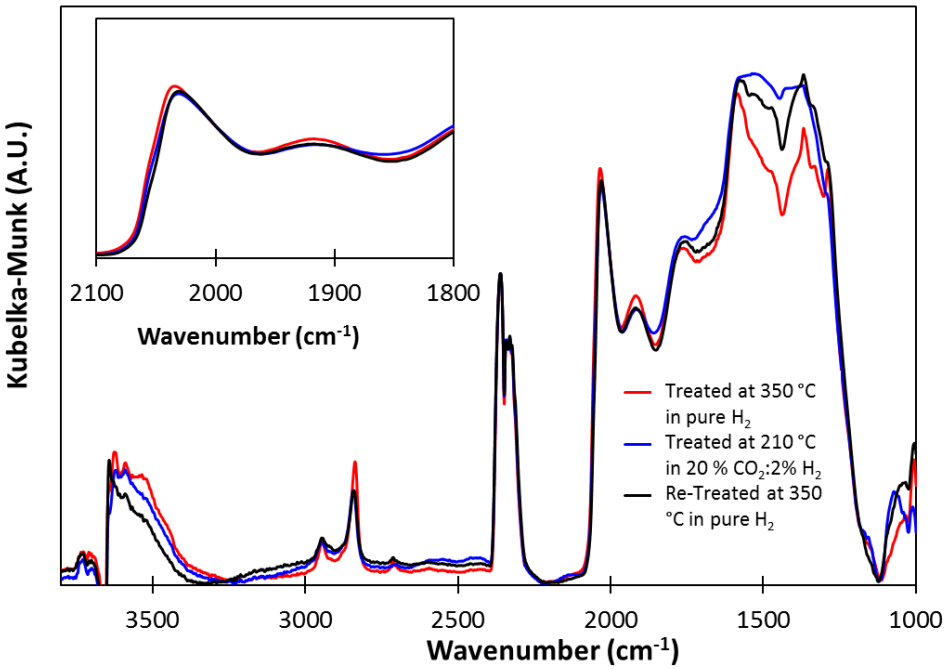

Fig. 4.30 In-situ DRIFT spectra of 2% Rh/CeO_2
Spectra were collected at 180 °C, 1sccm H_2, 1sccm CO_2, and 98 sccm He after H_2 reduction at 350 °C for 4 hours (red), 210 °C $20CO_2$:$2H_2$ for 16 hours (blue) and re-reduction at 350 °C for 4 hours (black).

Analysis of the DRIFT spectra of the 2%Rh/Nb_2O_5 catalyst under reaction conditions is more complicated than the other catalysts. Following 250 °C temperature reduction, under reaction conditions the primary features observed are associated with CO bound to isolated Rh atoms in a gem-dicarbonyl geometry (~2100 cm^{-1} and 2040 cm^{-1}). The high

population of CO gem-dicarbonyl species under reaction conditions is consistent with the high CO selectivity observed on the reduced catalyst, see Figure 4.27, and our previous work.[5] Along with the gem-dicarbonyl bands are smaller features associated with CO bound to Rh nanoparticles in bridge (1870 cm^{-1}) and linear (shoulder below 2040 cm^{-1}) configurations and HCO_x below 1600 cm^{-1}. Following $20CO_2$:$2H_2$ treatment, the gem-dicarbonyl stretches decrease in intensity significantly suggesting A-SMSI formation rendered the isolated Rh atoms unable to adsorb reactants. The decrease in the intensity of the gem dicarbonyl species is accompanied by a red-shift in frequency of the linear and bridge bound species. The strong initial gem-dicarbonyl signatures obfuscate calculation of the magnitude of the shift in the linear peak, but it can be seen that $20CO_2$:$2H_2$ treatment induced a shift in the bridge bound CO stretch from 1885 to 1835 cm^{-1}. In addition, a broad increase in the intensity of HCO_x species bound to Nb_2O_5 is observed below 1600 cm^{-1}. The changes in the DRIFT spectrum following $20CO_2$:$2H_2$ treatment showed a poisoning of isolated Rh atoms, redshift in the CO stretches associated with bonding to Rh nanoparticles and an increase in the concentration of HCO_x on Nb_2O_5. The results are generally consistent with observations on Rh/TiO_2 and the observed decrease in CH_4 production and increased CO production following $20CO_2$:$2H_2$ treatment. The re-reduction did not restore the gem-dicarbonyl species, however there was a small decrease in the intensity of the HCO_x species on Nb_2O_5 and partial blue-shift in the frequency of the bridge species. These results are consistent with an incomplete return of the Rh/Nb_2O_5 catalyst to the original reactivity following re-reduction, see Fig 4.28(C), which agrees with the more robust SMSI state observed in other work.[21] To summarize the reactivity and In-Situ

DRIFTS work on the various supports, *in-Situ* DRIFTS analyses agreed with changes in reactivity, where only for Nb_2O_5 were the CO stretching frequencies on Rh significantly red-shifted due to $20CO_2$:$2H_2$ treatment, see Fig. 4.29-4.31.

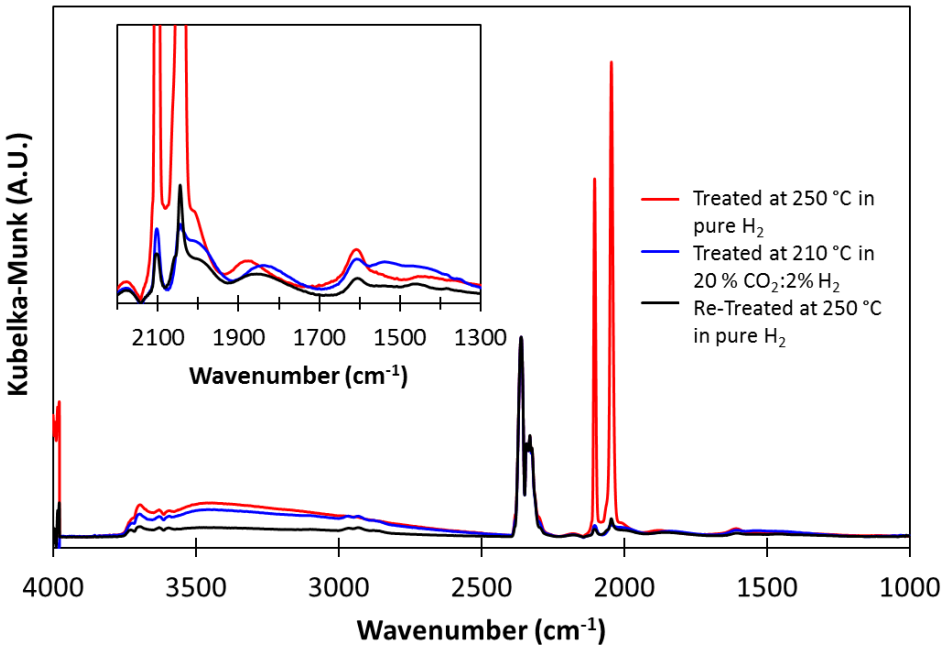

Fig. 4.31 In-situ DRIFT spectra of 2% Rh/Nb_2O_5.. Spectra were collected at 180 °C, 1sccm H_2, 1sccm CO_2, and 98 sccm He after H_2 reduction at 250 °C for 4 hours (red), 210 °C $20CO_2$:$2H_2$ for 16 hours (blue) and re-reduction at 250 °C for 4 hours (black).

4.5 Discussion

It is worth summarizing the evidence for participation of HCO_x adsorbates in the formation and stabilization of the A-SMSI overlayer and in modification of Rh reactivity. Correlation between the modified Rh reactivity and the appearance of HCO_x on the support measured by *in-situ* DRIFTS, similarity between the effects of $20CO_2$:$2H_2$ and formic acid treatment on Rh/TiO_2 reactivity, and the *in-situ* STEM/EELS results corroborate the role of HCO_x in mediating A-SMSI overlayer formation. Furthermore, the TPD experiment in Fig. 4.18(B,C) shows that HCO_x plays a critical role in stabilizing the A-SMSI overlayer

under humid environments. Coupled with the identification of Ti^{4+} in the A-SMSI overlayer by *in-situ* EELS, we hypothesize that HCO_x species coordinate with Ti in the overlayer thereby decreasing the driving force for re-oxidation of the overlayer. Finally, while there is no direct evidence that HCO_x species contribute to modification of Rh reactivity, it is clearly based on the particle size independent influence of the overlayer on Rh reactivity that the A-SMSI effect on Rh reactivity is a local effect at the Rh/A-SMSI overlayer interface.

We hypothesize a few mechanisms by which A-SMSI overlayer formation could induce the observed switch in CO_2 reduction selectivity. The downshift in CO stretching frequency could suggest that the CO bond is significantly polarized, which would decrease the CO-Rh bond strength, allowing CO to desorb before being hydrogenated.[28–30] Another plausible mechanism is that local modification of the Rh electronic structure, due to coordination with the A-SMSI overlayer, decreases the surface coverage of atomic hydrogen, thereby minimizing the driving force for CO hydrogenation.[30] Finally, the drastic transformation in local active site environment could also change the CO_2 reduction reaction mechanism, allowing for the overlayer to play a direct role as an active site.[7]

The formation mechanism and characteristics of the A-SMSI overlayers proposed here, and the traditional SMSI overlayer described by Tauster, are schematically depicted in Fig. 4.32. In both overlayers, migration of the support onto the catalytically active metal is induced by oxygen vacancy formation in the support. For SMSI overlayer formation, H_2 treatment at ~500 ˚C induces oxygen vacancy formation in the support, driving the formation of an impermeable, crystalline and fully reduced metal-oxide overlayer on the

active catalytic metal. Formation of the A-SMSI overlayer is mediated by high coverage of HCO_x on the support at 150-300 ˚C, which causes oxygen-vacancy formation, and drives formation of a porous and partially reduced metal-oxide overlayer on the catalytically active metal. For SMSI overlayers formed with TiO_2, the overlayer is rapidly oxidized in the humid environment of the $CO_2 + H_2$ reaction, causing recession of the support off the metal and negating any influence on the catalytic reactivity of the underlying metal. SMSI overlayers formed with Nb_2O_5 are stable under humid reaction conditions and thus completely suppress the reactivity of catalytic nanoparticles. However, the A-SMSI overlayers derived from TiO_2 and Nb_2O_5 are stable under humid reaction conditions, enabling the overlayer to strongly influence reactivity of the catalytically active metal.

4.6 Conclusion

In summary, it has been demonstrated that the HCO_x adsorbates on TiO_2 and Nb_2O_5 supported Rh catalysts can induce oxygen vacancy formation in the support and drive the formation of an A-SMSI overlayer on Rh. The A-SMSI overlayer is porous, enabling access of gas phase species to interact with the Rh surface, and stable under humid reaction conditions. The existence of the A-SMSI overlayer locally modifies the reactivity of the underlying Rh nanoparticles surface, opening new avenues for tuning and controlling the reactivity of supported metal catalysts.

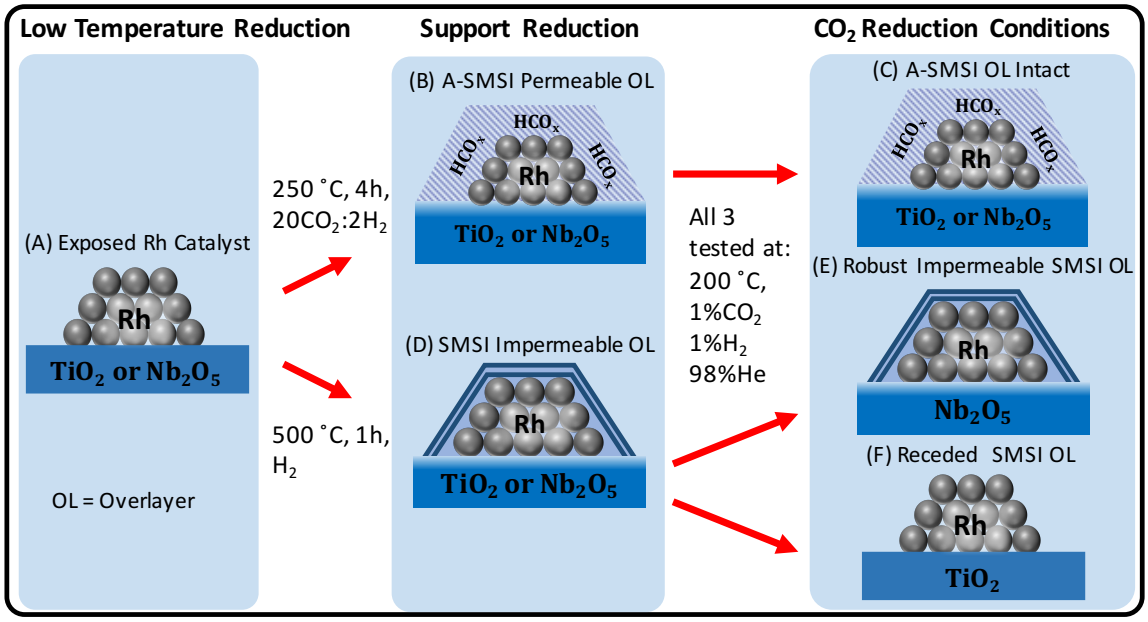

Fig 4.32 SMSI and A-SMSI structure and behavior. (A) Schematic showing bare Rh particles on TiO_2 or Nb_2O_5 with exposed Rh sites that favor CH_4 production. (B) $20CO_2$:$2H_2$ treated catalysts that forms a permeable A-SMSI overlayer composed of TiO_x species and HCO_x. (C) The stable A-SMSI overlayer under CO_2 reduction conditions modifies Rh catalytic behavior. (D) Rh/(TiO_2 or Nb_2O_5) following treatment with high temperature (500 ˚C) H_2, forming an impermeable SMSI overlayer. Crystalline bilayer structure observed for TiO_2 has yet to be confirmed for NbO_x SMSI state. (E) Reactivity results suggest there is a stable NbO_x SMSI overlayer that is impermeable in CO_2 reduction conditions, completely suppressing the reactivity of Rh nanoparticles. (F) TiO_x SMSI overlayer recedes off Rh when exposed to CO_2 reduction conditions due to water re-oxidizing TiO_x to TiO_2. The catalytic behavior of (F) is nearly identical to (A).

4.7 References

1 P. Christopher and S. Linic, *J. Am. Chem. Soc.*, 2008, **130**, 11264–11265.

2 F. Studt, I. Sharafutdinov, F. Abild-Pedersen, C. F. Elkjær, J. S. Hummelshøj, S. Dahl, I. Chorkendorff and J. K. Nørskov, *Nat. Chem.*, 2014, **6**, 320–324.

3 F. Calle-Vallejo, T. Jakub, V. Colic, P. Sautet, J. Tymoczko, V. Colic, Q. H. Vu, M. D. Pohl, K. Morgenstern, D. Loffreda, P. Sautet, W. Schuhmann and A. S. Bandarenka, *Science*, 2015, **350**, 185–189.

4 A. Holewinski, J.-C. Idrobo and S. Linic, *Nat. Chem.*, 2014, **6**, 828–834.

5 J. C. Matsubu, V. N. Yang and P. Christopher, *J. Am. Chem. Soc.*, 2015, **137**, 3076–3084.

6 M. Behrens, F. Studt, I. Kasatkin, S. Kühl, M. Hävecker, F. Abild-Pedersen, S. Zander, F. Girgsdies, P. Kurr, B.-L. Kniep, M. Tovar, R. W. Fischer, J. K. Nørskov and R. Schlögl, *Science*, 2012, **336**, 893–897.

7 J. Graciani, K. Mudiyanselage, F. Xu, A. E. Baber, J. Evans, S. D. Senanayake, D. J. Stacchiola, P. Liu, J. Hrbek, J. F. Sanz and J. A. Rodriguez, *Science*, 2014, **345**, 546–550.

8 J. A. Farmer and C. T. Campbell, *Science*, 2010, **329**, 933–936.

9 T. Ioannides and X. E. Verykios, *J. Catal.*, 1996, **161**, 560–569.

10 A. Bruix, J. a Rodriguez, P. J. Ramírez, S. D. Senanayake, J. Evans, J. B. Park, D. Stacchiola, P. Liu, J. Hrbek and F. Illas, *J. Am. Chem. Soc.*, 2012, **134**, 8968–8974.

11 C. T. Campbell, *Nat. Chem.*, 2012, **4**, 597–598.

12 Y. Lykhach, S. M. Kozlov, T. Skála, A. Tovt, V. Stetsovych, N. Tsud, F. Dvořák, V. Johánek, A. Neitzel, J. Mysliveček, S. Fabris, V. Matolín, K. M. Neyman and J. Libuda, *Nat. Mater.*, 2015, **15**, 284–288.

13 J. Saavedra, H. A. Doan, C. J. Pursell, L. C. Grabow and B. D. Chandler, *Science*, 2014, **345**, 1599–1602.

14 I. X. Green, W. Tang, M. Neurock and J. T. Yates Jr., *Science*, 2011, **333**, 736–739.

15 S. J. Tauster, S. C. Fung and R. L. Garten, *J. Am. Chem. Soc.*, 1978, **100**, 170–175.

16 S. J. Tauster, *Acc. Chem. Res.*, 1987, **20**, 389–394.

17 O. Dulub, W. Hebenstreit and U. Diebold, *Phys. Rev. Lett.*, 2000, **84**, 3646–3649.

18 A. K. Datye, D. S. Kalakkad, M. H. Yao and D. J. Smith, *J. Catal.*, 1995, **155**, 148–153.

19 G. L. Haller and D. E. Resasco, *Adv. Catal.*, 1989, **36**, 173–235.

20 S. Sakellson, M. McMillan and G. L. Haller, *J. Phys. Chem.*, 1986, **90**, 1733–1736.

21 C. Deleitenburg and A. Trovarelli, *J. Catal.*, 1995, **156**, 171–174.

22 T. Uchijima, *Catal. Today*, 1996, **28**, 105–117.

23 A. Boffa, C. Lin, A. T. Bell and G. A. Somorjai, *J. Catal.*, 1994, **149**, 149–158.

24 M. A. Vannice and B. Sen, *J. Catal.*, 1989, **115**, 65–78.

25 X. Y. Shi, W. Zhang, C. Zhang, W. T. Zheng, H. Chen and J. G. Qi, *J. Microsc.*, 2015, **00**, 1–13.

26 S. Bernal, J. J. Calvino, M. A. Cauqui, J. M. Gatica, C. L??pez Cartes, J. A. P??rez Omil and J. M. Pintado, *Catal. Today*, 2003, **77**, 385–406.

27 P. J. Chupas, K. W. Chapman, C. Kurtz, J. C. Hanson, P. L. Lee and C. P. Grey, *J. Appl. Crystallogr.*, 2008, **41**, 822–824.

28 M. Newville, *J. Synchrotron Radiat.*, 2001, **8**, 322–324.

29 S. I. Zabinsky, J. J. Rehr, A. Ankudinov, R. C. Albers and M. J. Eller, *Phys. Rev. B*, 1995, **52**, 2995–3009.

30 M. D. Porosoff, B. Yan and J. G. Chen, *J. Mater. Chem.*, 2016.

31 M. D. Porosoff and J. G. Chen, *J. Catal.*, 2013, **301**, 30–37.

32 P. Panagiotopoulou, D. I. Kondarides and X. E. Verykios, *Appl. Catal. A Gen.*, 2008, **344**, 45–54.

33 T. Avanesian, G. S. Gusmão and P. Christopher, *J. Catal.*, 2016.

34 F. Solymosi, T. Bánsági and É. Novák, *J. Cataysis*, 1988, **112**, 183–193.

35 P. Serna and B. C. Gates, *J. Am. Chem. Soc.*, 2011, **133**, 4714–7.

36 A. Karelovic and P. Ruiz, *J. Catal.*, 2013, **301**, 141–153.

37 M. A. Henderson and S. D. Worely, *J. Phys. Chem.*, 1985, **89**, 1417–1423.

38 M. J. Lundwall, S. M. McClure and D. W. Goodman, *J. Phys. Chem. C*, 2010, **114**, 7904–7912.

39 L. Brabec and J. Nováková, *J. Mol. Catal. A Chem.*, 2001, **166**, 283–292.

40 P. Deshlahra, J. Conway, E. E. Wolf and W. F. Schneider, *Langmuir*, 2012, **28**, 8408–8417.

41 K. K. Bando, K. Sayama, H. Kusama, K. Okabe and H. Arakawa, *Appl. Catal. A Gen.*, 1997, **165**, 391–409.

42 G. L. Haller, V. E. Henrich, M. McMillan, D. E. Resasco, H. R. Sadeghi and S. Sakellson, *Int. Congr. Catal.*, 1984, **V**, 135–144.

43 M. A. Henderson, *J. Phys. Chem. B*, 1997, **101**, 221–229.

44 U. Diebold, *Surf. Sci. Rep.*, 2003, **48**, 53–229.

45 Y. Morikawa, I. Takahashi, M. Aizawa, Y. Namai, T. Sasaki and Y. Iwasawa, *J. Phys. Chem. B*, 2004, **108**, 14446–14451.

46 M. Bowker, P. Stone, P. Morrall, R. Smith, R. Bennett, N. Perkins, R. Kvon, C. Pang, E. Fourre and M. Hall, *J. Catal.*, 2005, **234**, 172–181.

47 J. J. Liu, *ChemCatChem*, 2011, **3**, 934–948.

48 A. D. Logan, E. J. Braunschweig, A. K. Datye and D. J. Smith, *Langmuir*, 1988, **4**, 827–830.

49. R.E. Benfield, *J. Chemical Soc. Faraday Trans.* **88**, 1107-1110 (1992)

50. K. Sasaki, N. Marinkovic, in C.S.S.R. Kumar (Ed.), (Springer, Berlin, 2016)

Chapter 5 Critical Role of Interfacial Effects on the Reactivity of Semiconductor-Cocatalyst Junctions for Photocatalytic Oxygen Evolution from Water

5.1 Summary

Photocatalytic water splitting has the potential to provide a sustainable approach for storing the energy of solar photons in the form of chemical bonds. Much work has been executed towards developing semiconducting light absorbers (SC) and co-catalysts (CC) for photoelectrochemical (PEC) and particulate photocatalytic (PPC) water splitting systems. However, minimal insights exist into how the formation of junctions between highly dispersed CC clusters and nanoparticle SCs influences the reactivity of the system, as compared to the reactivity of the CCs in electrochemical environments. In this work, 15 materials consisting of five different CC nanoclusters deposited on three different nanoparticle SCs were synthesized, characterized, and tested for oxygen evolution reaction (OER) activity. The SCs were chosen based on their similar n-type behavior and low OER activity, and the CCs were chosen based on their benchmarked OER reactivity in electrochemical measurements. We found that the photocatalytic activity of these samples for the OER did not directly correlate with the reactivity of the CCs measured under electrochemical conditions. Instead, the performance was controlled by interfacial effects specific to each SC|CC junction. CC electrical conductivity and SC supplied OER overpotential were the major factors identified to strongly affect OER rate. This work suggests that when designing an optimal photocatalyst, one can not simply deposit the most active CC (as measured in electrochemical conditions) on the SC which absorbs the highest fraction of the solar flux, as the CC-SC pairing requires critical interfacial considerations.

5.2 Introduction

The utilization of solar energy to split water, producing H_2 and O_2, is a potentially transformative technology that could provide a nearly endless supply of sustainable fuels and chemicals. Various approaches for solar water splitting have been envisioned and realized[1–4], although efficiencies and costs are still prohibitive for large-scale application.[5,6] Technologies emerging as the most probable candidates for large scale solar water splitting include photo-electro-chemical (PEC) cells and particulate photocatalytic (PPC) processes. While current state-of-the-art PEC cells exhibit significantly more efficient performance than PPC processes, techno-economic analyses have suggested that PPC processes have the potential to produce H_2 at the lowest costs.[5] Regardless of whether PEC or PPC processes are used to split water, effective transfer of photo-generated charge carriers (electrons, e^-, and holes, h^+) from light absorbing semiconductors (SC) to reactive co-catalysts (CC) that facilitate water splitting half-reactions (oxygen evolution reaction (OER) and hydrogen evolution reaction (HER)) is requisite for high overall process efficiency.

Combinatorial efforts have been executed to identify SCs with broad-spectrum photon absorption,[7,8] targeted band positions,[9] excellent charge carrier transport,[10] and environmental stability.[11,12] Earth-abundant SCs with sufficient properties and n-type or p-type behavior have been developed to function as photoanodes (e.g. $BiVO_4$ or WO_3)[13,14] or photocathodes (e.g. p-Si)[15] and further SCs have been identified with characteristics to act simultaneously as a photoanode and photocathode in PPC processes for water splitting (e.g. GaN:ZnO).[16] Considerable research has also been dedicated to designing electrochemical

catalysts that can drive the HER and OER at low overpotentials.[17] The overpotential of a catalyst is the required potential to make the entire reaction pathway downhill in energy.[17a] Thus, this is an inherent measurement of the electrocatalytic reactivity of a material. Insights into surface chemical properties of catalytic materials that optimize performance for HER and OER under electrochemical environments have been developed, allowing for the design of earth-abundant catalysts with relatively low required overpotentials for water splitting half reactions (e.g. MoS_2 for HER and Ni_xFe_yOOH for OER).[18,19] However, only a few studies exist that systematically examine charge transfer from SC to CC under relevant PPC or PEC reaction conditions to identify how characteristics of SC|CC junctions influence the performance of solar water splitting technologies.[20–22] This raises a simple question: Can we exploit extensive studies that have been executed to identify optimal HER and OER catalysts in electrochemical environments to predict their reactivity in PEC/PPC systems that provide charge carriers via charge transfer across the SC|CC junction, rather than directly from a conductive support?

In the most basic analysis of charge transport across SC|CC junctions, electronic levels (valence band maximum (VBM), conduction band minimum (CBM) and Fermi level (E_f)) of the SC and CC are defined by their energies in vacuum. Upon SC|CC junction formation, E_f of the two components equilibrate through charge transfer.[23] The direction of charge flow and strength of the rectifying effect are defined by the relative E_f of the SC and CC. Equilibration of E_f induces band bending in the SC near the SC|CC junction (and in the CC if it is not metallic). [23] The band bending direction (down or up) defines which charge carriers (e^-, or, h^+) travel across the junction after illumination of the SC. For

example, a junction formed between a prototypical n-type SC and late transition metal will cause SC bands to bend up due to charge transfer from the metal $E_{f,}$ into the SC, such that under illumination, h^+s will migrate across the SC|CC junction. However, this depiction of charge transport across SC|CC junctions is only relevant for PEC systems where the CC forms a thick >10 nm pinhole free overlayer on the SC, a so-called buried junction.[23,24] In this case, the overpotential remaining in the charge carriers after traversing the bent bands at the SC|CC junction and the inherent kinetics on the CC surface together control the efficiency of charge carriers generated via SC photon absorption for driving charge transfer reactions at the CC surface. This mechanistic picture of the SC|CC junction has no application in PPC systems because SCs that drive both HER and OER half reactions do not use comprehensive CC layers.

Rather than buried junctions, SC|CC junctions in PPC materials are formed by few nanometer diameter CC nanoparticles dispersed at low surface densities on particulate SCs with sizes from ~25-1000 nm diameter, submerged in an electrolyte (EL). The formation of EL|SC and EL|CC junctions modify the vacuum picture of SC|CC junctions due to the influence of the EL on electronic levels of the CC and SC. Because the EL has a significantly larger magnitude of charge carriers compared to the SC or CC, and high conductivity, E_f of the SC, CC and SC|CC junction equilibrate to the electrolyte E_f. If the CC nanoparticles are small enough (smaller than< ~200 nm diameter) and surface density on SC is low enough (< ~50% coverage) the SC|CC junction energetics become equivalent to the SC|EL junction.[24] Thus, band bending at the SC surface and charge carrier migration across the SC|CC junction are defined by characteristics of the SC|EL junction. This is

known as the "pinch-off" effect, and is analogous to the recently described adaptive SC|CC junctions that form with commensurate ion permeable CCs, such as transition metal oxyhydroxides, on SCs.[25] In these situations, with the SC|CC junction acting identically to the SC|EL junction in terms of band bending, it would be expected that differences between CC performance in either PEC and PCC systems should be predicted only by the inherent reactivity of the CCs under electrochemical environments, as charge transfer across the CC|SC junction should be identical for all CCs.

Few studies exist that systematically examine the reactivity of CC in electrochemical environments and at SC|CC junctions in PECs or PPCs to elucidate the influence of charge transfer and electronic level alignment on the performance of solar water splitting systems. One such study examining HER over various metal CC particles deposited on a p-type Si SC (non-commensurate CC overlayers) showed that the PEC performance of the systems trended with the inherent activity of the CCs in electrochemical environments, suggesting no impact of the SC|CC junction formation on the CC reactivity.[26] This demonstrates that for PEC photocathodes consisting of Si photon absorbers and metal CC, optimal HER CCs can be interfaced with the SC to achieve excellent performance.

More recently, the reactivity of SC|CC junctions consisting of an n-type TiO_2 SC and dense commensurate oxide CC layers (NiO_x, CoO_x, IrO_x and FeO_x) or ion-permeable oxyhydroxide CCs (NiOOH, FeOOH, CoOOH, IrO_xxH_2O) were compared for PEC OER.[25] For the ion-permeable CCs it was found that all systems performed similarly in PEC OER. This was attributed to the identical SC|CC junction energetics (acting essentially as SC|EL layers) and the large SC supplied OER overpotential (see Figure 5.1(a)) based on the

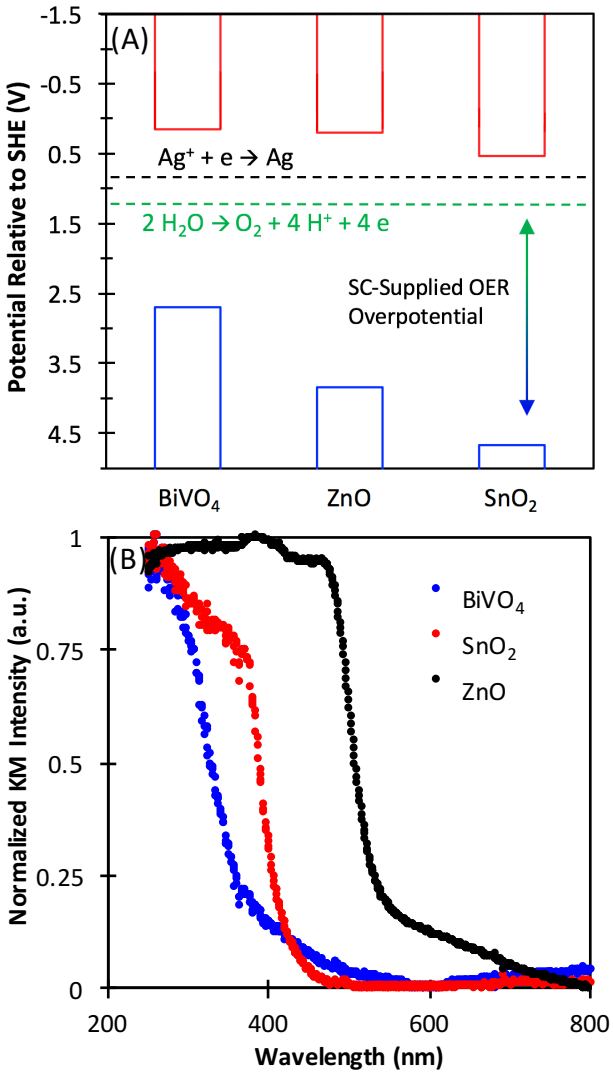

Figure 5.1 A) VBM and CBM for each SC compared to the reduction potential of Ag+ (electron scavenger) and the oxidation potential of water. It is assumed that due to the n-type electronic behavior of all three SCs that the Ef levels are identical to the CBM. The difference in energy between each SC VBM and water oxidation potential is amount of oxidation potential h^+s generated in the SC would have for driving the OER and is denoted in this work as the SC supplied OER overpotential. B) DR-UV-Vis spectra of SCs plotted in normalized KM units.

significant difference between n-TiO_2 VBM and the OER potential and minimal band bending in the n-TiO_2 layer. On the other hand, the dense overlayer SC|CC junction performances varied significantly and inconsistently with the CC OER reactivity in electrochemical environments. Variations in the buried SC|CC junction performance from

the performance of CCs in electrochemical environments were attributed to differences in h^+ transport across the junction. Whether these variations could be predicted from the vacuum band-bending picture described above, or a more complex function of junction formation was not explored.

These previous studies do not shed light on how SC|CC junctions influence the performance of water splitting PPC's consisting of CC nanoparticles on the SC, creating SC|CC, SC|EL and CC|EL junctions. This leaves an open question of whether optimum OER CCs identified in electrochemical conditions can be expected to be optimum CCs in PPC water splitting processes. More generally, it is still not understood whether the performance of SC|CC junctions for OER formed with dense non-ion-permeable CCs is controlled by band bending at the SC|CC junction, or is a more complex function of junction formation.

Here we report on the reactivity of SC|CC junctions for OER in a PPC geometry of CC nanoparticles (IrO_x, CoO_x, RuO_x, NiO_x and MnO_x) deposited on n-type SC particles (SnO_2, ZnO, and $BiVO_4$). CC particles were prepared at low weight loadings to allow the SC|CC junctions to act in a pinch off regime as SC|EL junctions. SCs were chosen based on their similar E_f positions, rendering band bending at the SC|EL interface to be similar, but different VBM energies, rendering the overpotential in the h^+ supplied to the CC different. The reactivity of these SC|CC junctions for OER exhibited significant variations compared to trends expected from electrochemical measurements of CC reactivity. Furthermore, trends in the CC reactivity varied significantly when comparing the relative reactivity of each CC on different SCs. The results strongly suggest that for SC|CC

junctions formed between oxide components in PPC OER systems, the reactivity of the junction is significantly influenced by SC supplied overpotential, in combination with CC electrical conductivity, that together control charge transport efficiency across the SC|CC junction and ultimately OER rate. Essentially, interfacial effects at the SC|CC junction significantly control the rate of OER, rather than the inherent CC reactivity measured under electrochemical environments.[27,28] These studies highlight the need for detailed interfacial analysis at oxide CC and oxide SC junctions on PPC, and perhaps PEC, to optimize OER performance.

5.3 Experimental section

5.3.1 Materials.

Metal catalyst precursors: cobalt (II) nitrate hexahydrate (cat. 203106), nickel (II) nitrate hexahydrate (cat. 203874), ruthenium (III) nitrosyl nitrate (cat. 373567), manganese (II) nitrate hydrate (cat. 203742), and iridium (III) chloride hydrate (203491) were purchased from Sigma-Aldrich. Precursors for the $BiVO_4$ nanoparticle support consisted of bismuth nitrate pentahydrate (cat. 467839), ethylenediaminetetraacetic acid (EDTA) (cat. E9884), and ammonium metavanadate (cat. 10028) and were purchased from Sigma-Aldrich. ZnO (cat. 5810HT) and SnO_2 (cat. NS6130-03-349) nanoparticle SC supports were obtained from NanoAmor and Nanoshel respectively.

5.3.2 Material Synthesis.

$BiVO_4$ was synthesized via an EDTA-modified hydrothermal process.[29] In a typical synthesis, 10 mmol $Bi(NO_3)_3 \cdot 5\ H_2O$ and 10 mmol EDTA were dissolved in 100 ml of aqueous 2M HNO_3 solution under vigorous agitation at room temperature in a 250 mL

media bottle for 10 minutes. Afterwards, 10 mmol NH_4VO_3 was added into the mixture and stirred continuously for 30 minutes. The hydrothermal process was then carried out at 90 ˚C for 6 hours after which the mixture was allowed to cool to room temperature. The resulting precipitate was washed with a distilled water-ethanol solution via centrifugation and dried at 90 ˚C in air.

Five weight loadings of Co, Ru, Mn, Ir, and Ni oxides were deposited onto ZnO (0.001%, 0.01%, 0.1%, 1%, 3%) and 1% weight loadings were deposited onto SnO_2, and $BiVO_4$ nanoparticle supports by a simple impregnation method. In a typical synthesis for ZnO supported catalysts, the quantity of catalyst precursor necessary for 300 mg of each weight loading was dissolved in an evaporation dish with 500 μL of deionized water. An appropriate amount of ZnO was added to the aqueous metal catalyst solution and mixed with a stir rod until homogeneous in appearance. The resulting mixture was dried at 90 °C under vacuum and calcined in a tube furnace in air with the parameters found in Table 5.1.[21,30–33] This process was repeated for SnO_2 and $BiVO_4$ using 800 μL and 400 μL of deionized water respectively.

Table 5.1 Temperature and duration of sample calcination in air during CC synthesis on the SCs.

Co-Catalyst	Temperature (˚C)	Hours
IrO_x	550	5
MnO_x	400	2
RuO_x	400	6
NiO_x	400	3
CoO_x	500	2

5.3.3 Characterizations

Powder X-ray diffraction (PXRD) was carried out on a PANalytical Empyrean X-ray diffractometer using a Cu Kα radiation source (λ=0.15425 nm). A generator voltage of 45 kV and emission current of 40 mA were employed. The scanning range was 10-70° (2θ) with a step size of 0.10° and a step time of .0275 s. The phases were determined by identifying the top matching score between each XRD spectrum and known library peak positions within the PANalytical software.

Surface areas of the SCs were measured by N_2 physical adsorption at 77K using the BET method with a Micromeritics ASAP 2020. The samples were degassed *in situ* at 350 °C for 3 hours and cooled to 35°C under vacuum prior to analysis. Diffuse reflectance spectra of the SCs were recorded with a Thermo Scientific Evolution 300 UV-Vis spectrophotometer and a Harrick Praying Mantis™ diffuse reflectance accessory. SC band gap energies were determined using the Kubelka-Munk technique.

Scanning Transmission electron microscopy (STEM) imaging was performed on a FEI Titan Themis 300 instrument equipped with XFEG electron gun, 4kx4K CETA digital camera, a SuperX EDX system with 4x30 mm2 SDD detectors and 4kx4k Fischione Instruments Inc. annular dark field detector model 3000. High Angle Annular Dark Filed (HAADF) imaging was done with a probe convergence angle of 10 mrad, probe current of 50 pA and collection angle of 40 to 233 mrad. Elemental mapping was performed with an electron beam probe current of 350 pA at 512x512 and 1024 x1025 frame resolution. The specimens were prepared by deposition from suspension on 200 mesh Cu support grid covered with lacey carbon support film. The HAADF imaging was coupled with EDS

elemental mapping to examine the dispersion of the IrO_x and CoO_x CCs on all three SCs to verify that CC dispersion did not play a significant role in observed reactivity trends.

5.3.4 Reactivity Experiments

The OER measurements were carried out in 65 ml custom built glass batch reactors. In a typical experiment, 15 mg of catalyst was suspended in distilled water through sonication followed by $AgNO_3$ addition to produce a 50mM $AgNO_3$ solution. Prior to irradiation, the reactor system underwent a series of He (99.999%) purging and high-vacuum pump evacuations to remove O_2 and N_2 from the reaction environment. After 3 sequential purge-evacuation cycles the photo-reactor was pressurized to 10 psig with He to maintain a positive pressure environment and therefore prevent O_2 and N_2 contamination from air. The reactors were left in pure He environment for 30 minutes to allow trace O_2 and N_2 concentrations to equilibrate prior to illumination. The start of the oxygen evolution reaction was signaled by illumination of the reactor with a 100 watt Dolan Jenner MH-100 metal halide lamp with a measured intensity of approximately 640 mW/cm^2 and the irradiation spectrum is shown in figure 5.2. During irradiation, 1 mL gas aliquots of the reactor headspace were drawn every 7-8 minutes with a valved-syringe and quantified using an SRI (MG#3) gas chromatograph equipped with a helium ionization detector (HID) and a thermal conductivity detector (TCD). Special care was taken to maintain strict time consistency between each sample taken and to minimize any effects from atmospheric O_2. N_2 and O_2 concentrations were tracked to account for any atmospheric O_2 that could be mistaken for evolved O_2, where a simple experimentally determined $3N_2$:O_2 molar ratio was utilized to subtract away atmospheric/non-evolved O_2,. The accumulation of the

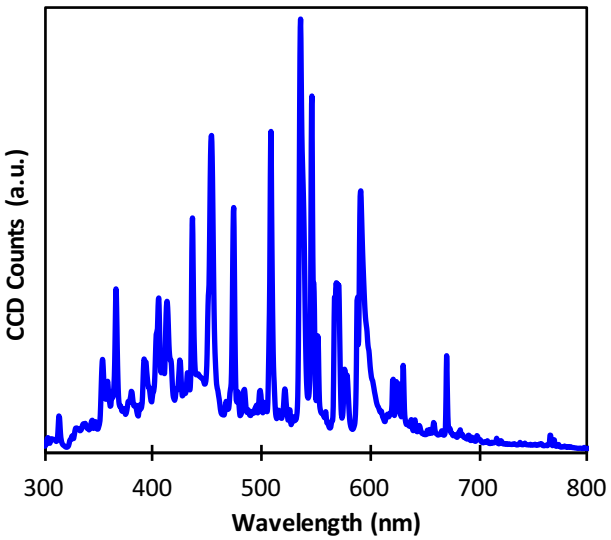

Figure 5.2 Spectral output of metal halide lamp (MH100A)

evolved O_2 in the reactor headspace was plotted as a function of time and a photocatalytic OER rate, normalized by mass of catalyst and photo flux, was determined by calculating the slope of the increase in O_2 accumulation during the first 30 minutes following irradiation, as shown in Figure 5.3. Irradiation time was limited to 30 minutes to minimize

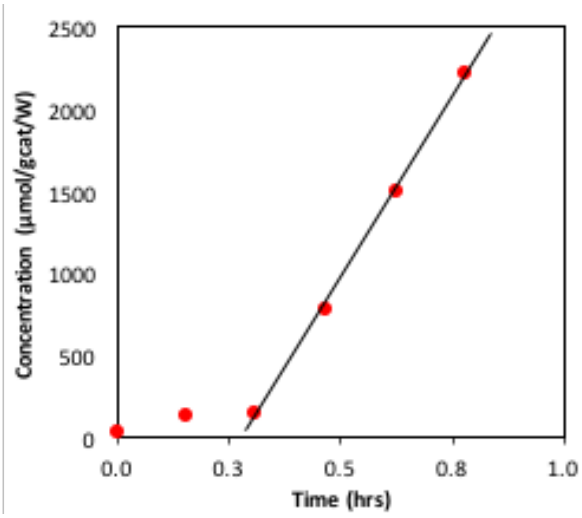

Figure 5.3 Typical O_2 accumulation plot, where slope of accumulation at onset of reactor illumination was used to determine OER rate.

the effect of Ag deposition from the sacrificial reagent on both light absorption (shading) and any potential catalytic effect from the Ag such as localized surface plasmon resonance.[34,35] Although irradiation time was limited to 30 minutes, linearity of the O_2 accumulation plots was verified to 4h experiment duration. The OER rate measurements were performed in duplicate to obtain error bars and ensure consistency of the catalytic performance.

5.4 Results

5.4.1 Characterizations

The three SCs examined in this study ($BiVO_4$, SnO_2, and ZnO) were chosen for their low inherent OER reactivity, Figure 5.4 and similar n-type electronic structure and E_f level positions, as shown in Figure 5.1(a). The E_fs of the SCs are similar to each other and to the E_f of the EL, suggesting minimal but consistent band bending in all systems. All five CCs used in this work are known to be active for electrocatalytic OER, with benchmarked differences in performance.[36] This creates an environment where the only difference between each CC on a new SC should be the efficiency of charge transfer across the SC|CC junction, and potentially the influence of the SC on the growth of the CC during synthesis. Due to the pinch-off effect, any change in the relative order of reactivity amongst CCs when deposited on the different supports would indicate an influence of the SC|CC junction on performance. For example, if one CC performed excellently relative to the other CCs on one semiconductor, but exhibited a different relative reactivity on another SC, one could attribute the difference in performance to the SC|CC junction characteristics. UV-Vis-DR absorption spectra for the SCs are shown in Fig 5.1(a), where $BiVO_4$ is the only SC to

absorb visible light, ZnO absorbs all of the UV spectrum and SnO_2 absorbs only wavelengths below 35 0nm, Figure 5.1(b). Band gap energies shown in Table 5.2 were determined by processing the absorbance data in Figure 5.1(b) with the Kubelka-Munk approach, Figure 5.5.

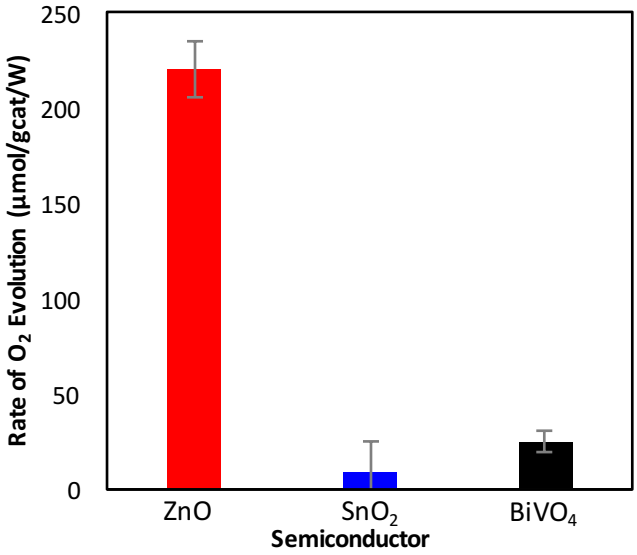

Figure 5.4 Rate of OER rate normalized per gram catalyst and power of lamp for ZnO, SnO_2, and $BiVO_4$ SCs. The rates for each SC were determined from the slope of the O_2 accumulation vs time plots similar to fig 5.3. Error bars were determined from testing the performance of each catalyst sample twice.

Table 5.2 Effect of calcination temperature on surface area and band gap energy

SC	Calcination Temp (°C)	Surface Area (m^2/g)	Band Gap (eV)
$BiVO_4$	400	.9	2.2
$BiVO_4$	550	N/A	2.3
SnO_2	400	5.8	3.5
SnO_2	550	6.9	3.3
ZnO	400	23.7	3.0
ZnO	550	17.9	2.9

Absorption spectra and corresponding band gap energies were in agreement with prior literature studying these materials.[29,37] Surface areas and absorption spectra of the SC supports were measured to ensure the supports did not undergo dramatic changes in surface area or band gap as a result of the range of calcination temperatures (400-550 ˚C) required to synthesize the desired CC oxide phases, Table 5.2. The SC crystal structures determined

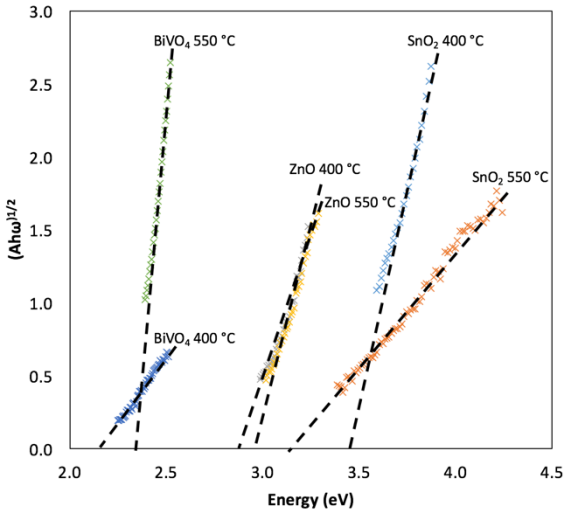

Fig 5.5 Plot of Kubelka-Munk function used to calculate band gap energies for SC pretreated at different conditions during CC synthesis.

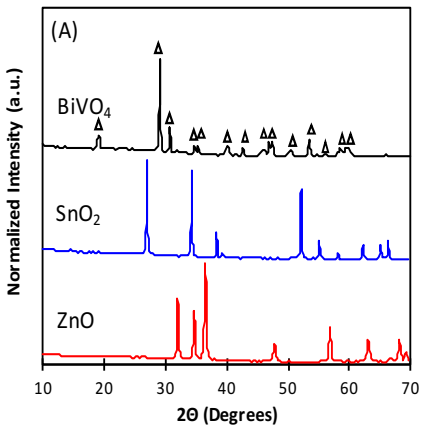

Figure 5.6 XRD spectra of the 3 SCs. All peaks observed were in agreement with the crystal structures of $BiVO_4$, SnO_2, and ZnO being monoclinic, rutile, and wurtzite, respectively. The triangles were added to denote known peaks for the assigned crystal structure for each SC and demonstrate that all observable peaks agreed with assigned structures.

via XRD were monoclinic for $BiVO_4$, rutile for SnO_2, and wurtzite for ZnO, Figure 5.6(a). These are consistent with the expected phases and with previously analyzed systems for photocatalytic applications.[13,38] STEM micrographs were taken of CoO_x and IrO_x on all 3 SCs to observe CC dispersion. Figure 5.7 shows that IrO_x homogeneously distributed at high dispersions on all 3 SCs, with particle sizes consistently below 5nm in diameter. CoO_x formed less uniformly on the SCs than IrO_x and with lower dispersions, where particles or particle aggregations existed from < 5nm up to 70nm, as shown in Figures 5.8. The order of dispersion for CoOx was ZnO>>$BiVO_4$>SnO_2 with particle sizes of 2-20nm, 5-70nm, and 15-70nm, respectively.

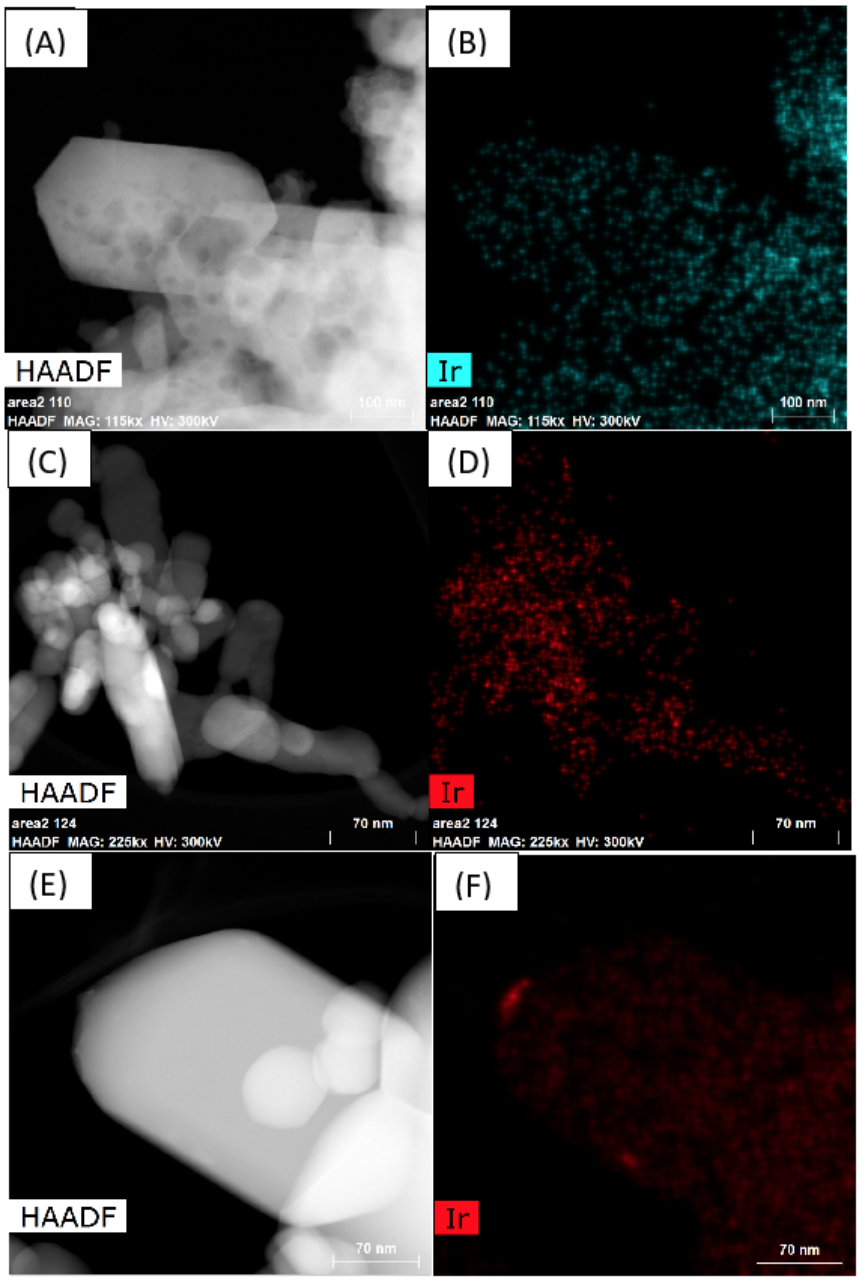

Figure 5.7 A) HAADF STEM analysis of 1% $IrO_x/BiVO_4$. (B) Corresponding EDS map showing IrO_x was highly and evenly dispersed on the $BiVO_4$ SC. (C) HAADF STEM analysis of 1% IrO_x/ZnO. (D) Corresponding EDS map showing high IrO_x dispersion with particle sizes < 5nm. (E) HAADF STEM analysis of 1% IrO_x/SnO_2. (F) Corresponding EDS map showing high IrO_x dispersion with particle sizes < 5nm. IrO_x was well dispersed on all 3 SCs

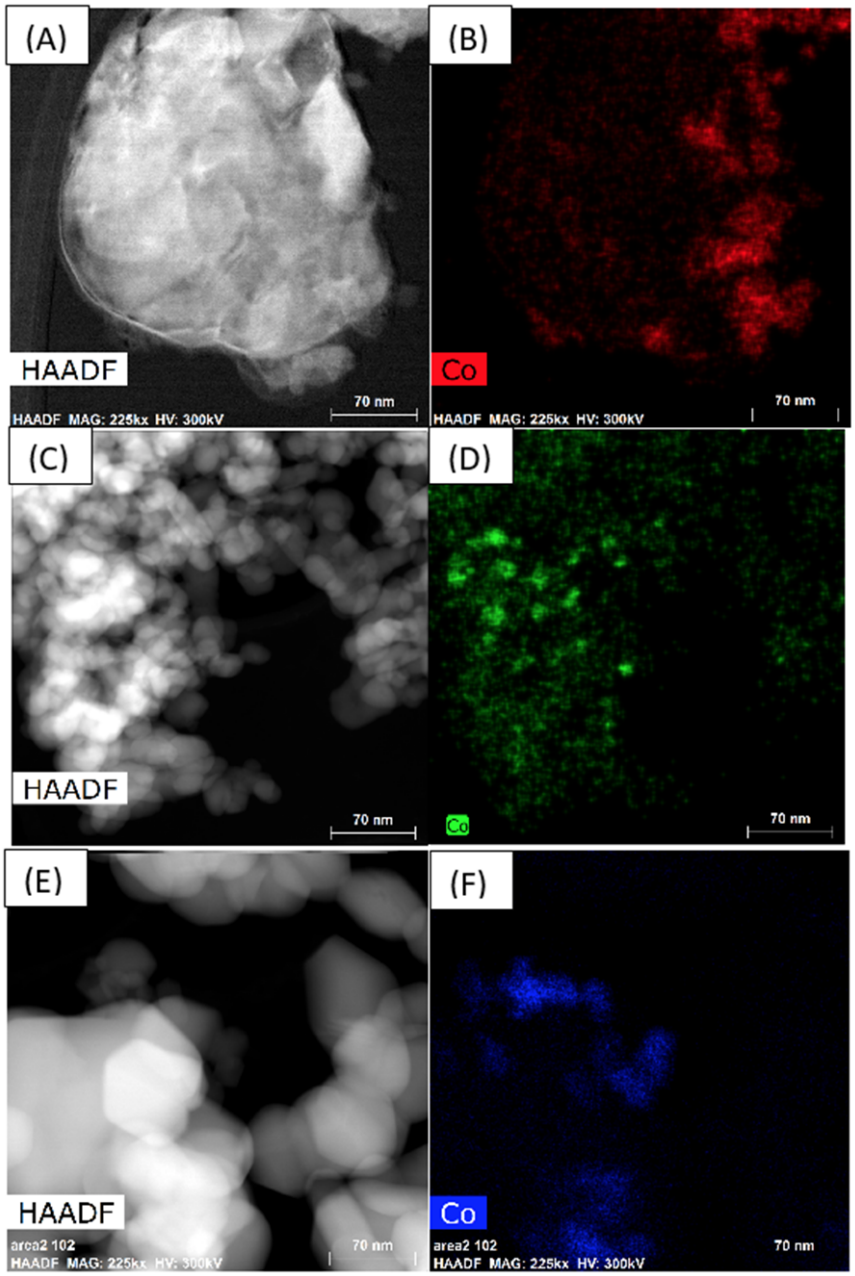

Figure 5.8 (A) HAADF STEM analysis of 1% CoO_x /$BiVO_4$. (B) Corresponding EDS map indicating Co NPs were present on the SC surface with particle and/or particle aggregations with sizes from <5nm up to 70nm. (C) HAADF STEM analysis of 1% CoO_x/ZnO. (D) Corresponding EDS map indicating Co NPs were present on the SC surface with particle and/or particle aggregations with sizes from <2nm up to ~20nm. (E) HAADF STEM analysis of 1% CoO_x/SnO_2. (F) Corresponding EDS map showing CoO_x formed large NPs or aggregates on SnO_2 of 15-70nm. ZnO supported more dispersed CoO_x NPs.

When working with PPC materials there exists an optimal CC weight loading, striking a balance between light absorption (high CC coverage can shadow the SC and reduce light absorption) and total exposed CC catalyst sites for driving the OER. The SCs in this work were chosen to have poor intrinsic OER reactivity, such that they could be treated as light absorbers in most systems and the CCs as the exclusive OER active sites, Figure 5.9. CC weight loading was varied on ZnO to identify the optimal weight loading for OER activity, where the optimal CC weight loading was 1% for all CCs, see Figure 5.10. Therefore, 1% CC weight loading was chosen as the OER CC weight loading for comparison across the systems. Furthermore, it is important to note that all the CC showed an optimum at 1% weight loading on ZnO, suggesting that even if 1% CC weight loading wasn't optimum for the other SCs, by having a consistent weight loading for all CCs the reactivity trend of the CCs on each SC could be reasonably compared. It is worth re-iterating that at these low CC loadings, the system is expected to act in the pinch off regime where the E_f of the EL controls the E_f of all junctions.

The stability of the suspension pH during the course of the reaction was tested with the most active system, CoO_x/ZnO, which had an initial pH of 6.25 and final pH of 6.0 after 30 minutes of reaction. This small change in pH is assumed to be negligible in terms of affecting the OER rate over the course of the 30 minute reaction. This effectively means that the E_f of the EL was constant for all experiments across both CCs and SCs allowing comparison of the results. Furthermore, it is worth noting that at these mild pH and short time scale experiments (30 min), the SCs and CCs are expected to be stable, i.e. no transformation to hydroxide phases or dissolution.

Figure 5.9 shows the rate of OER for all tested SC|CC systems. Each rate measurement was repeated two times and the error bars represent the standard deviation of the two measurements. Comparing the highest OER rate for each SC system (the OER rate on the highest performing CC), ZnO is the most active and SnO_2 was the least active with a 6:2:1 ratio in highest OER rate for ZnO:$BiVO_4$:SnO_2 supported catalysts. In Figure 5.9, the CCs are ordered from left to right in descending reactivity, as previously measured under electrochemical conditions.[39] If a direct translation from electrocatalytic performance could be made to our PPC system, the OER rates should descend from left to right. However, the PPC OER rates do not follow the same trend as predicted from electrocatalytic analysis, strongly suggesting the SC|CC junction influences the system reactivity. Interestingly, the highest OER rate for each SC was not achieved with the same CC, as CoO_x exhibited the highest activity on ZnO, and IrO_x exhibited the highest activity on $BiVO_4$, while IrO_x and CoO_x showed similar rates when deposited on SnO_2.

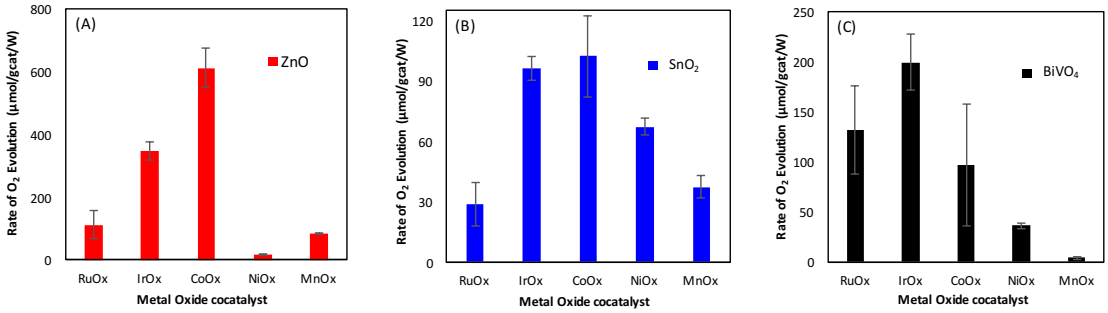

Figure 5.9 Rate of OER normalized per gram catalyst and lamp power for (A) ZnO (B) SnO_2 and (C) $BiVO_4$ supported CCs. The rates for each photocatalyst were determined from the slope of the O_2 accumulation as a function of time, similar to fig 5.3. Error bars denote the standard deviation of the rate, determined from testing the performance of each catalyst sample twice.

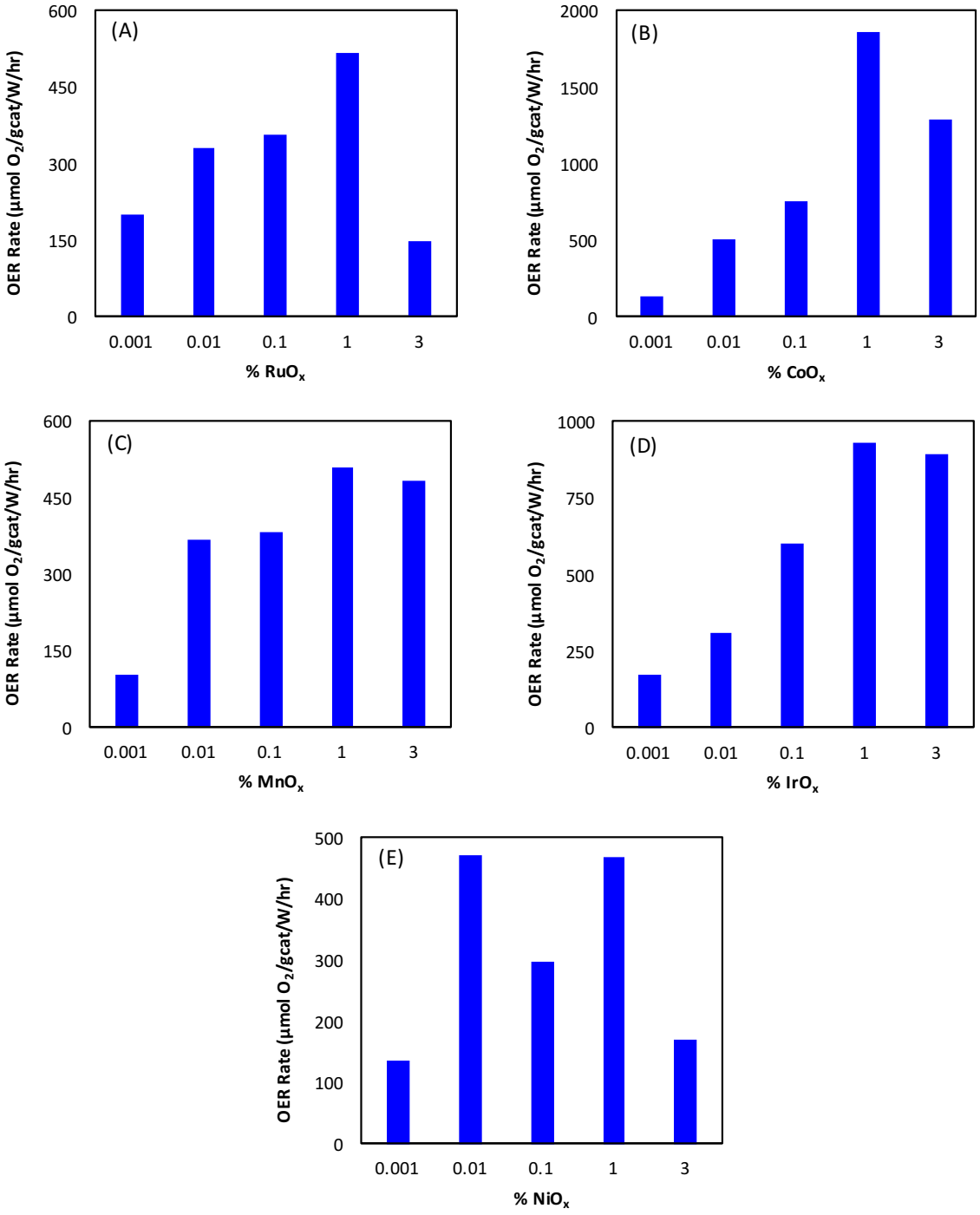

Figure 5.10 OER rates for varying CC weight loadings on ZnO SC with CCs: (A) RuO_x, (B) CoO_x, (C) MnO_x, (D) IrO_x and, (E) NiO_x. These samples were illuminated with 365nm light causing the rate per watt of illumination ~3-fold larger than the OER rates in Fig 5.9.

The relative reactivity of RuO_x varied across the three SCs, between 18% and 66% of the maximum OER rate measured on each respective SC. IrO_x was the top CC in two of the three systems, however exhibited 56% of the CoO_x rate when deposited on ZnO. Similarly, CoO_x was the top CC in two of the three systems, but displayed only 49% of the IrO_x rate when deposited on $BiVO_4$. NiO_x as a CC varied from 3% to 66% of the maximum OER rate across the explored SCs. MnO_x was generally the least active CC, exhibiting OER activities between 2% and 37% of the maximum performing OER CC. The worst performing CC was different on each SC, where RuO_x was the lowest for SnO_2, MnO_x was the worst on $BiVO_4$, and NiO_x was the worst for ZnO. In summary, we observed differences in relative CC reactivity comparing the different SC systems and expectations of OER reactivity from previous electrocatalytic OER measurements.

5.5 Discussion

5.5.1 SC-Dependent Reactivity.

The first trend we will address is the generally observed trend in the OER rate across the three SCs, as the maximum rates for ZnO, $BiVO_4$, and SnO_2 were 612, 200, and 102 μmol/gcat/W, respectively. The large difference in OER rates across the different SCs could be a result of several factors such as: light absorption efficiency of the SC (absorption cross section and overlap between the band gap and illumination source), SC supplied OER overpotential (defined here by the difference in energy between the SC VBM and the OER redox potential, see Figure 5.1(a)), rate of e^-/h^+ pair recombination in the SC, SC surface defects, and surface area (controls the required charge carrier migration distance).

Reactivity experiments were all performed with a broad-band light source illuminating SCs with different band gap energies, so it would be expected that the differences in light absorption and excitation efficiency could play a large role in controlling OER reactivity. However, the order of OER reactivity was not solely controlled by the magnitude of the overlap between the broad-band light source and the SC light absorption as $BiVO_4$ had the lowest band gap yet did not have the highest OER rate. With these SCs and many oxide semiconductors in general, band gap is intrinsically linked to SC supplied OER overpotential. The SC supplied OER overpotential is a measure of how much oxidative potential h^+s contain when initially formed in the SC. Given the small expected band bending in our systems due to similarity between the EL E_f and that of the SCs, the SC supplied OER overpotential is likely similar to the overpotential retained in the h^+ when it reaches the SC|CC|EL junctions. The intrinsic link between the band gap and SC supplied OER overpotential is a result of oxides having fairly fixed CBM positions and variable VBM positions, so most variation in band gaps between SC metal oxides is a result of variation in the VBM and therefore SC supplied OER overpotential. Thus, as band gap increased from $BiVO_4$ to SnO_2, SC supplied OER overpotential increased in the same direction. This may help explain the order of the OER reactivity between the different SCs, as ZnO had the best balance between light absorption and SC supplied OER overpotential, whereas $BiVO_4$ may have been limited by the lower SC supplied OER overpotential and SnO_2 may been limited by low light absorbance. SC surface area may be another factor affecting OER rates, which can translate to differences in distance a h^+ has to travel to reach the CC and drive OER without recombination with an e^-. ZnO had a much larger surface

area than SnO_2 and $BiVO_4$. Thus, for the SC structures explored here, ZnO may exhibit the best balance of high surface area, large SC supplied OER overpotential and reasonable overlap with the light source emission spectra, allowing for optimal performance.

Other factors which may have some role in the reactivity order between the different SCs are the defect density in the bulk and at the surface of the SCs. The bulk defect density could dictate what fraction of absorbed photons actually make it to the SC|EC interface in the form of h^+s to drive the OER compared to the fraction that end up recombining with e^-s at bulk defect recombination sites or trap sites. Surface defects can also hinder charge transfer, acting as a recombination site. CC dispersion for each SC was also considered as a potential cause for the large difference in reactivity between the SC systems, but was disregarded after comparing OER rates with STEM micrographs. The large disparity in normalized OER rate for IrO_x when supported on $BiVO_4$, SnO_2, and ZnO did not agree with what appeared to be similar dispersions of IrO_x on all 3 SCs, Figure 5.7. Additionally, the order of CoOx dispersion was ZnO>>$BiVO_4$>SnO_2, Figure 5.8, which disagreed with the order of normalized OER reactivity of ZnO~SnO_2>$BiVO_4$, Figure 5.11(a). The OER differences in reactivity across the SCs show that one cannot simply pick a SC with the smallest band gap energy with VBM and CBM positioned such that redox reactions would be feasible. Previous work supports that many factors relating to SC surface area/particle size, band gap, band positions all affect reactivity.[40] There are several factors which may impact overall reactivity of each SC system, however the point of this work was to better understand the differences in reactivity between various SC|CC junctions. Thus, the absolute order of reactivity comparing the SCs does not influence comparison of the CC

reactivity across the SCs if we focus on variations in the relative trend in CC OER reactivity across each SC.

5.5.2 CC-Dependent Reactivity.

As shown in Figure 5.11(a), the relative order of reactivity across the CCs was different on each SC, consequently, it can be seen that measurements of CC reactivity in electrochemical environments cannot be used to directly predict performance in PPC systems. It could be imagined that the inherent reactivity of each CC could be modified through interactions with the SC, much in the same way support effects in traditional catalysis occur, although this influence should be small and relatively consistent across all CCs for each SC. As has also been shown previously,[22,25,41] the surface electronic structure of these PPC materials will not be largely influenced by the electronic structure of the CCs due to operation in the pinch-off CC particle size and loading regime. Without the electronic structure or E_f of the CC affecting charge transfer across the SC|CC junction, it would be expected that for a given SC, the OER reactivity would be controlled by the inherent reactivity of the CC measured in electrochemical environments. Our results show that something other than band bending at the SC|CC junction, or inherent CC reactivity, controls the varying relative reactivity of the CCs across each SC.

Oxideloxide junctions, similar to those found in our SC|CC systems are known to be complicated in terms of geometric and electronic structure.[42] In the semiconductor and photovoltaics industries, significant effort is given to the development of synthetic approaches for creating coherent solid junctions, essentially allowing epitaxial growth with no defects or trap states. However, the formation of a coherent interface is dependent on

lattice matching both in size and structure between the oxide components.[42,43] Similarly, in the field of heterogeneous catalysis it is known that the geometry (shape, size and exposed surface facet) of catalytic structures grown on oxide supports (similar to the SCs studied here) can depend on the strength and nature of the interaction between the support and catalyst.[44,45] Based on these analyses it would be expected that atomic scale interactions

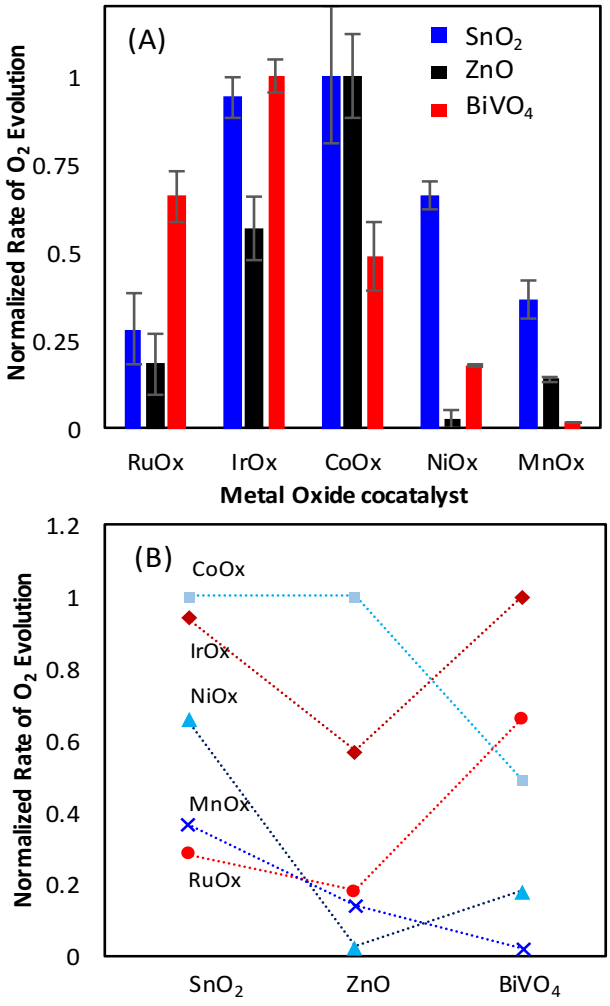

Figure 5.11 (A) Normalized OER rates to the highest OER rate for each SC. (B) Normalized OER rate for each CC series as a function of SC. Normalization was performed identically as to (A).

between the CC and SC at the SC|CC junction could significantly modify charge transport and potentially the inherent CC reactivity by influencing the exposed crystal facet.

This study was performed with varying SC and CC crystal structures to investigate the role of interfacial geometry on OER rate, where interfacial defects or lattice mismatch could introduce localized charge carrier trap sites that serve as efficient recombination sites. [42,46] In addition, CCs of both metallic and semiconductor conductivity were included to test the influence of CC conductivity on SC|CC junction performance. To investigate both geometric and CC conductivity effects, normalized OER rates were plotted for each CC series with respect to the SC, Figure 5.11(b). $BiVO_4$ is the SC on which the CCs behave most differently from one another, which is also the SC with the largest unit cell as shown in Table 5.3. Two of the rutile structured CCs (RuO_x and IrO_x) trend with increased normalized OER rates, when on $BiVO_4$, compared to the other CCs. The rutile CCs initially appear to form a better contact with the larger unit cell SC in $BiVO_4$ and the two non-rutile CCs (CoO_x and NiO_X) appear form better contacts with the smaller unit cell SCs. However, MnO_x is also rutile structured and did not show an increase in OER reactivity when bound to $BiVO_4$. In addition, if geometry played the predominant role in these varying CC reactivity trends through controlling charge transfer, then the rutile CCs should also exhibit increases in normalized OER rates when bound to the rutile structured SnO_2, due to the

Table 5.3. SC Crystal structures and lattice parameters determined from XRD

	$BiVO_4$	ZnO	SnO_2
Crystal Structure	Monoclinic	Wurtzite (hexagonal)	Rutile (Tetragonal)
Lattice Constant A	5.19	3.25	4.72
Lattice Constant B	5.09	-	-
Lattice Constant C	11.70	5.20	3.19

more coherent junctions associated with the same crystal structures. Therefore, while we don't intend to rule out SC|CC junction geometry as a factor that can influence the system reactivity in other systems, the trends in OER rates in this study did not seem to be dictated by geometry-controlled charge transfer.

Table 5.4. CC crystal structures and lattice parameters of SC and CC determined from previous studies.

	RuO_2	IrO_2	MnO_2	Co_3O_4	NiO
Crystal Structure[47]	Rutile	Rutile	Rutile	Spinel	Rock Salt
Lattice Constant A[48,49]	4.50	4.51	4.40	8.08	4.18
Lattice Constant C[48,49]	3.10	3.16	2.87	-	-
Conduction Type[47]	Metallic	Metallic	Semi	Semi	Semi

With the lack of relationship between system performance and SC band bending, electrochemically measured CC reactivity, or geometry constrained charge transfer across the SC|CC junction, CC conductivity was thought to potentially influence OER reactivity. CoO_x, NiO_x, and MnO_x all exhibit non-metallic electronic behavior and IrO_x and RuO_x both typically exhibit more metallic conductivity, Table 5.4.[47] In Figure 5.11(b), the three non-metallic CCs generally exhibited higher relative OER reactivity when deposited on SnO_2 and ZnO than on $BiVO_4$. This can be explained by the higher SC supplied OER overpotential with SnO_2 and ZnO, which provides additional driving force for h^+ transfer through the low conductivity of the non-metallic CCs to the OER active sites. This observation agrees well with the generally higher normalized OER rates for IrO_x and RuO_x (metallic CCs) on $BiVO_4$, because $BiVO_4$ has the smallest SC supplied OER overpotential and would therefore favor CCs with higher electronic conductivities that enable facile h^+ to OER active sites. Thus it seems that for SCs with large SC supplied OER overpotentials,

non-metallic CCs retain their reactivity, whereas for SCs with smaller SC supplied OER overpotential, conductive CCs are required to enable high OER rates.

Although CC conductivity and SC supplied OER overpotential appear to significantly dictate OER rate, we cannot completely neglect other specific SC|CC interactions which may control the CC shape and expose facets with varied OER rates, as prior work has demonstrated OER rates vary by CC facet.[27,28] The HAADF STEM micrographs show IrO_x formed in a much more dispersed geometry than CoO_x on all of the SCs, suggesting that SC-specific CC shape formation must be considered when assembling an optimal photocatalyst, Figure 5.7,5.8. In addition, geometric alignment at the SC|CC junction may not have been a crucial factor affecting OER rates in this study, however it should still be considered when designing an optimal PPC or PEC, as the findings in a single study can't represent the significant complexity associated with complex oxideloxide junctions.

5.6 Conclusions

In conclusion, we showed that benchmarked comparisons of oxide catalyst performance in electrochemical OER cannot be used to predict the performance of these catalysts in PPC systems. It is argued that various attributes of SC|CC junctions, including most prominently SC supplied overpotential and CC conductivity significantly control the reactivity of SC|CC systems for OER. Essentially one cannot simply combine an optimal CC and SC and expect optimal PPC performance without considering atomistic details of SC|CC junction formation on performance.

5.7 References

1. K. Domen, S. Naito, M. Soma, T. Onishi and K. Tamaru, *J. Chem. Soc. Chem. Comm.*, 1980, 543–544.

2. S. Sato and J. M. White, *Ind. Eng. Chem. Prod. Res. Dev.*, 1980, **19**, 542–544.

3. Fujishima and K. Honda, *Nature*, 1972, **238**, 37–38.

4. P. J. Boddy, *J. Electrochem. Soc.*, 1968, **115**, 199–203.

5. B. A. Pinaud, J. D. Benck, L. C. Seitz, A. J. Forman, Z. Chen, T. G. Deutsch, B. D. James, K. N. Baum, G. N. Baum, S. Ardo, H. Wang, E. Miller and T. F. Jaramillo, *Energy Environ. Sci.*, 2013, **6**, 1983–2002.

6. D. M. Fabian, S. Hu, N. Singh, F. A. Houle, T. Hisatomi, K. Domen, F. E. Osterloh and S. Ardo, *Energy Environ. Sci.*, 2015, **8**, 2825–2850.

7. K. Lee, B. M. Tienes, M. B. Wilker, K. J. Schnitzenbaumer and G. Dukovic, *Nano Lett.*, 2012, **12**, 3268–3272.

8. J. Choi, H. Park and M. R. Hoffmann, *J. Mater. Res.*, 2010, **25**, 149–158.

9. X. Yong and M. A. A. Schoonen, *Am. Mineral.*, 2000, **85**, 543–556.

10. H. Park, H. Kim, G. Moon and W. Choi, *Energy Environ. Sci.*, 2016, **9**, 411–433.

11. M. R. Singh, K. Papadantonakis, C. Xiang and N. S. Lewis, *Energy Environ. Sci.*, 2015, **8**, 2760–2767.

12. D. G. Nocera, *Acc. Chem. Res.*, 2012, **45**, 767–776.

13. T. W. Kim and K.-S. Choi, *Science*, 2014, **343**, 990–994.

14. G. Hodes, D. Cahen and J. Manassen, *Nature*, 1976, **260**, 312–313.

15. B. Bocarsly, D. C. Bookbinder, R. N. Dominey, N. S. Lewis and M. S. Wrighton, *J. Am. Chem. Soc.*, 1980, **102**, 3683–3688.

16. K. Maeda, T. Takata, M. Hara, N. Saito, Y. Inoue, H. Kobayashi and K. Domen, *J. Am. Chem. Soc.*, 2005, **127**, 8286–8287.

17. C. Man, H.-Y. Su, F. Calle-Vallejo, H. A. Hansen, J. I. Martínez, N. G. Inoglu, J. Kitchin, T. F. Jaramillo, J. K. Nørskov and J. Rossmeisl, *ChemCatChem*, 2011, **3**, 1159–1165.

17a. J. K. Nørskov, J. Rossmeisl, A. Logadottir, L. Lindqvist, J. R. Kitchin, T. Bligaard and H. Jónsson, J. Phys. Chem. B, 2004, 108, 17886–17892.

18. T. F. Jaramillo, K. P. Jørgensen, J. Bonde, J. H. Nielsen, S. Horch and I. Chorkendorff, *Science.*, 2007, **317**, 100–102.

19. L. Trotochaud, S. L. Young, J. K. Ranney and S. W. Boettcher, 2014, **136**, 6744–6753.

20. F. Lin, B. F. Bachman and S. W. Boettcher, *J. Phys. Chem. Lett.*, 2015, **6**, 2427–2433.

21. M. T. Uddin, Y. Nicolas, C. Olivier, T. Toupance, M. M. Müller, H.-J. Kleebe, K. Rachut, J. Ziegler, A. Klein and W. Jaegermann, *J. Phys. Chem. C*, 2013, **117**, 22098–22110.

22. Y. Ping, W. A. I. Goddard and G. A. Galli, *J. Am. Chem. Soc.*, 2015, **137**, 5264–5267.

23. Z. Zhang and J. T. Yates Jr., *Chem. Rev.*, 2012, **112**, 5520–5551.

24. R. C. Rossi and N. S. Lewis, *J. Phys. Chem. B*, 2001, **105**, 12303–12318.

25. F. Lin and S. W. Boettcher, *Nat. Mater.*, 2014, **13**, 81–86.

26. M. Szklarczyk and J. O. Bockris, *J. Phys. Chem.*, 1984, **88**, 1808–1815.

27. K. A. Stoerzinger, L. Qiao, M. D. Biegalski and Y. Shao-Horn, *J. Phys. Chem. Lett.*, 2014, **5**, 1636–1641.

28. Z. Chen, C. X. Kronawitter and B. E. Koel, *Phys. Chem. Chem. Phys.*, 2015, **17**, 29387–29393.

29. W. Sun, M. Xie, L. Jing, Y. Luan and H. Fu, *J. Solid State Chem.*, 2011, **184**, 3050–3054.

30. M. Moser, C. Mondelli, A. P. Amrute, A. Tazawa, D. Teschner, M. E. Schuster, A. Klein-Hoffman, N. López, T. Schmidt and J. Pérez-Ramírez, *ACS Catal.*, 2013, **3**, 2813–2822.

31. J. Liu, C. Li, F. Wang, H. Shan, H. Chen, Y. Zhao, M. Wei, D. G. Evans and X. Duan, *Catal. Sci. Technol.*, 2013, **3**, 2627–2633.

32. M. Del Arco and V. Rives, 1986, **21**, 2938–2940.

33. P. G. Smirniotis, P. M. Sreekanth, D. A. Peña and R. G. Jenkins, *Ind. Eng. Chem. Res.*, 2006, **45**, 6436–6443.

34. S. Linic, P. Christopher and D. B. Ingram, *Nat. Mater.*, 2011, **10**, 911–921.

35. P. Christopher, D. B. Ingram and S. Linic, *J. Phys. Chem. C*, 2010, **114**, 9173–9177.

36. C. C. L. McCrory, S. Jung, I. M. Ferrer, S. M. Chatman, J. C. Peters and T. F. Jaramillo, *J. Am. Chem. Soc.*, 2015, **137**, 4347–4357.

37. S. Chen and L.-W. Wang, *Chem. Mater.*, 2012, **24**, 3659–3666.

38. M. T. Uddin, Y. Nicolas, C. Olivier, T. Toupance, L. Servant, M. M. Müller, H.-J. Kleebe, J. Ziegler and W. Jaegermann, *Inorg. Chem.*, 2012, **51**, 7764–7773.

39. C. C. L. McCrory, S. Jung, J. C. Peters and T. F. Jaramillo, *J. Am. Chem. Soc.*, 2013, **135**, 16977–16987.

40. Kudo and Y. Miseki, *Chem. Soc. Rev.*, 2009, **38**, 253–278.

41. M. G. Walter, E. L. Warren, J. R. McKone, S. W. Boettcher, Q. Mi, E. A. Santori and N. S. Lewis, *Chem. Rev.*, 2010, **110**, 6446–6473.

42. M. O'Sullivan, J. Hadermann, M. S. Dyer, S. Turner, J. Alaria, T. D. Manning, A. M. Abakumov, J. B. Claridge and M. J. Rosseinsky, *Nat. Chem.*, 2016, DOI: 10.1038/NCHEM.2441.

43. E. Bauer and J. H. van der Merwe, *Phys. Rev. B*, 1986, **33**, 3657–3671.

44. Y. Stakheev and L. Kustov, *Appl. Catal. A Gen.*, 1999, **188**, 3–35.

45. J. A. Farmer and C. T. Campbell, *Science*, 2010, **329**, 933–936.

46. W. A. Smith, I. D. Sharp, N. C. Strandwitz and J. Bisquert, *Energy Environ. Sci.*, 2015, **8**, 2851–2862.

47. Y. Matsumoto and E. Sato, *Materials Chemistry and Physics*, 1986, **14**, pp. 397–426.

48. A. Bolzan, C. Fong, B. J. Kennedy and C. J. Howard, *Acta Crystallogr. Sect. B*, 1997, **B53**, 373–380.

49. N. R. Rao and G.V. Subba Rao, Transition Metal Oxides: Crystal Chemistry, Phase Transition, and Related Aspects; U.S. Govt. Print. Off: Washington.,1974.

Chapter 6 Conclusions and Future Work

6.1 Summary

The bulk of this dissertation was prepared from combining a variety of characterization techniques, both *in-situ* and *ex-situ,* with creative experimental testing to design optimal heterogeneous catalysts and photocatalysts. We showed that Rh_{iso} sites play a different role in driving CO_2 reduction than Rh_{NP} sites and can be exploited for significant CO_2 reduction selectivity. Additionally, it was shown that A-SMSI overlayers can be produced to reversibly control CO_2 reduction selectivity by up to ~90%. We also demonstrate the importance of matching SC and CC for optimal photocatalyzed OER, and that one cannot simply deposit a CC with the lowest overpotential on a SC with the highest light absorption. In this chapter, we review the main conclusions of this work and future work which may stem from these conclusions.

6.2 Conclusions

The main goals of this work were to investigate catalyst geometry and catalyst/co-catalyst interactions with supports or SCs and how these factors affect each other and how they affect catalytic performance. In particular, we examined: the role isolated Rh sites may play in the structure sensitivity of Rh catalyzed CO_2 reduction, the role of A-SMSI behavior causing a dynamic change in CH_4 selectivity observed with time-on-stream and how this could be exploited for selectivity control, and the potential implications of expanding universalities derived for electrocatalytic water splitting to photocatalytic water splitting, particularly the OER. The following are the main dissertation conclusions:

In Chapter 3, we determined site specific reactivity assignments, where in CO_2-H_2 environments Rh_{iso} sites drive CO production and Rh_{NP} sites drive CH_4 production. In the

isolated catalyst site or single atom catalyst field, site specific reactivity measurements have been very limited due to the lack of a quantitative method for counting isolated sites. Therefore, we developed a quantitative DRIFTS method for measuring the fraction of Rh_{iso} and Rh_{NP} sites by combining a spectrum of Rh weight loadings, CO probe molecule DRIFTS measurements, and previously determined extinction coefficients.[1] These site fractions were then compared to reactivity data to determine the site-specific reactivity assignments. These assignments were further supported with selective removal of Rh_{NP} sites via leaching and consequential suppression of CH_4 activity. Additionally, an atypical dynamic change in reactivity was observed with time-on-stream, where the activity of CH_4 production decreased and CO production increased. Insights gained in this work provide important information for the design of highly reactive and selective CO_2 reduction catalysts and stress the importance of considering how the catalyst structures may change under reaction conditions. Furthermore, this work emphasizes the importance of considering catalytic sites that may go undetected with traditional TEM approaches when developing rigorous structure function relationships in catalysis.

The peculiar catalytic behavior observed for Rh/TiO_2 catalysts at high CO_2:H_2 ratios in chapter 4 was investigated with a battery of synthesis, characterization, and catalytic reactivity analysis techniques to understand the underlying state of the catalyst and its potential utility in controlling selectivity. We demonstrated that HCO_x adsorbates on TiO_2 and Nb_2O_5 supported Rh catalysts can induce oxygen vacancy formation in the support and drive the formation of an A-SMSI overlayer on Rh. The A-SMSI overlayer is porous, allowing reactants to still interact with the Rh surface, and stable under humid reaction

conditions. The existence of the A-SMSI overlayer locally modifies the reactivity of the underlying Rh nanoparticles surface, opening new avenues for tuning and controlling the reactivity of supported metal catalysts.

In chapter 5, we showed that benchmarked comparisons of oxide catalyst performance in electrochemical OER cannot be used to predict the performance of these catalysts in PPC systems. This was demonstrated by synthesizing a library of 15 catalysts (3 SCs and 5 CC) with varying electronic and physical structures. Here we suggest that various attributes of SC|CC junctions, including most prominently SC supplied overpotential and CC conductivity significantly control the reactivity of SC|CC systems for OER. Essentially one cannot simply combine an optimal CC and SC and expect optimal PPC performance without considering atomistic details of SC|CC junction formation on performance.

The work discussed here essentially sheds light on frequently overlooked effects in both metal catalyzed CO_2 reduction reactions and the pairing of metal oxide CCs with SCs for photocatalytically driving water splitting. Although the majority of our work was focused on Rh/TiO_2 catalyzed CO_2 reduction to CH_4 and CO and photocatalyzed water splitting for driving the OER, the understanding gained should still translate to other systems and reactions. By using CO_2 reduction as a model reaction with two main pathways in this work, we have demonstrated that Rh_{iso} and Rh_{NP} sites differ in reactivity as they each drive different reaction pathways. This differing reactivity should help control selectivity in many different reactions with pathways that are at least differentiated by the degree of reduction required as the CO and CH_4 pathways contain. The same can be said regarding

the A-SMSI encapsulation we investigated in chapter 4, as we showed that this encapsulation causes the Rh_{NP} sites to behave like a more noble metal and therefore preferentially drive a gentler reduction. Therefore, in both chapters 3 and 4, we have established that both isolated sites and adsorbate induced/mediated encapsulation of NP's affect reactivity, allowing for selectivity control in reactions with multiple pathways. The work in chapter 5 provides insight regarding the placement of CCs on SCs, stresses the numerous variables to consider, and highlights the importance of SC-supplied overpotential and the electronic conductivity of CCs for for designing optimal photocatalysts.

6.3 Future Work

There are many different directions to take the work performed in this dissertation. The Rh_{iso} and Rh_{NP} site assignment work in chapter 3 has already been followed up with a computational study elucidating why these sites drive different CO_2 reduction pathways,[2] and there are several other potential studies that can stem from the insights gained regarding our work both reaction-wise and material wise. Moving forward, the CO probe molecule technique developed in this work will be essential for quantifying isolated catalyst sites to probe the potential role isolated sites may have on other reactions. One specific study would be to explore other metal types and reaction conditions to test the effect of isolated sites for driving other reactions which may have more industrial relevance. These studies could be performed fairly analogously to the study in chapter 3, however working with other metals can be difficult to quantify isolated sites as CO does

not often bind in a germinal dicarbonyl geometry on isolated sites for other metals, and would require a fair amount of work to distinguish between isolated and NP sites.

In chapter 4, it was shown that Rh could be encapsulated with an adsorbate stabilized overlayer of reduced TiO_x formed as a function of temperature or time on stream and these variables could be used to control CH_4 selectivity. Nb_2O_5 supported Rh also exhibited similar catalytic behavior, however may form a more stable overlayer. Future work could include a more thorough evaluation of the phenomena causing the catalytic change in reactivity associated with Nb_2O_5 upon $20CO_2$:$2H_2$ treatment. Additionally, due to Nb_2O_5 forming a more resistant traditional SMSI overlayer to CO_2 reduction conditions than TiO_2,[3] another potential study that we have initiated is to potentially control selectivity simply with reduction temperature. The idea here being kind of a combination of the isolated Rh sites work in chapter 3, where CO is produced by Rh_{iso} sites and CH_4 is produced by Rh_{NP} sites, and the work in chapter 4, where only the Rh_{NP} sites were selectively encapsulated with the Rh_{iso} sites still left exposed for CO production. Here, the idea would be to maximize CO selectivity by identifying a specific reduction temperature which would selectively encapsulate the Rh_{NP} sites while leaving the Rh_{iso} sites exposed for CO production.

6.4 References

1 T. M. Duncan, J. T. Yates Jr. and R. W. Vaughan, *J. Chem. Phys.*, 1980, **73**, 975.

2 S. Ma, W. Song, B. Liu, H. Zheng, J. Deng, W. Zhong, J. Liu, X.-Q. Gong and Z. Zhao, *Catal. Sci. Technol.*, 2016, DOI: 10.1039/C5CY02158H

3 C. Deleitenburg and A. Trovarelli, *J. Catal.*, 1995, **156**, 171–174.

4 T. Abe, M. Tanizawa, K. Watanabe and A. Taguchi, *Energy Environ. Sci.*, 2009, **2**, 315.